ABSTRACT

WANG, GUIZHOU. Hygrothermal Performance of Southern Pine Cross-Laminated Timber. (Under the direction of Dr. Perry Peralta and Dr. Phil Mitchell).

Being a relatively new wood product, cross-laminated timber (CLT) has advantages such as dimensional stability, high strength and stiffness properties, good acoustic and fire resistance, fast on-site processing, and great potential as substitute for concrete and steel in building envelopes. However, the properties of CLT are highly species dependent. This research chose southern pine as subject species because of its economic importance as the most widely-planted tree species group in the US, and perhaps, the world.

In this research, the effect of three commonly available adhesives (polyurethane, phenol resorcinol formaldehyde, and melamine formaldehyde) on moisture transport, warping, and fire performance on southern pine CLT were analyzed.

Results showed that moisture transport below fiber saturation point in southern pine CLT can be modeled as a diffusion process. Glueline moisture diffusion coefficient was independent of adhesive type, and a well-constructed CLT wall assembly did not provide favorable conditions for mold growth. Warping results validated the hygrothermal warping model, revealed that cross lamination improved the dimensional stability of CLT as compared to solid wood, and showed that adhesive type had no or little effect on the degree of warping. Findings from fire tests and thermal analyses demonstrated that polyurethane performed poorly under high temperature or fire conditions, while phenol resorcinol formaldehyde was very thermally stable. Adhesive type had a significant effect on the charring rate of the second layer of CLT. The effect of edge gluing on fire performance of CLT remains uncertain and further research with more replication is needed.

Hygrothermal Performance of Southern Pine Cross-laminated Timber

by
Guizhou Wang

A dissertation submitted to the Graduate Faculty of
North Carolina State University
in partial fulfillment of the
requirements for the degree of
Doctor of Philosophy

Forest Biomaterials

Raleigh, North Carolina
2018

APPROVED BY:

_____	_____
Dr. Perry Peralta Committee Co-chair	Dr. Phil Mitchell Committee Co-chair
_____	_____
Dr. Ilona Peszlen	Dr. Joel Pawlak

_____
Dr. Michael Stoskopf

DEDICATION

This dissertation work is dedicated to my dear mom, Jinying Wei; dad, Bangyu Wang; and two sisters, who have been my constant source of support and encouragement during the challenges of overseas study and life. I'm truly grateful to have you all in my life.

BIOGRAPHY

Guizhou Wang was born on 06 January 1991 in Hefei, Anhui, China. He earned his Bachelor of Science degree in Light Chemical Engineering in 2011 from South China University of Technology in Guangzhou, Guangdong, China. Then he moved to Miami University, Oxford, Ohio, USA for MS study in 2012 and earned his Master of Science in Chemical Engineering in 2015. He began work on his Doctor of Philosophy in 2014 at North Carolina State University, Raleigh, North Carolina, USA. His fields of interest include pulp and paper making, paper physics, wood composite and wood mechanics.

ACKNOWLEDGMENTS

Special thanks to USDA-NIFA Integrated Forest Products Research Grant Program for the fund provided under Grant # 2012-03699.

I would like to express my deepest gratitude to my advisor Dr. Perry Peralta, who guided me in my my work, and gave me both academic and financial supports!

I also want to thank Dr. Ilona Peszlen for her concern and care, especially during the times when I had health issues. The supports from Dr. Peralta and Dr. Peszlen meant a lot to me and made me feel at home!

And it is my great honor to have Dr. Phil Mitchell as my co-chair, and Dr. Joel Pawlak and Dr. Michael Stoskopf as my committee members! Thank you all so much for your thoughtful suggestions and precious time!

Meanwhile, I am also grateful to Zach Miller, Mike Maltby, Guillermo Velarde and my best friends Yuhan Wang and Wenhui Geng for all the support they gave me during my work here.

Lastly, I want to thank my family for raising me and supporting me all these years!

Thank you all, my advisor, committee members, friends and my family! Without your support, it would be impossible for me to go through the hard times and accomplish my PhD work. I will remember all these forever!

TABLE OF CONTENTS

LIST OF TABLES

LIST OF FIGURES

CHAPTER 1. INTRODUCTION

1. Background

Cross-Laminated Timber (CLT), also known as X-lam (cross lam) or massive timber, was first developed in Europe in the early 1990s. Further research work in Austria in the mid-1990s led to CLT as we know it today. Due to advantages such as long span; dimensional stability compared to other wood products; superior fire, seismic, acoustic and thermal performance; excellent strength and stiffness properties; fast on-site processing due to prefabrication; and light weight as compared to concrete, CLT is expected to have the potential to replace concrete, steel, and masonry in low- and mid-rise residential and commercial constructions.

According to the American National Standard ANSI/APA PRG 320 (American National Standard Institute, 2012), cross-laminated timber is:

A prefabricated solid engineered wood panel made of at least three orthogonally bonded layers of solid-sawn lumber or structural composite lumber (SCL) that are laminated by gluing of longitudinal and transverse layers with structural adhesives to form a solid rectangular-shaped, straight and plain timber intended for roof, floor, or wall application.

Or in a more straightforward language, CLT panels consist of several layers of lumber stacked crosswise typically at 90 degrees and glued together on their wide faces, sometimes on the narrow sides as well, as shown in Figure 1.1.

Figure 1.1. Picture of a cross-laminated timber (Courtesy of APA-The Engineered Wood Association).

Being a relatively new material, though CLT has gained more and more research interests, there are still a lot left to be studied due to the fact that the properties of CLT are species related. For instance, no data existed for the moisture diffusion in southern pine CLT, even though southern pine is one of the most planted tree species group in the US, and has good strength properties and competitive price.

As mentioned previously, CLT is made of solid sawn or structural composite lumber. Given the fact that wood is a hygroscopic material, the lack of database (such as southern pine CLT diffusion) can raise concerns of water accumulation in CLT in use. This can further result in issues like mold growth and its associated health concerns. Meanwhile, like wood and wood products, CLT will shrink or swell when it loses or accumulates water. This can substantially affect the dimensional stability and therefore can raise safety concerns, especially when it is used as a loading bearing element. Lastly, being a combustible material, fire performance of CLT needs to be studied to address fire safety concerns.

2. Objective

The overall purpose of this study was to increase the acceptance of CLT, or more specifically southern pine CLT, by addressing concerns stated previously. The specific goals are:

1. Model the diffusion process in southern pine CLT to analyze the effect of adhesive types on diffusion and study the hygrothermal performance of CLT building envelopes.
2. Model the warping of southern pine CLT, and thereby predict and analyze the dimensional stability of southern pine CLT.
3. Improve the fire performance of southern pine CLT by means of different adhesives and edge gluing.

3. Outlines of the dissertation

To accomplish the objectives in Section 1.2, a general introduction of cross-laminated timber was given first in Chapter 1. The modeling of southern pine CLT and hygrothermal performance of CLT building envelopes were discussed in Chapter 2. The diffusion data in Chapter 2 were used as data input for the hygrothermal warping model study in Chapter 3, with the aim to address the dimensional stability concern of CLT. With regard to the fire safety of southern pine CLT, thermal studies of adhesives, small-scale fire tests, and intermediate-scale horizontal fire tests were performed and discussed in Chapter 4. Lastly, an overall summary of this study was given in Chapter 5.

CHAPTER 2. MOISTURE TRANSPORT IN CROSS-LAMINATED TIMBER

Moisture transport in southern pine cross-laminated timber (CLT) and moisture accumulation in a building envelope with cross-laminated timber as wall component was addressed in this chapter. A general literature review of wood, moisture transport in wood, and wood adhesives will be provided first. Then diffusion studies of solid southern pine and southern pine CLT will be discussed where the diffusion process in southern pine CLT is modeled and the effect of adhesive types on diffusion is analyzed. A study on the hygrothermal performance of CLT building envelopes will be described thereafter to further address concerns of moisture accumulation and mold growth in CLT.

1. Literature Review

1.1. General Introduction of Wood

Wood, as one of the most important and abundant renewable raw materials, has been utilized by human beings since the start of history. Now, with the increasing awareness of environmental issues and the growing demand for a “green” world, wood utilization has become more and more important in many areas, one of which is the construction industry.

Visible on the cross section of a mature tree (Figure 2.1) are several macroscopic features: bark, vascular cambium, sapwood, heartwood, and pith (from outside to inside). The wood produced early in the growing season, called earlywood, has large cell lumens and thin cell walls. The wood produced later in the growing season, called latewood, has smaller cell lumens and thicker cell walls.

In softwoods such as southern pine, the longitudinally aligned tracheids cover 90-95% of the volume and have the main function of fluid transport and mechanical support. In addition to

tracheids, parenchyma cells could appear in both longitudinal and radial directions with the main function of nutrient storage (Kettunen, 2006). When formed in the radial direction, they compose the basic structure of rays. Rays are assumed to reinforce wood in the radial direction (Burgert & Eckstein, 2001).

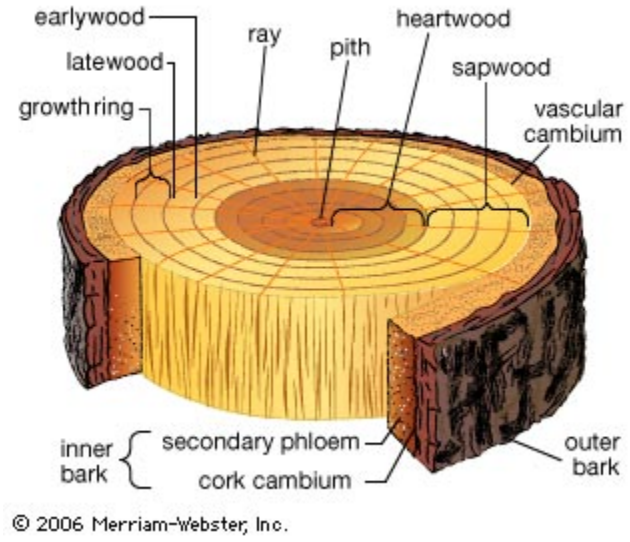

Figure 2.1. Tree cross section from bark (outside) to pith (center).

1.2. Moisture in Wood

1.2.1. Moisture Content of Wood

In the wood industry, **moisture content** is expressed as the percentage of the mass of water relative to the mass of oven-dry wood, as given by the following equation (Siau, 1984):

$$\boldsymbol{Moisture\ Content} = \boldsymbol{w} = \frac{\boldsymbol{m_g - m_{od}}}{\boldsymbol{m_{od}}} \times \mathbf{100}\% \qquad (1)$$

where *w* is the moisture content; m_g is the total mass of the wood; m_{od} is the oven-dry mass of the wood. The mass of oven-dry wood is the mass when wood placed in a forced convection oven heated at 103±2 ℃ shows no appreciable mass change.

Moisture content of wood varies with wood species, sapwood/heartwood ratio, surrounding air, drying history and many other factors. The moisture content for some living trees could be more than 100%, while that of solid wood products in use is around 10%. Moisture content is a critical parameter for all wood products since it can affect its strength properties, density, specific gravity, moisture and thermal diffusion processes, dimensions and other properties.

When wood is neither gaining nor losing moisture to the environment, or in other words, the water in the wood is in balance with the water in the environment, it reaches the equilibrium state and the moisture content at this condition is called the **equilibrium moisture content (EMC)**. This equilibrium is not a static but a dynamic process: the water in wood continues to exchange with water in the environment, however at equilibrium the net gain or loss is zero.

EMC is closely related to temperature and relative humidity, where **relative humidity** (RH) is defined as:

$$\boldsymbol{RH = \frac{p}{p_0} \times 100} \qquad (2)$$

where p is the partial vapor pressure in air and p_0 is the saturated vapor pressure at a given temperature of air.

The **Hailwood-Horrobin** equation is usually used to approximate EMC (Hailwood & Horrobin, 1946a):

$$\boldsymbol{EMC = \frac{1800}{W}\left[\frac{kh}{1-kh} + \frac{k_1 kh + 2k_1 k_2 k^2 h^2}{1 + k_1 kh + k_1 k_2 k^2 h^2}\right]} \quad (3)$$

where:

$W = 330 + 0.452T + 0.00415T^2$

$k = 0.791 + 4.63 \times 10^{-4}T - 8.44 \times 10^{-7}T^2$

$k_1 = 6.34 + 7.75 \times 10^{-4}T - 9.35 \times 10^{-5}T^2$

$k_2 = 1.09 + 2.84 \times 10^{-2}T - 9.04 \times 10^{-5}T^2$

T is the temperature in Fahrenheit, h is the fractional relative humidity.

1.2.2. Fiber Saturation Point and Specific Gravity

Fiber saturation point (FSP) is the moisture content at which the cell lumens are devoid of free water (contained as liquid or vapor in the cell cavities) while the cell walls are saturated with bound water (trapped within cell walls). This definition is based on the observation that there is a transient moisture content above which the mechanical properties of wood will remain constant to some extent and below which the mechanical properties will increase when reducing the moisture content. Depending on the wood species and the properties chosen to observe, FSP might vary from one to another but the commonly accepted value for FSP is 30% according to the Wood Handbook (2010).

Specific gravity (G) is the ratio of oven-dry mass of wood to the mass of water displaced by the bulk wood at a given moisture content. It can be expressed as:

$$\boldsymbol{G = \frac{m_{od}}{V\rho_w}} \tag{4}$$

where m_{od} is the oven-dry mass of the wood; V is the moist volume; ρ_w is the density of water.

It can be seen from Equation (4) that below fiber saturation point, an increase in moisture content will cause the increase of moist volume V, thus resulting in a decrease in specific gravity. The specific gravity from moisture content w_0 to w can be determined by:

$$\boldsymbol{G = \frac{G_g}{1 - 0.01 \times S_{g-o}\% \times (30 - w)/30}} \tag{5}$$

where G_g is the green specific gravity, $S_{g-o}\%$ is the percent volumetric shrinkage from green to oven-dry state.

1.2.3. Measurement of Moisture Content

Currently, there are many methods of measuring the moisture content of wood, including the gravimetric method, Karl Fischer titration method, electrical resistance moisture meters, dielectric moisture meters, H nuclear magnetic resonance and neutron moisture meter (Skaar, 1984).

- Gravimetric method

In this method, the moist sample is weighed first, m_g, and then weighed again after oven-dry condition is reached, m_{od}. This method is quite straightforward and easy to implement, but can have several drawbacks. For instance, the existence of extractives can cause the measured moisture content value to be too high. The moisture history of the sample could also influence

the measurement. Besides these, if it is necessary to move the oven-dry sample out of the oven to weigh it, it will inevitably absorb moisture from the ambient environment, and the extent of error depends on the exposure time and the environmental conditions. However, by careful sample selection and experimental design, these errors can be minimized.

- Karl Fischer titration method

In this method, titration is performed using the Karl Fischer reagent. The end point could be determined either colorimetrically (free iodine present) or electrically (the conductivity of the solution). It is said that this method could give the best results of any standard methods (Kollmann and Höckele, 1962). However, there is one major problem - it can't be applied to large wood samples especially when the moisture content is high.

- Electrical resistance & dielectric moisture meters

These methods are based on the electrical properties of the moist wood sample. The measurement procedures are quite simple and therefore they've been accepted by industry to measure moisture contents within the range of 6~25%. However, the methods don't provide reliable results for research work (SKAAR, 1984).

- Other non-destructive methods

  With the recent development of computer technology and increasing availability of CT scanning (Baettig et al., 2006), NMR (Almeida et al., 2007; Riggin et al., 1979), and neutron imaging (Sonderegger et al., 2010), non-destructive methods to measure the moisture content profiles have gained more and more interest. The advantages are obvious, such as the non-destructive nature (which could allow the sample to be used for

consecutive observation) and high resolution (with pointwise moisture data). However, it also suffers from several drawbacks: it is very expensive, complex, and might also be very slow.

1.3. Wood Adhesives

The utilization of wood adhesives is of tremendous importance in the development and growth of the wood industry, as more than two-thirds of the wood products worldwide are bonded together, completely or partial, by a variety of adhesives. Adhesives have played and will continue to have an indispensable role in the efficient utilization wood resources (Frihart, 2015). Despite the many decades of use and numerous publication devoted to it, many aspects of wood adhesives and wood adhesion remain to be investigated due to the anisotropy of wood structure and the complexity of the interactions between wood and adhesives. In addition, since wood adhesives are designed for specific uses, there are huge amounts of products available in the market and can be divided into dozens of subgroups. Therefore, a thorough summary of wood adhesives is beyond this paper's scope. This paper only provides basic generalizations of the topic in order to help readers better understand it. Interested readers can find more details in the literature (Brief, 1990; Petrie, 2007).

Generally, three steps are involved in the adhesive application in wood. The first step is the preparation of the wood surface to provide better interaction between adhesive and substrate. The preparation could be mechanical and/or chemical treatment. The second step is the formation of a molecular-level contact between adhesive and the wood surface, which is the prerequisite to the formation any type of bond. In order to obtain a better bond formation, adhesive in liquid form is preferable. This step involves the science of surface energy and rheology. The third step is adhesive setting or curing which involves one or more of three

mechanisms: loss of solvent by evaporation and/or diffusion into wood, chemical polymerization to form cross-linked structure, and cooling of the molten adhesive (Risbrudt et al., 2005).

Once formed, the adhesive bond in wood products can transfer and distribute both external and internal loads between components, therefore increasing the wood products' stiffness and strength properties. The performance of the adhesive bond depends not only on factors during the application process (for instance wood anatomy, adhesive type, assembling pressure, surface energy, initial moisture content and so on) but also on conditions in service such as temperature and moisture changes. Wood adhesives like urea formaldehyde are known to depolymerize at high moisture levels, while phenol- and resorcinol- formaldehyde adhesives are able to maintain their adhesion to wood and do not change much under high moisture conditions. To better understand the adhesive bond, an imaginary chain across the bond was proposed by Marra (Marra, 1992), as illustrated in Figure 2.2.

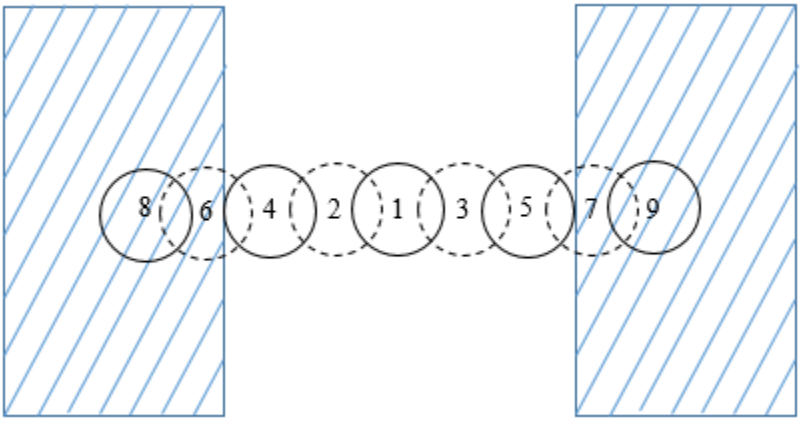

Figure 2.2. Imaginary links of adhesive bond in wood from Link 1 to 9: Link 1 is the adhesive film; Link 2 and 3 are intraadhesive boundary layer; Link 4 and 5 are adhesive-adherent interface; Link 6 and 7 are adherent (wood) subsurface; Link 8 and 9 are bulk adherent (dashed links are most vulnerable to weak formation) (Marra, 1992).

In this imaginary chain, link 1 is the unaffected adhesive film. Link 2 and 3 are adhesive boundary layers which may have been affected by the substrate (in this case, wood) and is no longer homogenous. Link 4 and 5 are adhesive-adherent (wood) interfaces in which the adhesion

mechanism (includes mechanical interlocking, covalent bond and/or secondary chemical forces) happens. Link 6 and 7 are adherent (wood) subsurfaces, in which wood cells have been modified by the preparation or bonding process. Lastly, link 8 and 9 are the unaffected wood layers.

The adhesive bond was initially characterized with only three links (1, 8 and 9): two wood pieces and one adhesive in the middle. With the recognition of basic attachment mechanisms between wood and adhesive (Link 4 and 5), it was expanded to five links (1, 4, 5, 8 and 9). Then, in order to recognize the influence of wood immediately under the surface, two more links were added (Link 6 and 7, dashed circle indicates the vulnerability to weakness). The final two links (Link 2 and 3, dashed circles) were added to emphasize the potential weakness resulting from the possible inhomogeneous glueline due to the influence of wood on some of the adhesive ingredients. These four dashed links (2, 3, 6 and 7) represent the potential weaknesses that troubles most gluelines.

Marra (1992) proposed that adhesive penetration influences links 4 to 7, or in other words, the potential adhesion mechanisms are influenced by adhesive penetration. Due to the penetration of adhesive and the anisotropic nature of wood, the bond region is an uneven layer as shown in Figure 2.3. More details regarding wood adhesive penetration can be found in the literature (Frihart, 2004; Marcinko et al., 1998; Pizzi, 1994).

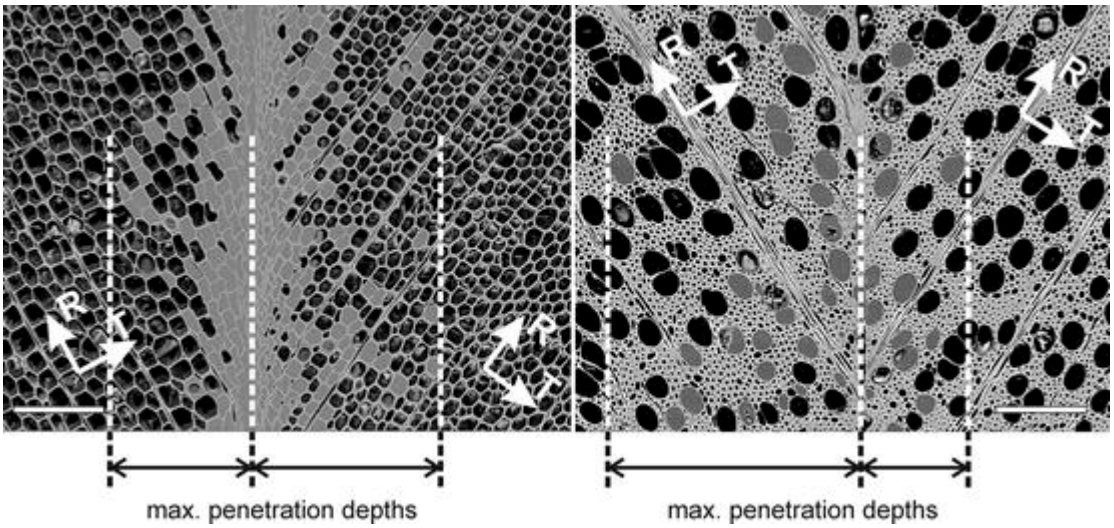

Figure 2.3. SEM images of polyurethane (PU) bond lines in wood: (Left) spruce; (Right) beech. The white bar length represents 200 um (Hass et al., 2012).

1.4. Moisture Transport in Wood and Wood Adhesives

As a hygroscopic material, **wood** absorbs or loses water according to the ambient environmental conditions. This could lead to swelling or shrinking of wood products, which as a result could cause a series of problems, such as checks on the surface, warping, loss of thermal insulation capability, and so on. Worse still, when water accumulates in wood and moisture content reaches 20% or above, it could cause favorable decay conditions.

At moisture contents below the fiber saturation point, moisture transport in wood is governed by diffusional processes: bound water diffusion in cell walls and water vapor diffusion in the cell lumen (Siau, 1995). Although several approaches exist to model this process, the most common one is to use the Fickian diffusion law. For the study of cross-laminated timber (CLT) panels, only the diffusion process in the transverse (tangential or radial) direction is considered, which is a reasonable simplification based on the comparison of the thickness with the width or

length of the CLT panels. That is to say, only a one-dimensional diffusion process is considered here.

Fick's first law for one-dimensional (x direction) steady state diffusion can be expressed as:

$$\boldsymbol{J_x = -D\frac{dC}{dx}} \tag{6}$$

where J_x is the mass flux, or the rate of mass transfer per unit area in the x-direction; D is the diffusion coefficient; C is the concentration of the diffusing substance; dC/dx is the concentration gradient in the x direction.

Several alternative gradients have been mentioned in the literature, such as chemical potential, partial vapor pressure and others (Siau, 1995). In the case of moisture content gradient as the driving force, it is necessary to convert between water concentration and moisture content by the following two equations:

$$\boldsymbol{C = \frac{m_w}{V} = \frac{wm_{OD}}{100V}} \tag{7}$$

and

$$\boldsymbol{G = \frac{m_{OD}}{V\rho_w}} \tag{8}$$

where m_w is mass of water in wood; w is the moisture content; m_{OD} is the oven dry wood weight; V is the moist volume of wood; G is the specific gravity; ρ_w is the density of water. Then the water concentration can be expressed as:

$$\boldsymbol{C = \frac{wG\rho_w}{100}} \tag{9}$$

Thus, Fick's first law of diffusion can be written in terms of moisture content as:

$$\boldsymbol{J_x = -D\frac{dC}{dx} = -D\frac{d\left(\frac{wG\rho_w}{100}\right)}{dx}} \tag{10}$$

When the specific gravity G is constant or the average is used, the above equation can be reorganized as:

$$\boldsymbol{J_x = -D\frac{d\left(\frac{wG\rho_w}{100}\right)}{dx} = -D\frac{G\rho_w}{100}\frac{dw}{dx} = -K_m\frac{dw}{dx}} \tag{11}$$

where $K_m = D\frac{G\rho_w}{100}$ is the moisture conductivity coefficient.

For one-dimensional unsteady state diffusion, moisture transfer is given by:

$$\boldsymbol{\frac{\partial C}{\partial t} = \frac{\partial}{\partial x}\left(D\frac{\partial C}{\partial x}\right)} \tag{12}$$

For a constant diffusion coefficient, the above equation can also be expressed using moisture content gradient as:

$$\boldsymbol{\frac{\partial w}{\partial t} = D\frac{\partial^2 w}{\partial x^2}} \tag{13}$$

Although this simplification is very helpful, this is not the case in a real scenario. Diffusion coefficient is affected by many factors, such as temperature, moisture content, density

and grain orientation. For example, the diffusion coefficient is found to increase with temperature and moisture content. Part of the reason might be the decrease in the activation energy for moisture diffusion in the cell wall with increasing temperature (Skaar, 1984).

The dependency of diffusion coefficient on moisture content can be expressed in an exponential form (Gereke, 2009; Hanhijärvi, 1995; Toratti, 1994):

$$\boldsymbol{D = ae^{bw}} \tag{14}$$

where a, b are constants; *w* is the moisture content.

By applying equation (11), (14) and assuming a constant, c, for the flux under steady state, for any location across the thickness, x, a following equation can be obtained:

$$-\frac{\boldsymbol{G\rho_w}}{\boldsymbol{100}}\boldsymbol{ae^{bw}}\frac{\boldsymbol{dw}}{\boldsymbol{dx}} = \boldsymbol{c} \tag{15}$$

Rearrange and integrate equation (15):

$$\int e^{bw}dw = \int -\frac{100c}{aG\rho_w}dx \tag{16}$$

$$e^{bw} - e^{bw_0} = -\frac{100bc}{aG\rho_w}(x - x_{0)} \tag{17}$$

$$w = \frac{1}{b}ln\left(e^{bw_0} - \frac{100bc}{aG\rho_w}(x - x_0)\right) \tag{18}$$

where w_0 is the moisture content at location x_0. An approximately linear relationship can be found when w is plotted against x, or in other words, $\frac{dw}{dx} \approx constant$, which is similar with

Popper's work (Popper, Niemz, & Eberle, 2004). This leads to a constant moisture diffusion coefficient in steady state.

There are generally two ways to measure moisture diffusion coefficient in wood: the cup method (steady state) and the unsteady-state method. Examples can be found in the references (Siau, 1995; van Meel et al., 2011; Wadsö, 1993a).

1.4.1. Microscopic Level Transverse Moisture Diffusion Model in Wood

In most moisture transport processes below the Fiber Saturation Point, there will be fluxes through cell wall substances and through the air in lumens. In order to study the transverse diffusion in wood, a simplified single cell model was proposed by Siau (1970), as shown in Figure 2.4. The wood cell has unit overall dimensions. This model is also assumed to be applicable to thermal and electrical conductivity, and dielectric behavior for all longitudinal cells such as tracheids, fibers and vessels.

The analysis of this model is in a manner that is analogous to a series-parallel electrical circuit, as illustrated in Figure 2.5. The cross walls are combined as Section (1) with a length of (1-*a*) in the flow direction and a unit width; similarly, the side walls are also combined in Section (3) with a length of *a* in the flow direction and a width of (1-*a*); the lumen is a square with the side dimension of *a*.

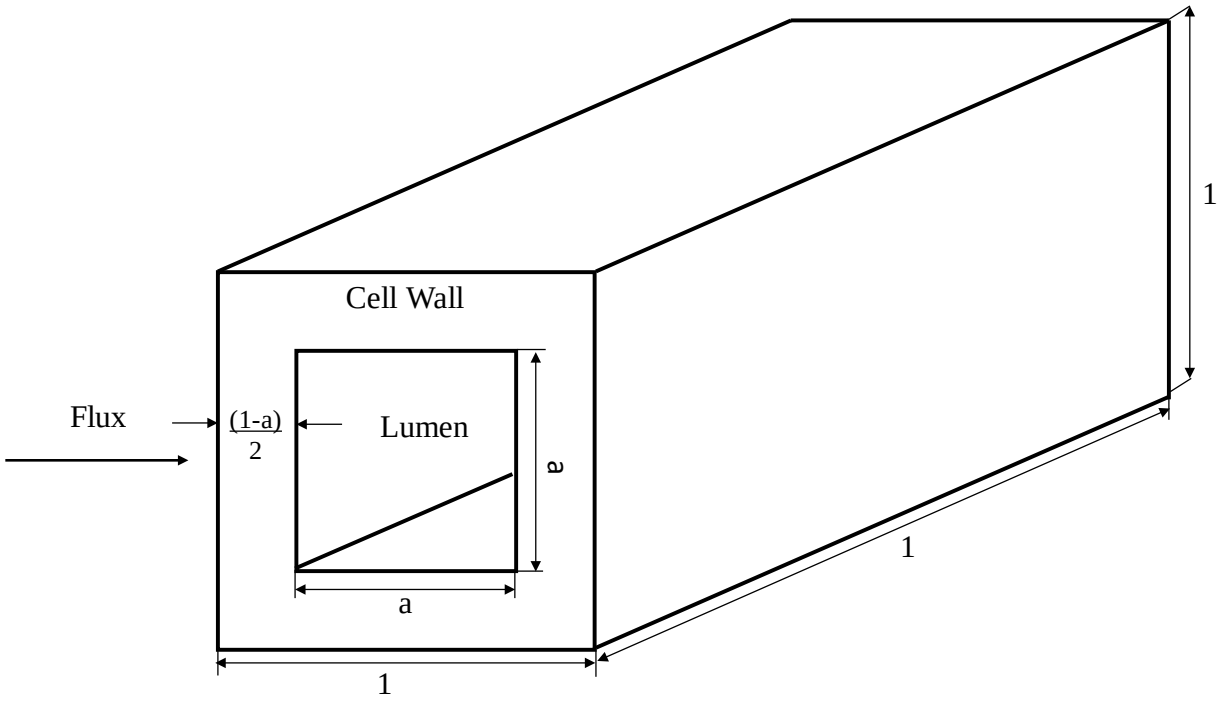

Figure 2.4. Single cell geometrical model (Siau, 1984).

The resistance of the circuit in can be determined as:

$$\boldsymbol{R_T = R_1 + \frac{1}{1/R_2 + 1/R_3}} \qquad (19)$$

where R_T is the resistance of wood in the transverse direction; R_1, R_2 and R_3 are the resistance of cross walls, lumen and side walls, respectively.

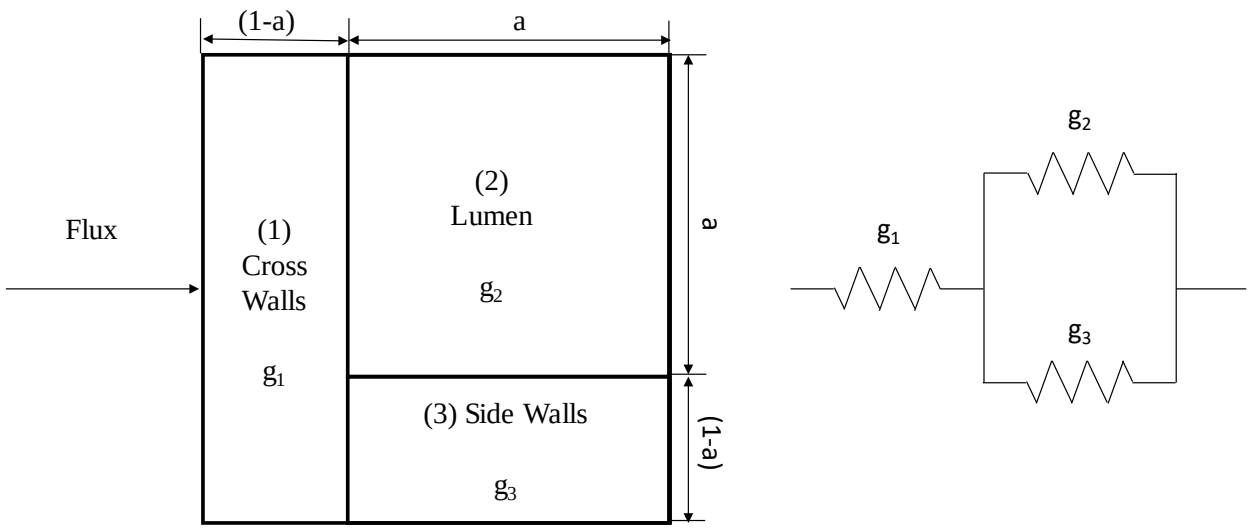

Figure 2.5. Transverse conductivity model (left) and the analogous electrical model (right) (Siau, 1984).

Equation (19) can also be expressed in conductance form:

$$\frac{\mathbf{1}}{\boldsymbol{g_T}} = \frac{\mathbf{1}}{\boldsymbol{g_1}} + \frac{\mathbf{1}}{\boldsymbol{g_2 + g_3}} \tag{20}$$

$$g_T = D_T,\ g_1 = \frac{D_{BT}}{(1-a)(1-a^2)}\ , g_2 = \frac{D_V}{(1-a^2)},\ g_3 = \frac{D_{BT}(1-a)}{a(1-a^2)}$$

where D_T, D_{BT}, D_V are the transverse moisture diffusion coefficient in a single wood cell, transverse bound-water diffusion coefficient in the cell wall, and water vapor diffusion coefficient in bulk air, respectively. The factor ($1-a^2$) is the volume fraction of cell wall substances in wood.

The bound water diffusion coefficient of wood in transverse direction (D_{BT}) is significantly lower than that in air (D_v), with the ratio of D_v to D_{BT} ranging from 20 to 2000. Thus Equation (20) can be simplified as:

$$\frac{\mathbf{1}}{\boldsymbol{g_T}} = \frac{\mathbf{1}}{\boldsymbol{g_1}} + \frac{\mathbf{1}}{\boldsymbol{g_2}} \tag{21}$$

The transverse diffusion coefficient of a single wood cell can therefore be determined as:

$$\boldsymbol{D_T} = \frac{\mathbf{1}}{(\mathbf{1} - \boldsymbol{a^2})} \frac{\boldsymbol{D_{BT} D_V}}{\boldsymbol{D_{BT}} + \boldsymbol{D_V}(\mathbf{1} - \boldsymbol{a})} \tag{22}$$

When D_v is sufficiently larger than D_{BT}, equation (22) can be simplified further to the form

$$\boldsymbol{D_T} = \frac{\boldsymbol{D_{BT}}}{(\mathbf{1} - \boldsymbol{a^2})(\mathbf{1} - \boldsymbol{a})} \tag{23}$$

When it comes to cross-laminated timber (CLT), gluelines will be formed during the manufacturing process. As mentioned in Section 1.3, adhesives will penetrate into and interact with the wood substrates to form a resin-rich region. This resin-rich region is less conductive to moisture than the non-resinated region, therefore a geometrical model similar to Siau's model was developed by Tanaka (2012), as shown in Figure 2.6:

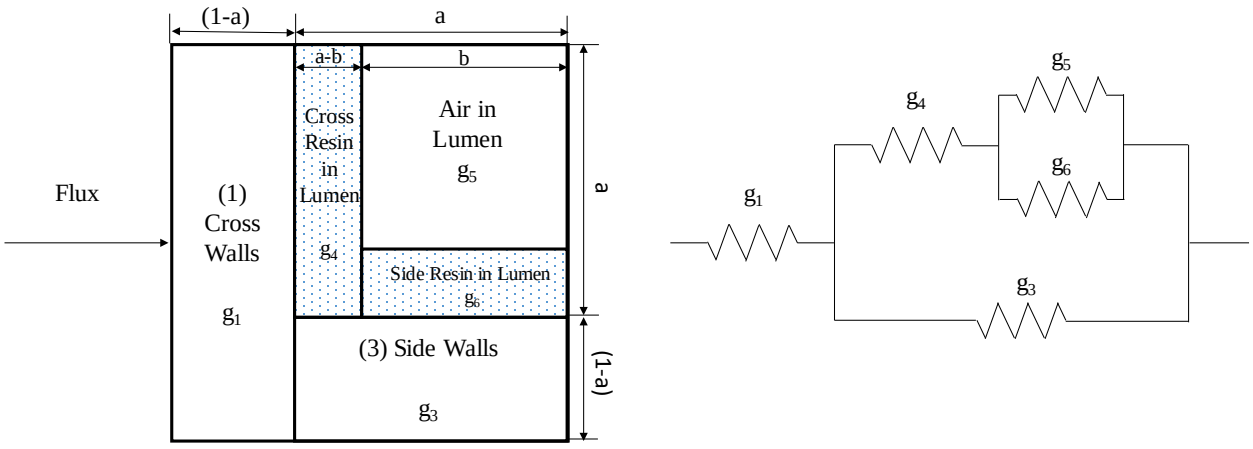

Figure 2.6. Transverse conductivity model for resin-rich region with five sections (g_1, g_3, g_4, g_5 and g_6) and the corresponding analogous electrical circuit.

This model has five sections: the cross wall conductivity, g_1; the side wall conductivity, g_3; the cross resin conductivity, g_4; the air conductivity in lumen, g_5; and the side resin conductivity, g_6. Similarly, we have:

$$\frac{\mathbf{1}}{\boldsymbol{g_{rr}}} = \frac{\mathbf{1}}{\boldsymbol{g_1}} + \frac{\mathbf{1}}{\boldsymbol{g_2' + g_3}} \tag{24}$$

$$\frac{1}{g_2'} = \frac{1}{g_4} + \frac{1}{g_5 + g_6} \tag{25}$$

where g_{rr} is the transverse resin-rich region conductivity; g_2' is the lumped conductivity of lumen; g_4, g_5 and g_6 are the conductivity of cross resin, air in lumen and side resin respectively.

Two fundamental assumptions were made for this model: 1, high wettability between cell wall and the resin; 2, very low vapor permeability of the resin. To meet the first assumption, all tracheid lumens in the resin-rich region should be filled with resin, or at least covered with a thin film of resin. Based on the second assumption, phase transition between bound water and vapor at cell wall-lumen interface should be rare, therefore the lumped conductivity of the lumen, g_2', can be considered to be negligible:

$$\frac{\mathbf{1}}{\boldsymbol{g_{rr}}} = \frac{\mathbf{1}}{\boldsymbol{g_1}} + \frac{\mathbf{1}}{\boldsymbol{g_3}} \tag{26}$$

Substituting g_1, g_3 into Equation (26):

$$\boldsymbol{D_{rr}} = \boldsymbol{g_{rr}} = \frac{\boldsymbol{D_{BT}}}{\mathbf{1} + \boldsymbol{a^3}} \tag{27}$$

where D_{rr} is the transverse bound water diffusion coefficient of the resin-rich region.

1.4.2. Macroscopic Level Transverse Moisture Diffusion Model in Cross-Laminated Timber

As mentioned in Section 1.3, during the manufacturing of CLT, adhesives penetrate into the wood and form a thin interface layer thereafter. One-dimensional steady state moisture transfer in CLT can be viewed as a multilayer diffusion process. As shown in Figure 2.7, the CLT panel consists of five layers (top layer, middle layer and bottom layer) and two adhesive layers (adhesive layer 1 and adhesive layer 2).

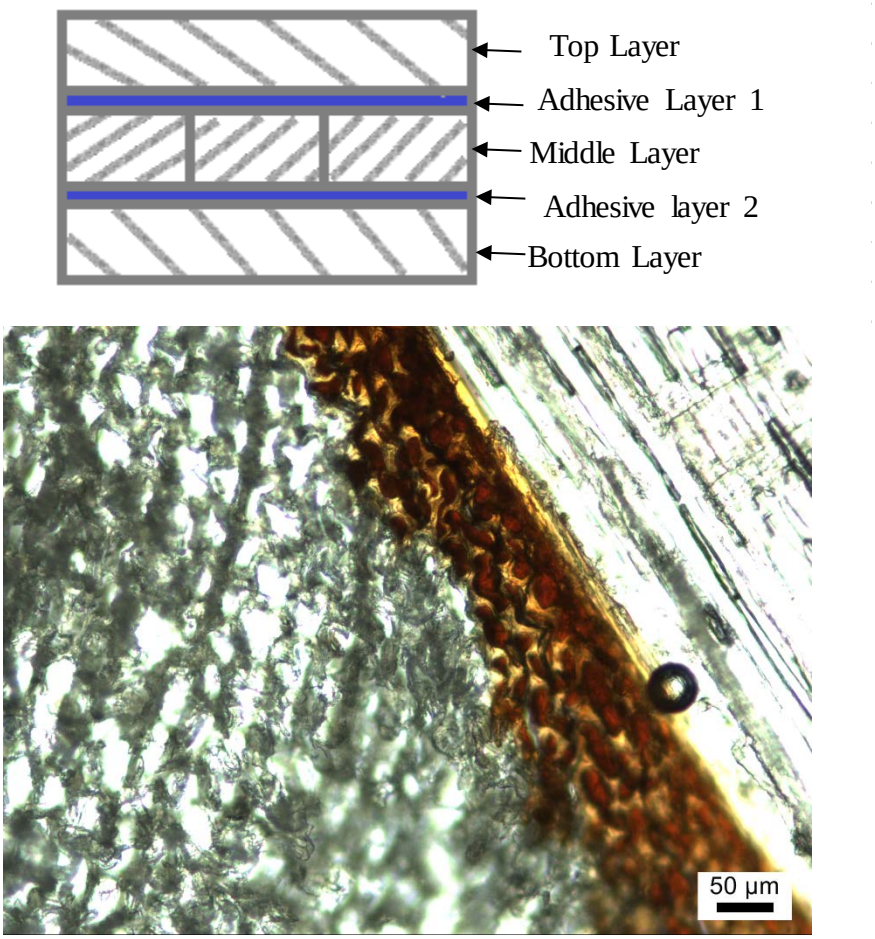

Figure 2.7. Simplified illustration of CLT and Microscope Images of gluelines for multilayer diffusion analysis.

An electric analog model is used here to calculate the theoretical diffusion coefficient. The diffusion resistance for a given substance can be expressed as $\Delta x/K_m$, which is easy to see when Fick's law is reorganized as follows:

$$\boldsymbol{J_x = -K_m \frac{dM}{dx} = -\frac{\Delta M}{\Delta x/K_m}} \tag{28}$$

Assuming the diffusion coefficient (using moisture content gradient) is constant in each layer, namely K_{m1}, K_{mA1}, K_{m2}, K_{mA2}, K_{m3} as a sequence, then the diffusion resistance for each layer can be written as $\Delta x_1/K_{m1}$, $\Delta x_{A1}/K_{mA1}$, $\Delta x_2/K_{m2}$, $\Delta x_{A2}/K_{mA2}$, $\Delta x_3/K_{m3}$, where Δx is the thickness for each layer.

Then the overall diffusion coefficient of the whole CLT panel could be calculated:

$$J_x = -\frac{\Delta M}{\Delta x/K_{mo}} = -\frac{\Delta M}{\Delta x_1/K_{m1} + \Delta x_{A1}/K_{mA1} + \Delta x_2/K_{m2} + \Delta x_{A2}/K_{mA2} + \Delta x_3/K_{m3}}$$

$$\boldsymbol{K_{mo} = \frac{\Delta x_1 + \Delta x_{A1} + \Delta x_2 + \Delta x_{A2} + \Delta x_3}{\Delta x_1/K_{m1} + \Delta x_{A1}/K_{mA1} + \Delta x_2/K_{m2} + \Delta x_{A2}/K_{mA2} + \Delta x_3/K_{m3}}} \quad (29)$$

1.4.3. Moisture Diffusion in Adhesives

As for the **adhesives** in wood, when water moves inside the wood, the glue line can be viewed as a water vapor diffusion barrier which is responsible for the moisture gradient development inside the wood composite (Pizzi and Mittal, 2003). Due to the complexity of wood anatomy and wood-adhesive interface formation, and the difficulty of isolating and analyzing them, literature on moisture transport through the glueline is limited. In order to understand the mechanism of diffusion in wood adhesives, there exist plenty of publications in which adhesive films were prepared and studied separately. One of the most common techniques for studying the diffusion of small molecules in polymer is sorption kinetics methods. It was found that at early stages, the diffusion process can be approximated by Crank and Park's diffusion equation (Park & Crank, 1968):

$$\boldsymbol{E = \frac{M_t}{M_\infty} = \frac{4}{d}\sqrt{\frac{Dt}{\pi}}} \quad (30)$$

where E is the dimensional sorption; M_t is the amount of water absorbed at time t; M_∞ is the amount of water absorbed at equilibrium; D is the diffusion coefficient; d is the thickness.

Long (1960) performed the conventional weight gain experiment to study the diffusion of methyl iodide vapor into PVA (polyvinyl acetate) film at two different temperatures, and used microradiographic procedure to measure the concentration gradients resulting from the diffusion process. In that study, it was found the surface concentration changes slowly and varies with time according to its proposed equation, therefore inferred that assuming the dependence on time and a constant diffusion coefficient, explicit solutions for Fick's Law can be obtained for diffusion both into an initially dry polymer and a preequilibrated polymer (Long and Richman, 1960).

Smith and Fisher (1984) studied the water absorption in melamine formaldehyde (1:2 mole ratio) resins and found that although the diffusion process is non-Fickian (due to the irreversible stress relaxations and structural degradation caused by the absorbed water), it still can be quantitatively described by introducing a stress relaxation factor.

More recently, Wimmer chose six commercial wood adhesives to study the water sorption mechanisms. In the study, it was found that PRF showed the lowest diffusion coefficient with a total weight gain of around 20%. Based on the results, it was concluded that water sorption mechanisms can be driven by: (1) the available free volume in the polymer and (2) the interacting ionic groups of the polymer chain (Wimmer et al., 2013).

1.5. One-dimensional Hygrothermal Building Envelope Simulation

Due to advantages such as sustainability, excellent strength and stiff properties, and good insulation performance, wood products (including CLT) have received wide acceptance in the construction field. However, being a hygroscopic material, the ability to absorb moisture increases the risk of moisture accumulation and mold-related damage in wood-frame structures.

Therefore the evaluation of hygrothermal performance of wood products (in this study, southern pine CLT) would be of great importance.

WUFI Pro, a program for one-dimensional heat and moisture transfer, is widely used for hygrothermal building envelope evaluation. It can calculate dynamic hygrothermal behaviors on the cross sections of building components by using real climatic data and offer predictions like possible condensation issues, construction moisture drying time, long term system performance and hygrothermal behavior of construction modifications.

1.6. State of the art research on Cross Laminated Timber (CLT)

Plenty of work on cross-laminated timber has been done in Europe over the past decades, especially in the German-speaking countries, but research in North America has just started. Currently, studies on CLT mainly focus on the **mechanical performance** of CLT panels, such as the vibration/seismic properties (Amini et al., 2014; Bogensperger et al., 2010; Ceccotti et al., 2013; Joebstl, 2010; Labonnote and Malo, 2010), the in-plane shear strength/stiffness or bending properties (Branco, et al., 2014; Brandner et al., 2013; Chen and Lam, 2013; Ido et al., 2014; Okabe et al., 2014), and the **fire resistance** performance of the structure (Fragiacomo et al., 2013; Frangi et al., 2009; Menis et al., 2012; Schmid et al., 2010). These past researches are in response to the need to accelerate the approval of product standards and the inclusion of CLT in building codes.

On the other hand, **moisture-related studies** on CLT panels have been very limited, especially those considering the thin adhesive layers. As mentioned previously, wood is a hygroscopic material and can absorb water either by water vapor diffusion from the ambient air or capillary forces from liquid water. Water accumulation could cause conditions favorable for

decay and mold. In addition, internal stresses in the wood and in the glueline due to moisture content variation could result in the occurrence of cracks which is undesirable and could lead to further structural failure (Niemz & Sonderegger, 2013). Warping is also very common when the moisture content changes. Therefore the study of moisture in CLT is of significant interest.

The majority of moisture-related CLT work was conducted by Gereke and co-investigators on European wood species (Gereke, 2009; Gereke & Niemz, 2010a; Gereke & Niemz, 2010b). In their research, they utilized simulations to help study the moisture diffusion process in spruce CLT panels by using a gravimetric method to measure the moisture content and an inverse method to calculate the moisture diffusion coefficient. It was found that the adhesive layer could provide a high moisture diffusion resistance and the diffusion across the glueline depended on the moisture concentration. The diffusion coefficient of the adhesive layer was found to decrease with increasing moisture content of adhesive layer, therefore they concluded that moisture transport through the glueline is governed by water-vapor diffusion.

2. Problem Statement and Objectives

2.1. Problem statement

Since the main purpose of building enclosures is the separation between the conditioned and unconditioned spaces, the control of heat, air and moisture flow is of vital importance. There are limited investigations with regard to moisture transfer in cross-laminated timber (CLT) panels, despite the importance of understanding this process. Although Gereke (2009) has done some studies on spruce CLT panels and also proposed a method to measure the moisture diffusion coefficient in the adhesive layers, much work remains to be done in this area.

- Moisture transfer in CLT is highly influenced by wood species. No diffusion data exist on CLT made from southern pine, the most widely planted tree species group in the U.S. and perhaps in the world.
- Gereke's work was based on only one type of adhesive, polyurethane. Additional adhesive systems such as phenol resorcinol formaldehyde and melamine formaldehyde also need to be evaluated for CLT applications.
- The hygrothermal performance of CLT building envelopes needs to be evaluated to address mold growth concerns.

2.2. Objectives

Based on the problems stated previously, the goal of the proposed study is to characterize moisture transport in a 3-layer southern pine cross-laminated timber panel. The specific objectives are to:

- Determine the diffusion coefficients of southern pine lumber, adhesive layer, and southern pine cross-laminated panel.
- Evaluate the effect of different adhesives (polyurethane, phenol resorcinol formaldehyde, and melamine formaldehyde) on the overall moisture transfer.
- Evaluate the hygrothermal performance of CLT building envelopes subjected to various boundary conditions, especially those that promote mold growth.

The hypotheses are:

- The steady-state moisture diffusion coefficient of southern pine is constant.
- Moisture diffusion coefficient in the glueline is independent of adhesive type.
- Properly designed CLT building envelopes have no mold growth issue.

3. Materials and Methods:

In order to study moisture diffusion in southern yellow pine CLT panels, flat sawn, nominal 2'×6', #2 southern yellow pine lumber with specific gravity around 0.50 at 12% moisture content was purchased from a local supplier in Raleigh, North Carolina, USA. The selection criteria for lumber were no wane, close to flat grain, no knots or just a few. Except for pieces used for sorption isotherm measurement, the lumber was planed and ripped to dimensions slightly larger than 2cm × 15cm (thickness × width) after purchase. The materials were then conditioned at 65% relative humidity (RH), 20℃ in a climate chamber. Unless otherwise specified, all laminae were randomized before sample preparations and measurements.

Since the equilibrium moisture content difference between solid wood and laminated specimen is insignificant (Gereke, 2009), only solid southern yellow pine samples were subjected to sorption isotherm measurements. Solid samples with the dimensions of 3cm × 7cm × 7cm (thickness × length × width) were prepared and conditioned at 65% RH, 20℃ in a climate chamber.

Six southern yellow pine samples machined to dimensions of 1cm × 10cm × 7cm (thickness × length × width) were equilibrated over a saturated potassium sulfate solution (97.6% RH at 20°C) in preparation for the unsteady-state diffusion experiments.

Lumber to be used for the manufacture of laminated panels was first cut and planed to dimension of 1cm × 30cm × 10cm (thickness × length × width). These were then edge glued as 1cm × 30cm × 30cm (thickness × length × width) laminae. Three layers of the laminae were then face glued in a cold press as cross-ply laminates according to procedures specified by adhesive manufacturers (see Table 2.1 for details). Each laminate was then cut to final

dimensions of 3cm × 7cm × 7cm (thickness × length × width). Three commonly used adhesives were chosen in this study, namely phenol resorcinol formaldehyde (PRF), melamine formaldehyde (MF) and polyurethane (PU). In total, 45 laminated panel specimens were made, 15 for each adhesive. Once made, the laminates were conditioned at 65% RH, 20℃ until equilibrium.

Table 2.1. Gluing specifications for each adhesive used to make the laminates in a cold press.

	glue spread (g/m^2)	glueline pressure (psi)	pressing time (hrs)
MF	0.260	140	2
PRF	0.189	150	7
PU	0.129	100	4

3.1. Sorption Isotherm Measurement

Sorption isotherm samples were conditioned in desiccators with a constant temperature of 20℃ and six steps of relative humidity by means of saturated salt solution: 9% RH (potassium hydroxide), 23% RH (potassium acetate), 59% RH (sodium bromide), 75% RH (sodium chloride), 85% RH (potassium chloride), and 97.6% RH (potassium sulfate). For each relative humidity, at least six samples were conditioned. Moisture content was measured using the gravimetric method. The moisture content was be assumed to be in equilibrium state when the difference between two moisture content measurements at intervals of 24 h is less than 0.1%.

3.2. Unsteady-state Diffusion Measurement

Six southern yellow pine samples with dimensions of 1cm × 10cm × 7cm (thickness × length × width) were first sealed on all edges with aluminum foil and placed inside desiccators at

97.6% RH at 20 ℃ until equilibrium. After measuring the thickness and initial weight, the samples were placed in an air stream of 65% RH and 20 ℃. Three fans were used to maintain sufficient air flow over the samples to eliminate surface resistance effects. The samples were weighed at specified schedule until equilibrium.

3.3. Steady-state Diffusion (Moisture Transfer) Measurement

The test setup was made according to DIN EN ISO 12572. A climate gradient of 65% - 100% relatively humidity was applied by placing the diffusion cup inside a climate chamber. Details of sample preparation and measurement are as follows:

1. Prepare and condition (at 65% RH, 20 ℃) a total of 45 laminated samples, 15 for each adhesive.
2. Seal the edges of each sample with silicone (DAP SiliconePlus) to force one-dimensional moisture movement.
3. Attach the jar cover to the jar (1qt jars from Anchor Hocking Company) using silicone sealant.
4. Add enough distilled water to the jar to have a distance of 4 cm between the water surface and the laminate bottom surface.
5. Attach the sample to the jar cover using silicone sealant, then put the whole setup into the climate chamber to maintain a 65% - 100% relative humidity gradient across the samples.
6. Divide the samples into 5 groups to conduct moisture profile measurements at 7, 14, 21, 42 and 365 days after the start of the experiment. Each group consisted of 9 samples since there were 3 replicates for each adhesive.
7. After 7, 14, 21, 42, or 365 days , remove the 9 samples from the diffusion cups, cut 1 cm from each of the four edges to minimize the edge effect, then cut the remaining into half (Figure 2.9).

8. Using a self-designed guillotine device (to avoid excessive heated generated by sawing), slice the specimen from Step 7 into 6 pieces evenly along the transverse direction (Figure 2.9).
9. Weigh specimens right away and place them into the oven for a minimum 24 hours or until no weight change. Weigh the specimens at the ovendry condition.
10. Calculate the diffusion coefficients, and use them as the inputs for following dimensional studies.

Figure 2.8. Illustration of the diffusion cup.

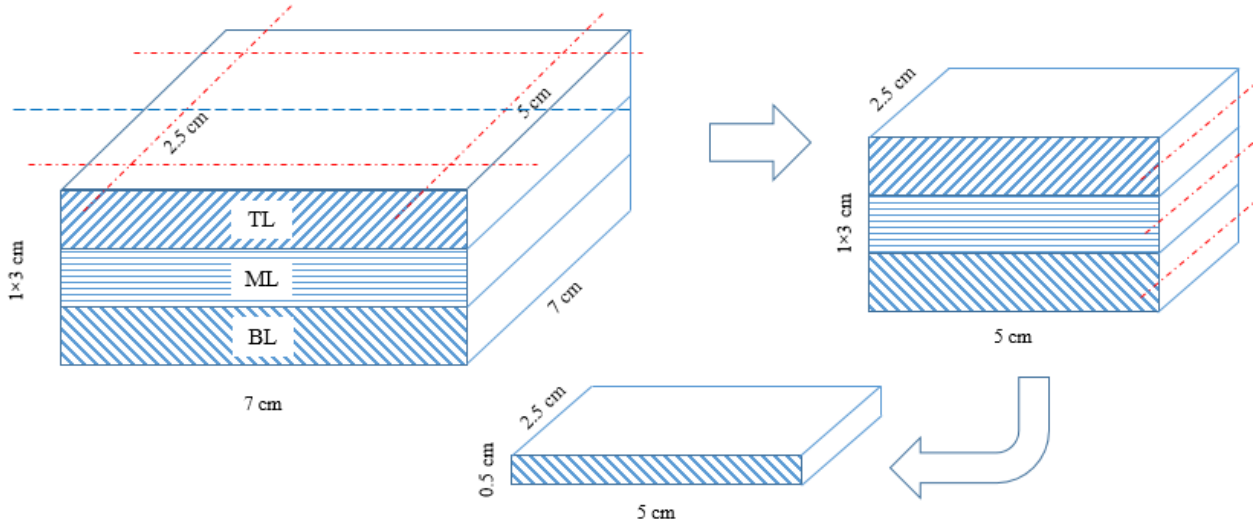

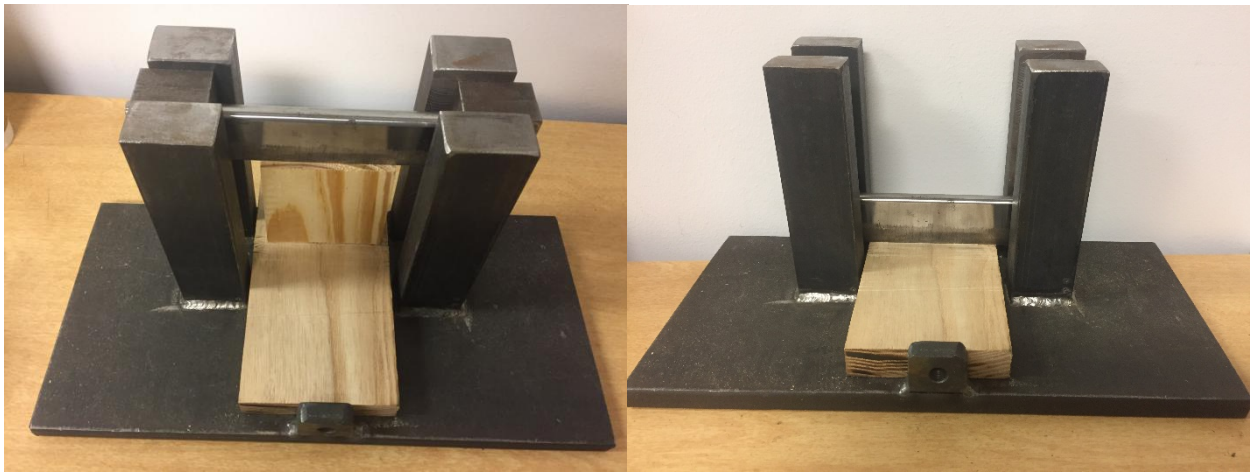

Figure 2.9. Slicing Procedures and Device for Diffusion Samples (BL is the bottom layer which is exposed to 100% RH; ML is the middle layer; TL is the top layer, which is exposed to 65% RH).

In addition to laminated specimens, 4 solid southern pine samples with the dimensions of 3.5cm × 7cm × 7cm (thickness × length × width) were prepared and sealed for 60 days, then sliced in the same manner as the laminate samples to verify linear moisture distribution along thickness direction under steady state.

4. Results and Discussion

4.1. Sorption Isotherm

Results of sorption isotherm measurements are presented in Table 2.2. Summarized data are shown in Table 2.3. The increasing standard deviations of moisture contents was assumed to be related to the inevitable system errors associated with the measurements due to the timespan between removing samples from the climate chamber or oven and the weighing. Despite this existing system error, the results were still very consistent.

The sorption behavior of the southern yellow pine samples was analyzed by the Hailwood-Horrobin (H-H) model (Hailwood & Horrobin, 1946b):

$$\boldsymbol{EMC = \frac{1800}{W}\left[\frac{kh}{1-kh} + \frac{k_1 kh + 2k_1 k_2 k^2 h^2}{1 + k_1 kh + k_1 k_2 k^2 h^2}\right]} \quad (3)$$

where EMC is the equilibrium moisture content; h is relative humidity; W, k, k_1, k_2 are equilibrium parameters related to temperature.

Since this experiment was conducted at a constant temperature (20 ℃), these temperature related parameters could be treated as constants. By minimizing the residual sum of squares, a nonlinear regression method was applied to fit the data. These constants were determined to be:

$$W = 387.459; k = 0.821;$$

$$k_1 = 5.8695, k_2 = 2.7145$$

Table 2.2. Sorption isotherm measurement results. Samples were randomized for each test condition, for instance, sample 4B3 is the 3rd block from the 2nd half (B) of the 4th lumber, 49A2 is the 2nd block from the 1st half (A) of the 49th lumber.

Potassium Hydroxide 9%RH				Potassium Acetate 23%RH			
Sample #	Weight (g)		MC (%)	Sample #	Weight (g)		MC (%)
	Before	After			Before	After	
4B3	98.213	94.651	3.76	7B1	96.089	90.408	6.28
27B1	106.791	102.879	3.80	27B12	112.587	106.115	6.10
4B2	99.628	96.000	3.78	28B20	106.691	100.634	6.02
49A2	106.813	102.879	3.82	27B11	112.127	105.668	6.11
4B1	99.104	95.536	3.73	4B27	102.123	96.289	6.06
49A6	108.830	104.916	3.73	7B2	96.934	91.179	6.31
Sodium Bromide 59%RH				Sodium Chloride 75%RH			
Sample #	Weight (g)		MC (%)	Sample #	Weight (g)		MC (%)
	Before	After			Before	After	
4B8	100.759	90.257	11.64	4B11	104.670	91.845	13.96
27B8	116.236	104.425	11.31	27B24	118.040	103.957	13.55
4B7	99.522	89.151	11.63	27B9	119.223	104.231	14.38
4B6	97.627	87.339	11.78	29A16	117.354	103.081	13.85
29A8	116.258	104.207	11.56	4B10	104.852	92.009	13.96
29A7	116.751	104.650	11.56	29A14	117.645	103.270	13.92
Potassium Chloride 85%RH				Potassium Sulfate 97.59%RH			
Sample #	Weight (g)		MC (%)	Sample #	Weight (g)		MC (%)
	Before	After			Before	After	
4B15	113.339	97.434	16.32	4B26	118.782	94.812	25.28
4B14	113.309	97.297	16.46	7B10	115.622	90.998	27.06
29A19	120.229	103.145	16.56	7B9	117.246	92.305	27.02
29A20	120.071	103.060	16.51	4B24	122.274	97.400	25.54
27B28	123.353	106.336	16.00	29A26	128.845	101.254	27.25
27B29	123.282	106.244	16.04	4B23	124.754	99.307	25.62
27B5	122.886	105.838	16.11				

Table 2.3. Summarized results for sorption isotherm.

RH (%)	MC (%)	Standard Deviation
9	3.77	0.04
23	6.15	0.12
59	11.58	0.15
75	13.94	0.27
85	16.28	0.26
97.6	26.30	0.90

The measured data and predicted values from the H-H model are presented in Figure . The typical sigmoid shape of the isotherm is clearly seen here. It can be seen that the H-H model can predict the moisture content surprisingly well. This can also be confirmed by the residual plot in

Figure , which plots the differences between the measured and predicted values. Therefore, it can be concluded that the moisture content of southern yellow pine at 20 ℃ and a given relative humidity can be calculated by the H-H model using the parameters determined in this study.

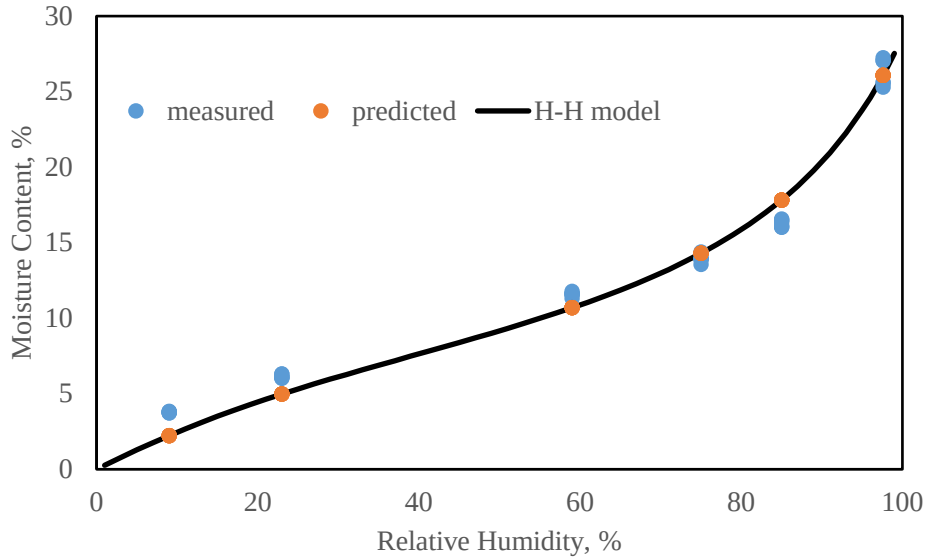

Figure 2.10. Measured and predicted data for sorption isotherm at 20 ℃.

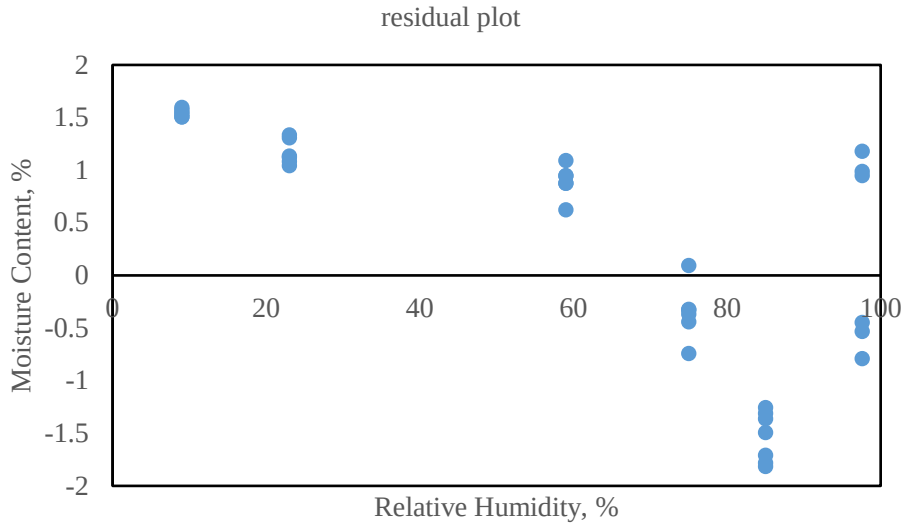

Figure 2.11. Residual plot of the H-H model.

4.2. Unsteady-state Diffusion Measurement

The unsteady-state determination of southern yellow pine diffusion coefficient was based on desorption measurements. Depending on which part of the desorption curve is used, there are two different ways to evaluate the diffusion coefficient (Neimsuwan, Wang, Taylor, & Rials, 2008; Wadsö, 1992; Wadsö, 1993b):

$$\boldsymbol{D_1 = \frac{\pi l^2}{16}\left(\frac{dE}{d\sqrt{t}}\right)^2} \quad (31)$$

$$D_2 = \frac{l^2}{\pi^2 t} ln\left(\frac{8}{\pi^2(1-E)}\right) \quad (32)$$

where D_1 and D_2 are the diffusion coefficients based on the initial linear part and on the final part of the desorption curve, respectively. The parameters l, t, and E are the thickness of the sample, time and dimensionless moisture content, respectively.

The use of D_2 is best around 60-80% of the total desorption, the weight change at this point is slower thus affects the determination of fractional weight changes. D_1 works best for the initial linear part of the measurement and can be considered as the constant coefficient at that specific moisture content.

In this study, to ease the analysis, the initial linear part of the desorption curve was chosen for calculating the diffusion coefficient. The equation for D_1 can also be rewritten as:

$$\boldsymbol{D = \frac{\pi l^2}{16}\frac{slope^2}{(W_i - W_e)^2}} \quad (33)$$

where W_i and W_e are the initial and equilibrium weight of the sample respectively; *slope* is the slope of the initial linear portion of weight loss ($W_i - W$) against $\sqrt{TIME}$ curve.

2.12 is the desorption curve for Sample 1. The slope (0.1805 g/min$^{0.5}$), thickness (1.12 cm), and weight difference (6.012 g) were used to calculate a diffusion coefficient of 3.25 x 10^{-6} cm^2/s. Unsteady-state diffusion (desorption) results are presented in Table 2.4. The average diffusion coefficient D for the six samples is 3.06×10^{-6} cm^2/s. The result agrees well with those of other researchers (Neimsuwan et al., 2008; Stamm & Nelson, 1961).

Table 2.4. Summary of the unsteady-state diffusion data.

Sample #	slope	thickness (cm)	Wi-We (g)	D (cm^2/s)
1	0.1805	1.12	6.012	3.25E-06
2	0.1738	1.10	6.128	2.803E-06
3	0.1852	1.10	6.140	3.171E-06
4	0.1879	1.09	6.393	2.971E-06
5	0.2022	1.10	6.699	3.208E-06
6	0.1963	1.09	6.690	2.976E-06

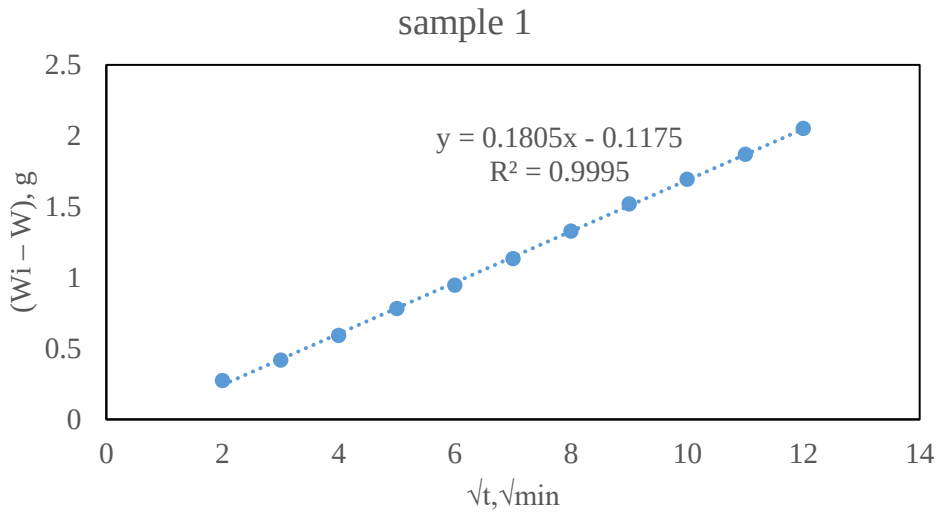

Figure 2.12. Desorption curve for Sample 1 at 20 ℃.

4.3. Steady State Diffusion in Solid Southern Pine Samples

With the aim of verifying the linear moisture content distribution along the thickness direction, solid southern pine samples were subjected to a relative humidity gradient of 100% to 65% by using the diffusion cup method for two months, and sliced thereafter to determine the

moisture content profile along the thickness direction as presented in Table 2.5. The moisture content profile is shown in Figure 2.13.

Table 2.5. Slice moisture contents from top (65% RH) to bottom (100% RH) for each solid southern pine sample.

Location (cm)	Moisture Content (%)				
	#1	#2	#3	#4	Average
3.3	13.7	12.3	11.3	12.3	12.4(1.0)
2.7	15.4	14.8	13.8	15.2	14.8(0.7)
2.1	17.1	16.6	16.4	17.2	16.8(0.4)
1.5	19.0	18.8	18.5	19.5	19.0(0.5)
0.9	21.0	20.4	19.4	20.7	20.4(0.7)
0.3	21.5	21.4	22.0	22.3	21.8(0.4)

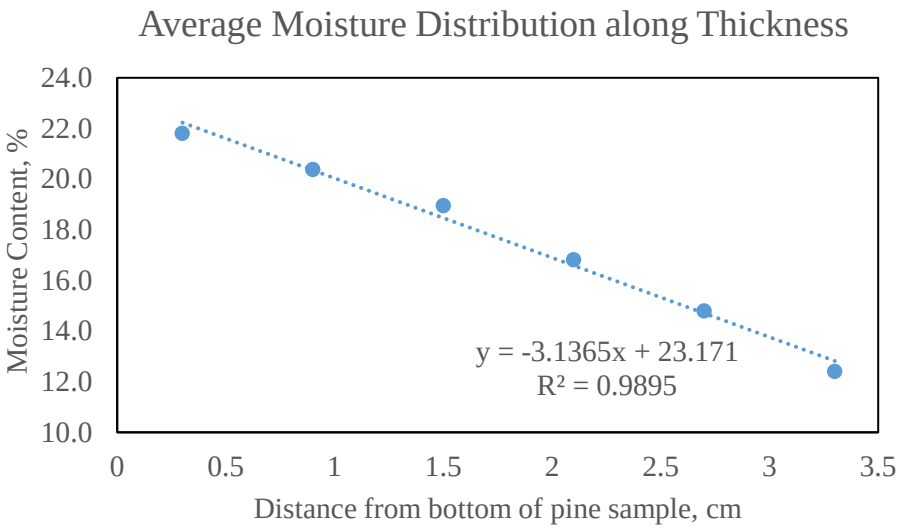

Figure 2.13. Moisture content profile in the thickness direction.

As seen in Figure 2.13, on average a linear moisture content profile along the thickness direction can be found. Therefore from Equation (11), it can be concluded that the conductivity for moisture coefficient K_m is independent of moisture content, or in other words, K_m is constant.

Simulations were also performed in COMSOL MULTIPHYSICS (Tabatabaian, 2015) to verify the linear moisture content distribution. In this simulation, moisture transport from the water surface to the outer specimen surface (shown in Figure) was modeled. The thickness of the specimen was 3.5 cm, the distance between water surface and inner specimen surface was 4.0 cm. The equilibrium moisture content at the water surface, M_s, was 28.7% (EMC at 100% RH calculated from the H-H model), the initial moisture content of the southern pine specimen was 12.0%. A constant moisture diffusion coefficient of southern pine was 3.00×10^{-6} cm^2/s (rounded from 3.06×10^{-6} cm^2/s obtained during Unsteady-state Diffusion Measurement), the moisture diffusion coefficient in still air was 7.65×10^{-6} cm^2/s (see Appendix for details). The boundary conditions were:

1. water concentration of air at the water surface was 7532 mol/m^3 (converted from 28.7% moisture content);
2. water concentration of air at the outer specimen surface was 3383 mol/m^3 (converted from 12.0% moisture content).

Details regarding the parameter calculations and conversions can be found in the Appendix.

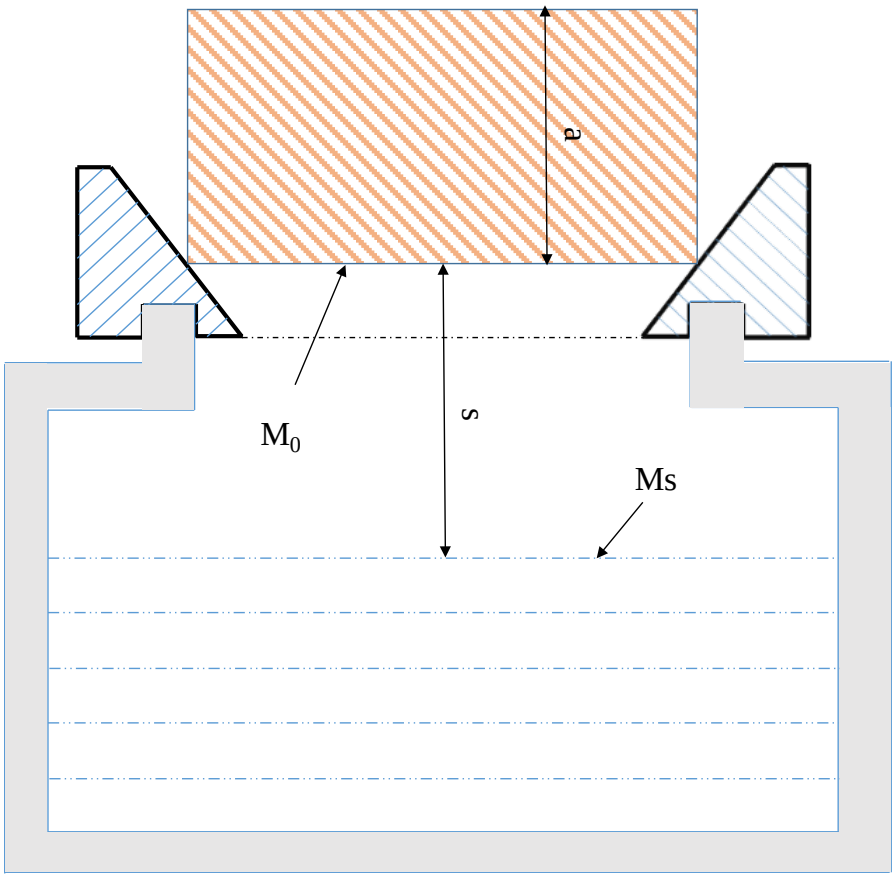

Figure 2.14. Illustration of diffusion cup parameters for COMSOL simulation: a is the thickness of solid southern pine specimen (3.5cm); s is the distance from water surface to the inner specimen surface (4.0cm); M_0 is the equilibrium moisture content at the inner specimen surface; Ms is the equilibrium moisture content at the water surface.

Using the data as input, a time-dependent study using Transport of Diluted Species model was performed to study the moisture transport process. The simulation was run from Day 0 to Day 100 at intervals of 5 days. Results are shown in Figure 2.15. The curves between 0.00 and 0.04 m represent the moisture profiles between the water surface and the inner specimen surface; curves from 0.04 to 0.075 m are the profiles for moisture transport in the southern pine specimen. It can be seen that in static air, M_0 was substantially different from Ms and increased with time until equilibrium. After 60 days, the change in moisture concentration was negligible at each location; linear moisture concentration profiles were obtained. Therefore the moisture transport process can be assumed to have reached steady state after 60 days. In Figure 2.16, the

moisture profile of southern pine from the steady state measurement is compared to that of 60 days from the model. It is obvious that data from measurement and model matched very well with each other.

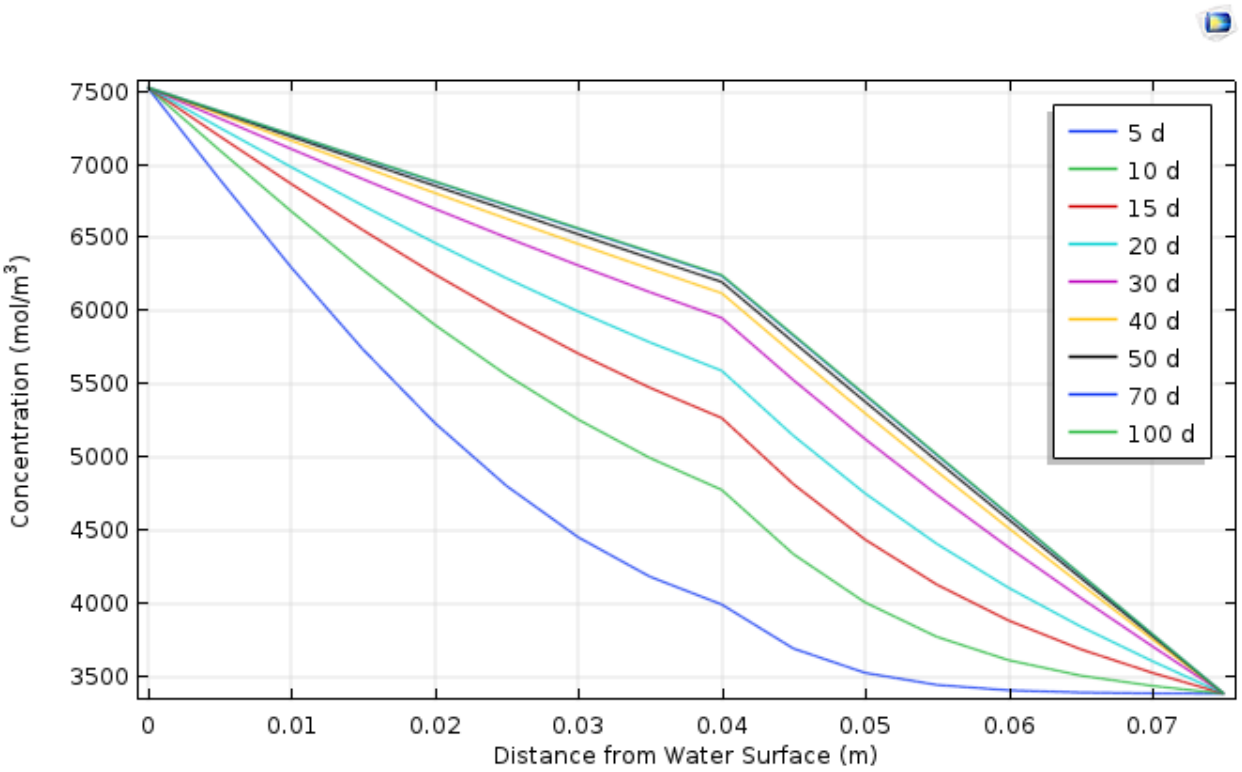

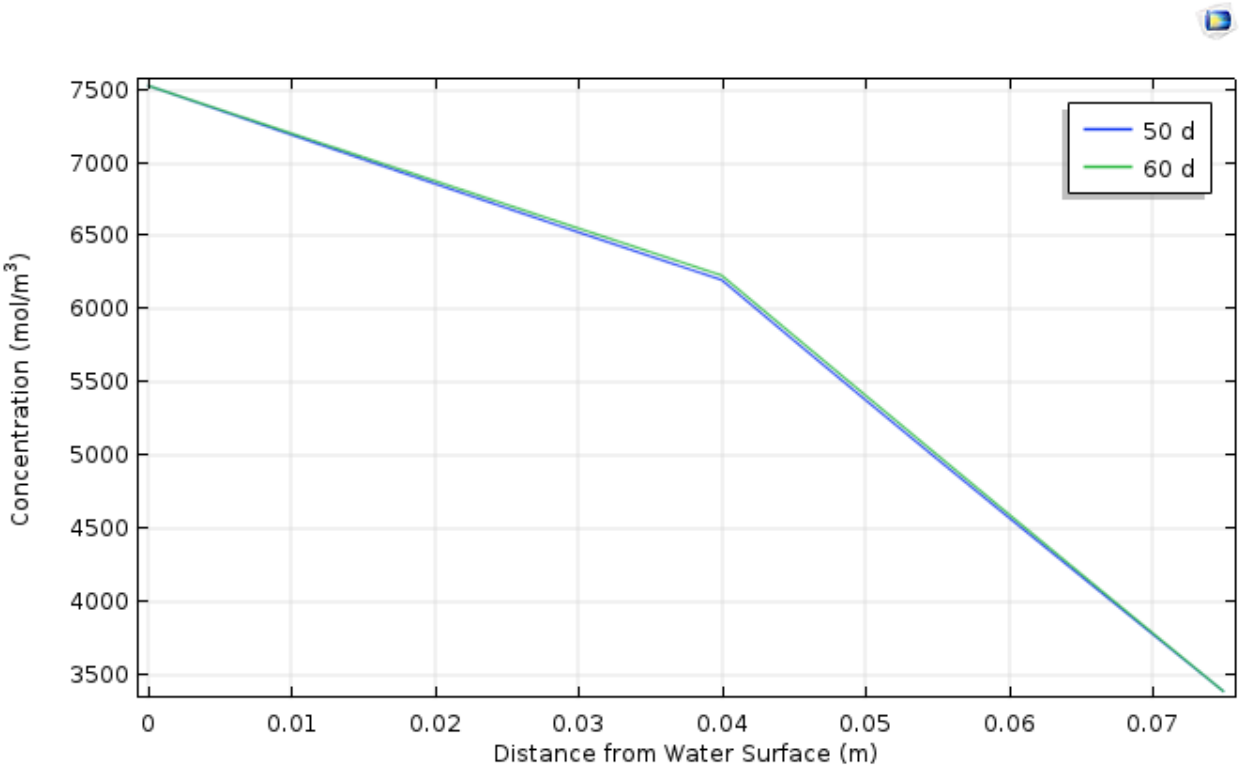

Figure 2.15. COMSOL simulation of moisture transport in a diffusion cup with an interval of 5 days.

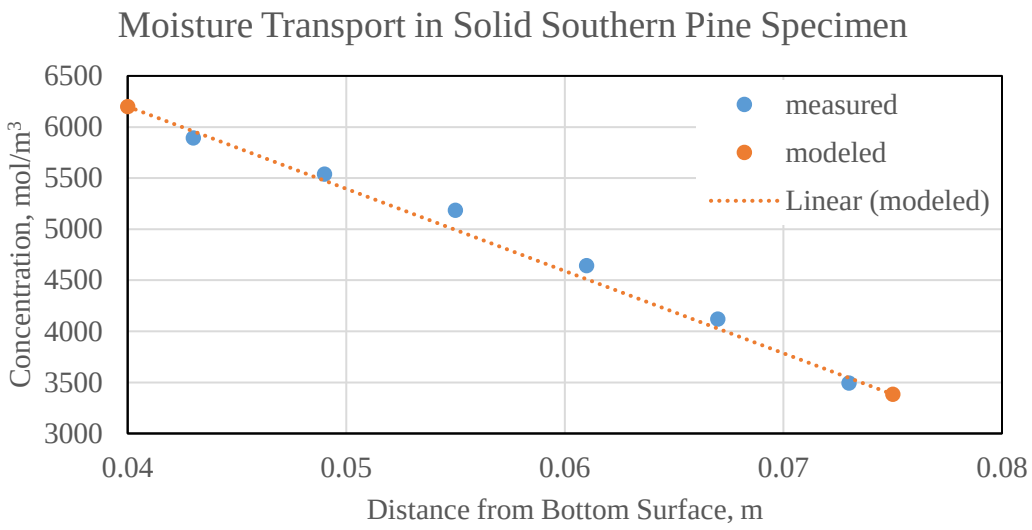

Figure 2.16. Moisture transport comparison between data from measurement and model.

Meanwhile another simplified numerical proof has been provided in Section 1.4 by using an average specific gravity of 0.51 at 12% moisture content, a better explanation of the linear moisture content profile may be obtained by adopting Equation (5):

$$G = \frac{G_g}{1 - 0.01 \times 12.3\% \times (30 - w)/30} \tag{5}$$

With the average specific gravity of 0.51 at 12% moisture content, 20 ℃, plot of specific gravity against moisture content (12% to 28%) was shown in Figure 2.17. In this figure, it showed that the relationship between specific gravity and moisture content can be well approximated by an exponential function:

$$G = 0.534e^{-0.004w} \tag{36}$$

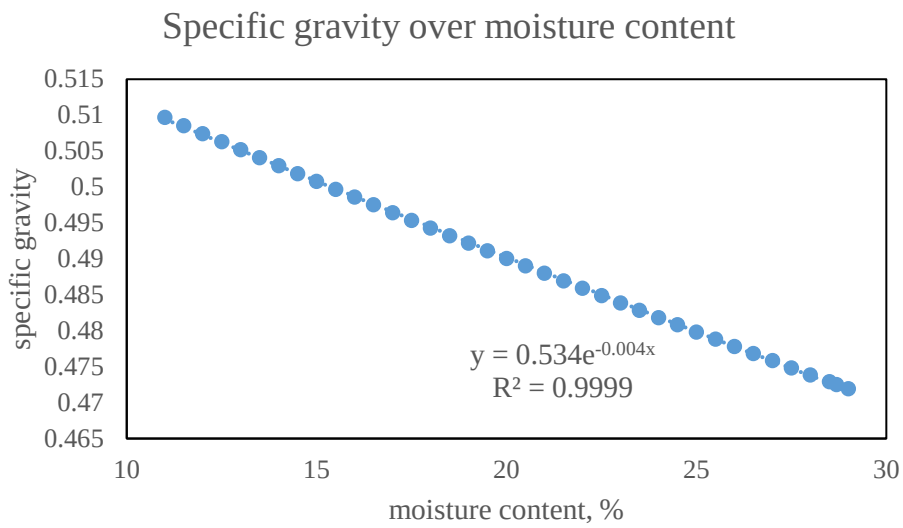

Figure 2.17. Plot of specific gravity against moisture content.

Since $K_m = \frac{DG\rho_w}{100}$ and $D = ae^{bw}$, a reasonable explanation of a constant K_m is the exponential terms in D and G cancel out each other, therefore K_m is independent of moisture content. By substituting the average diffusion coefficient of 3.00×10^{-6} cm^2/s and the specific gravity of 0.51 at 12% moisture content, conductivity for moisture coefficient K_m can be determined as:

$$K_m = \frac{DG\rho_w}{100} = 1.53 \times 10^{-8} \frac{g}{cm \cdot s}$$

4.4. Steady-State Diffusion in Laminates

Slice fractional moisture contents of the laminates are summarized in Table 2.6. Given the fact that variations between wood pieces are inevitable, it can be seen that data collected here are surprisingly consistent (small standard deviations). This is mainly due to the careful sample selection and proper experimental design.

Due to the existence of gluelines as water barriers and the applied relative humidity gradient along the thickness direction (65%/100% RH), obvious step changes in moisture content

across layers (i.e. BL to ML, ML to TL) can be observed for all samples (Table 2.6 and Figure 2.20).

The moisture contents of the top layer (Slice 5 and 6) did not change much for each sample from Day 7 to Day 42, while those of the bottom layer (Slice 1 and 2) exhibited rapid changes during the first 7 days and increased gradually thereafter. This could be well explained by the water barrier function of the gluelines. The top layer was farthest from and not in direct contact with the 100% RH environment, while the bottom layer was subjected to the 100% RH directly.

Table 2.6. Slice average moisture contents (%) from the bottom (Slice 1) to the top (Slice 6) of the laminates glued with polyurethane (PU), phenol-resorcinol formaldehyde (PRF), and polyurethane (PU) adhesives.

Slice #	7 Days	14 Days	21 Days	42 Days	1 Year
6	12.3 (0.2)	12.1 (0.4)	12.0 (0.7)	12.1 (0.2)	13.3 (0.3)
5	12.1 (0.2)	11.9 (0.5)	12.3 (0.7)	12.3 (0.6)	14.3 (0.4)
4	13.2 (0.5)	14.0 (0.5)	14.8 (0.4)	15.3 (1.5)	17.8 (0.8)
3	13.7 (0.7)	14.8 (0.8)	15.8 (0.3)	15.8 (1.3)	19.0 (0.8)
2	15.7 (0.9)	18.6 (1.1)	18.8 (1.1)	21.1 (1.3)	22.4 (1.0)
1	18.1 (0.4)	20.9 (0.7)	20.4 (0.9)	22.7 (0.8)	24.5 (1.1)
			PRF glued CLT		
Slice #	7 Days	14 Days	21 Days	42 Days	1 Year
6	12.2 (0.5)	12.8 (0.4)	12.0 (0.3)	12.4 (0.3)	13.1 (0.2)
5	12.5 (0.8)	13.2 (0.4)	12.7 (0.6)	13.2 (0.2)	14.8 (0.2)
4	13.6 (0.7)	14.4 (0.6)	15.1 (0.4)	14.6 (0.4)	18.2 (0.3)
3	14.1 (0.5)	15.7 (0.8)	16.5 (0.4)	16.5 (0.6)	19.8 (0.3)
2	16.4 (0.6)	18.2 (1.4)	18.1 (1.1)	19.5 (0.6)	21.9 (0.7)
1	19.1 (0.5)	19.9 (1.0)	20.4 (0.7)	20.7 (0.5)	22.7 (0.4)
			MF glued CLT		
Slice #	7 Days	14 Days	21 Days	42 Days	1 Year
6	12.6 (0.2)	12.8 (0.1)	12.6 (0.2)	12.5 (0.6)	13.0 (0.4)
5	13.0 (0.4)	13.3 (0.2)	14.2 (0.3)	13.2 (0.7)	15.0 (0.3)
4	13.7 (0.3)	14.3 (0.5)	14.9 (0.5)	15.7 (0.3)	17.2 (0.3)
3	14.4 (0.3)	16.0 (0.4)	16.6 (0.4)	17.0 (0.7)	17.8 (0.7)
2	16.5 (1.0)	19.0 (0.7)	19.5 (1.5)	19.1 (1.1)	22.7 (0.2)
1	19.2 (0.8)	20.6 (1.3)	21.4 (0.7)	21.2 (1.1)	24.1 (0.8)

Notes: values in the brackets are the standard deviation.

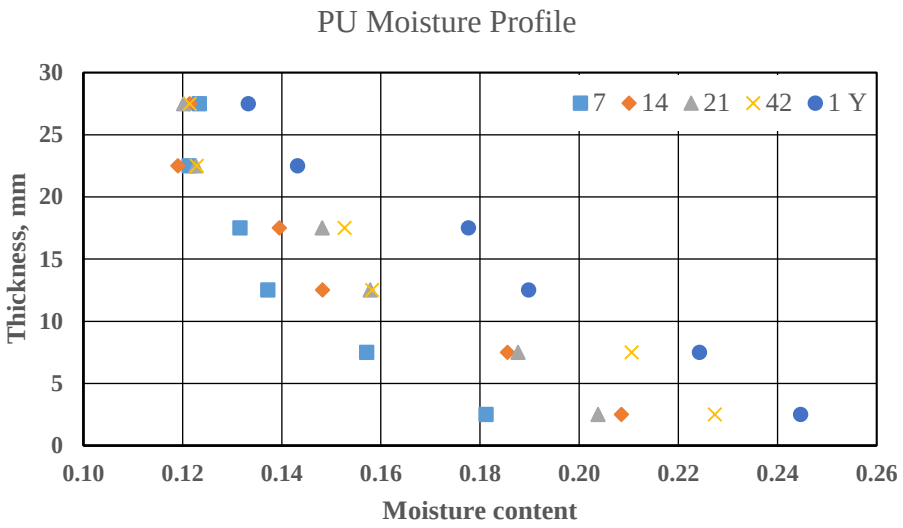

Figure 2.18. Moisture profiles (fractional) in PU-glued laminates on Day 7 (square), Day 14 (diamond), Day 21 (triangle), Day 42 (cross) and Day 365 (circle) of the diffusion cup experiment.

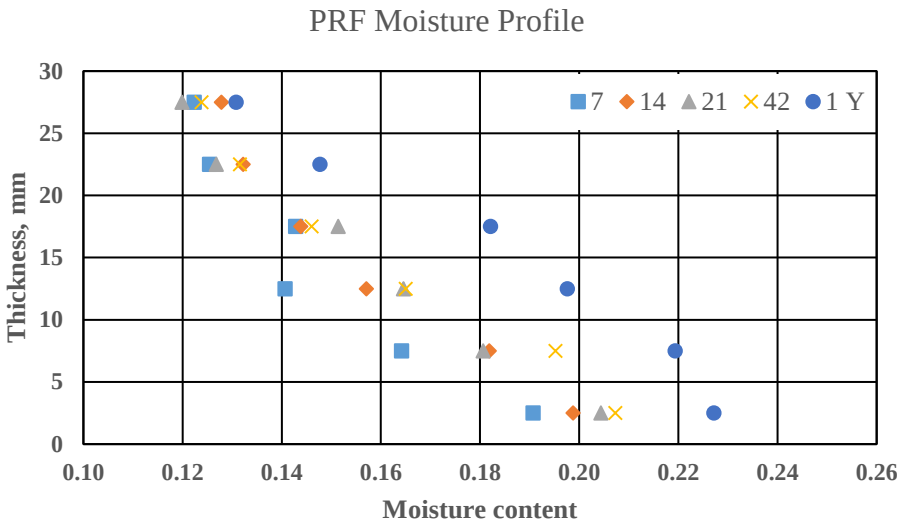

Figure 2.19. Moisture profile (fractional) in PRF-glued laminates on Day 7 (square), Day 14 (diamond), Day 21 (triangle), Day 42 (cross) and Day 365 (circle) of the diffusion cup experiment.

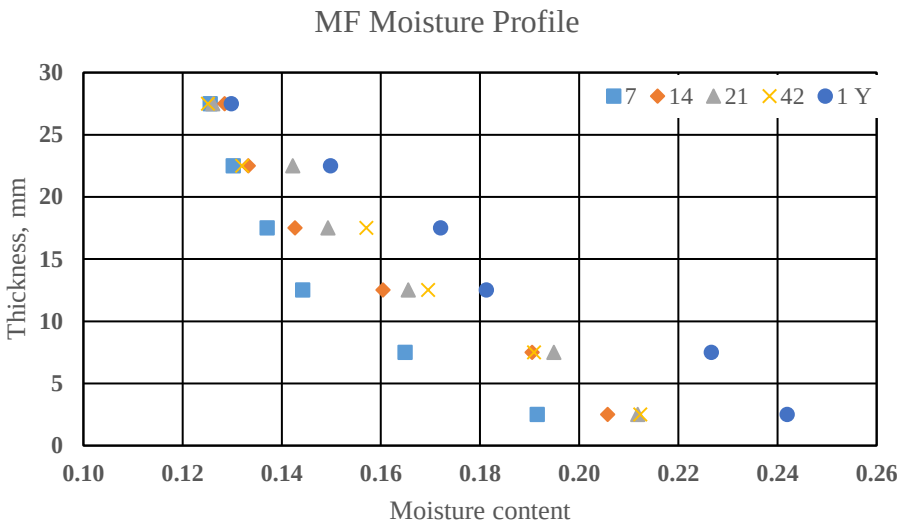

Figure 2.20. Moisture profile (fractional) in MF-glued laminates on Day 7 (square), Day 14 (diamond), Day 21 (triangle), Day 42 (cross) and Day 365 (circle) of the diffusion cup experiment.

As discussed in 1.4, the moisture diffusion in CLT can be modeled as a five-layer diffusion process. The diffusion coefficient of solid southern pine has been obtained from the unsteady-state diffusion study, with a value of 3.00×10^{-6} cm^2/s. This has been confirmed both by steady-state measurement of solid southern pine and simulation results that this diffusion coefficient can be treated as a constant during the diffusion process. The glueline diffusion coefficient, Drr, can also be determined from Equation (23) and (27) as:

$$\boldsymbol{D_T = \frac{D_{BT}}{(1-a^2)(1-a)}} \tag{23}$$

$$D_{rr} = g_{rr} = \frac{D_{BT}}{1+a^3} \tag{27}$$

$$Drr = \frac{(1-a^2)(1-a)}{1+a^3} D_T \tag{37}$$

where D_T and D_{BT} are the transverse diffusion coefficient of a single wood cell, and the transverse bound-water diffusion coefficient, respectively. D_T has the value of 3.00×10^{-6} cm^2/s as

measured from the unsteady-state diffusion study. The value of *a* can be determined from porosity (Siau, 1984):

$$\boldsymbol{Porosity = a^2 = 1 - (0.667 + 0.01 \times w) \times G} \quad (38)$$

where w is the moisture content, %; and G is the specific gravity at 12% moisture content, 20 ^{0}C. G has the value of 0.51 in this study. From Equation (38), a=0.77. Therefore the glueline diffusion coefficient at dry condition is Drr=1.93×10^{-7} cm^2/s.

The value of solid southern pine diffusion coefficients was used as input for COMSOL Transport of Diluted Species modeling. The thickness of each southern pine ply was 1.0 cm, the thickness of PRF glueline was 0.1 mm, and those of PU and MF gluelines were 0.2 mm (obtained from microtome images of these gluelines, Figure 2.7). The modeling setup were the same with the solid southern pine simulation as shown in Figure except that the solid southern pine was replaced by the southern pine laminate with a total thickness of 3.02 cm for PRF-glued laminate and 3.04 cm for the PU- and MF-glued laminates. The simulation was run from Day 0 to Day 364 with an interval of 7 days. The initial and boundary conditions were the same:

1. equilibrium moisture content at the water surface, Ms, was 28.7%;
2. initial moisture content of the southern pine laminate was 12.0%;
3. moisture diffusion coefficient in still air was 0.25 cm^2/s;
4. water concentration at the water surface was 7532 mol/m^3;
5. water concentration at the outer CLT surface was 3383 mol/m^3.

4.4.1. Constant Glueline Diffusion Coefficient

Gereke (2009) found that water diffuses through the glueline as water vapor, and that the vapor diffusion coefficient in wood decreases with increasing moisture content. Therefore, to estimate the magnitude of glueline diffusion coefficient, two extreme case were assumed:

1. $D_1 = 2 \times 10^{-7}$ cm^2/s when glueline stays dry;
2. $D_2 = 2 \times 10^{-8}$ cm^2/s when glueline gets wet.

Simulation results for PU-glued laminates using D_1 are presented in Figure 2.21 and 2.22. It can be seen that although the simulation results fitted well for the middle and top layers, the bottom layer moisture content was lower than the experiment data. Therefore, the glueline diffusion coefficient should be smaller than D_1.

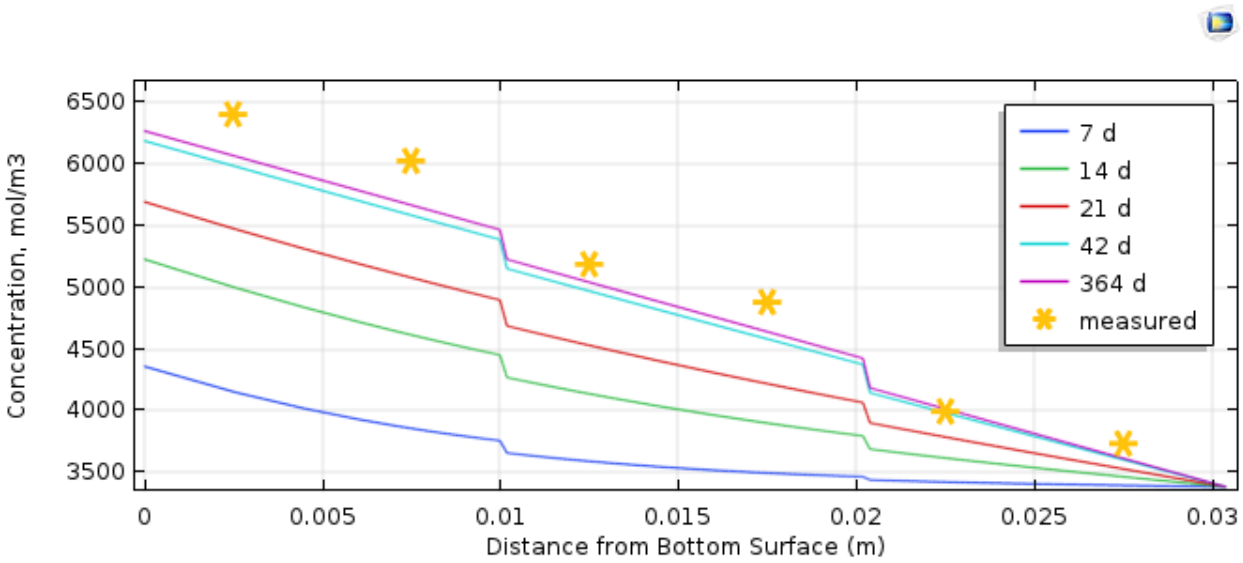

Figure 2.21. COMSOL simulation results for PU-glued laminates using D_1 = 2×10^{-7} cm^2/s.

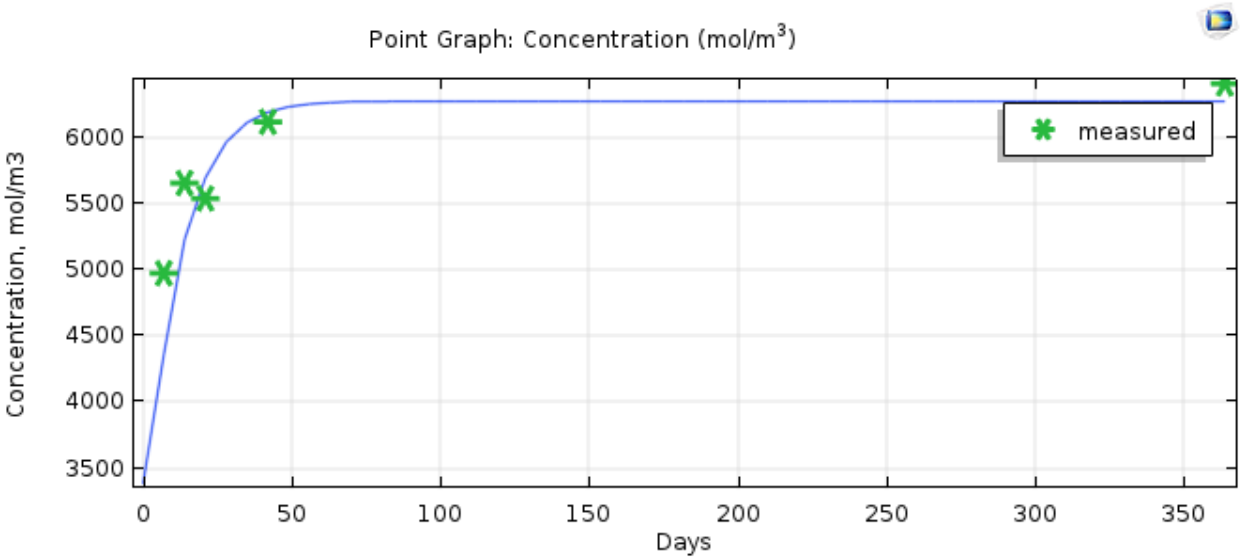

Figure 2.22. COMSOL simulation results for PU-glued laminates using $D_1 = 2\times10^{-7}$ cm^2/s.

Similarly, simulation results for PU-glued laminates using D_2 are shown in Figure 2.23 and 2.24. Since the glueline diffusion coefficient is much smaller, the water barrier function became stronger, therefore a bigger step change of water concentration (or moisture content) was found along the glueline. As a result, the steady state water concentration of the bottom layer were higher than the experiment data. This suggested that the glueline diffusion coefficient should be bigger than D_2. Simulations results for laminates glued with the other two adhesive were similar and hence are not presented here.

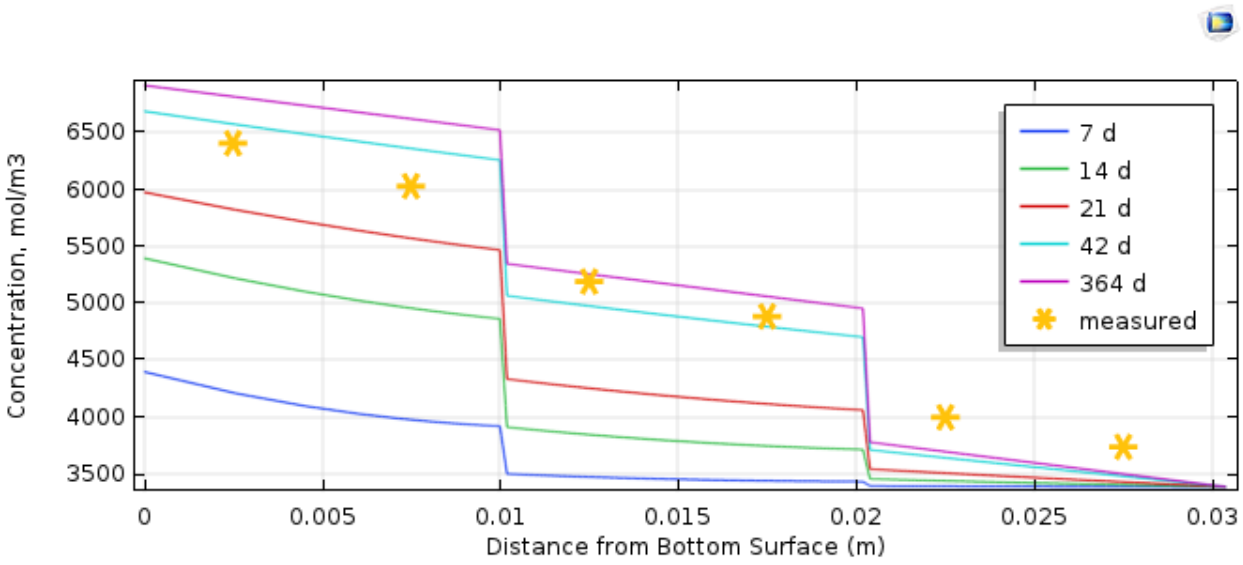

Figure 2.23. COMSOL simulation results for PU-glued laminates using $D_2 = 2\times10^{-8}$ cm^2/s.

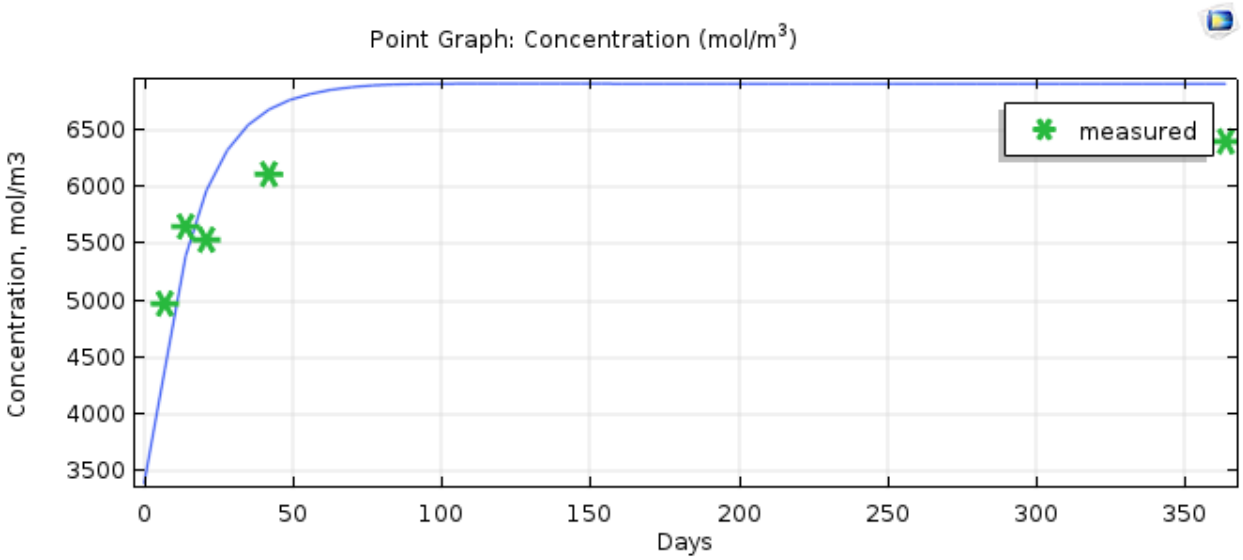

Figure 2.24. COMSOL simulation results for PU-glued laminates using $D_2 = 2\times10^{-8}$ cm^2/s.

4.4.2. Linear Glueline Diffusion Coefficient

From the constant glueline diffusion coefficient simulation results, a linear dependency of glueline diffusion coefficient on water concentration was applied:

$$D = Ac + B$$

where D is the glueline diffusion coefficient; c is the concentration; A, B are constants.

After fitting the experiment data, this dependency was found to be:

$$D = (1 - \frac{c}{10000}) \times 10^{-7} cm^2/s$$

COMSOL simulation results for PU-glued laminates are presented in Figure . Both the simulated results and experimental data showed that after 60 days, the diffusion process was close to steady state, which was the same in the solid southern pine diffusion process. Figure 2.25 also revealed that a good match between the simulation and experiment can be found at steady state.

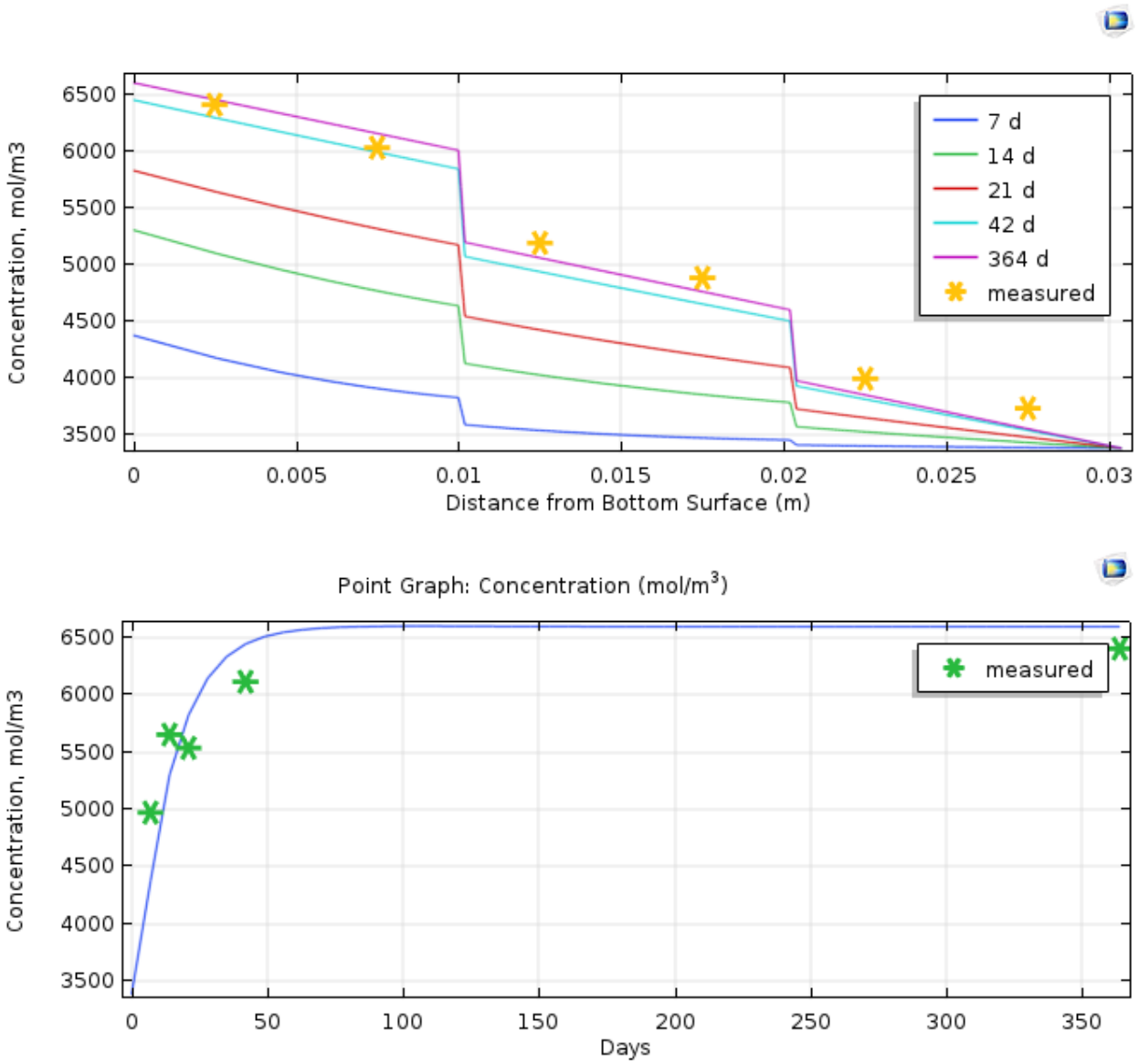

Figure 2.25. COMSOL simulation results for PU-glued laminates when the moisture dependency of the glueline diffusion coefficient is considered.

Similar findings were obtained in PRF-glued (Figure) and MF-glued (Figure) laminates, except that in the PRF-glued panels, the measured moisture contents of the middle layer were about 1% larger than those of the simulated results.

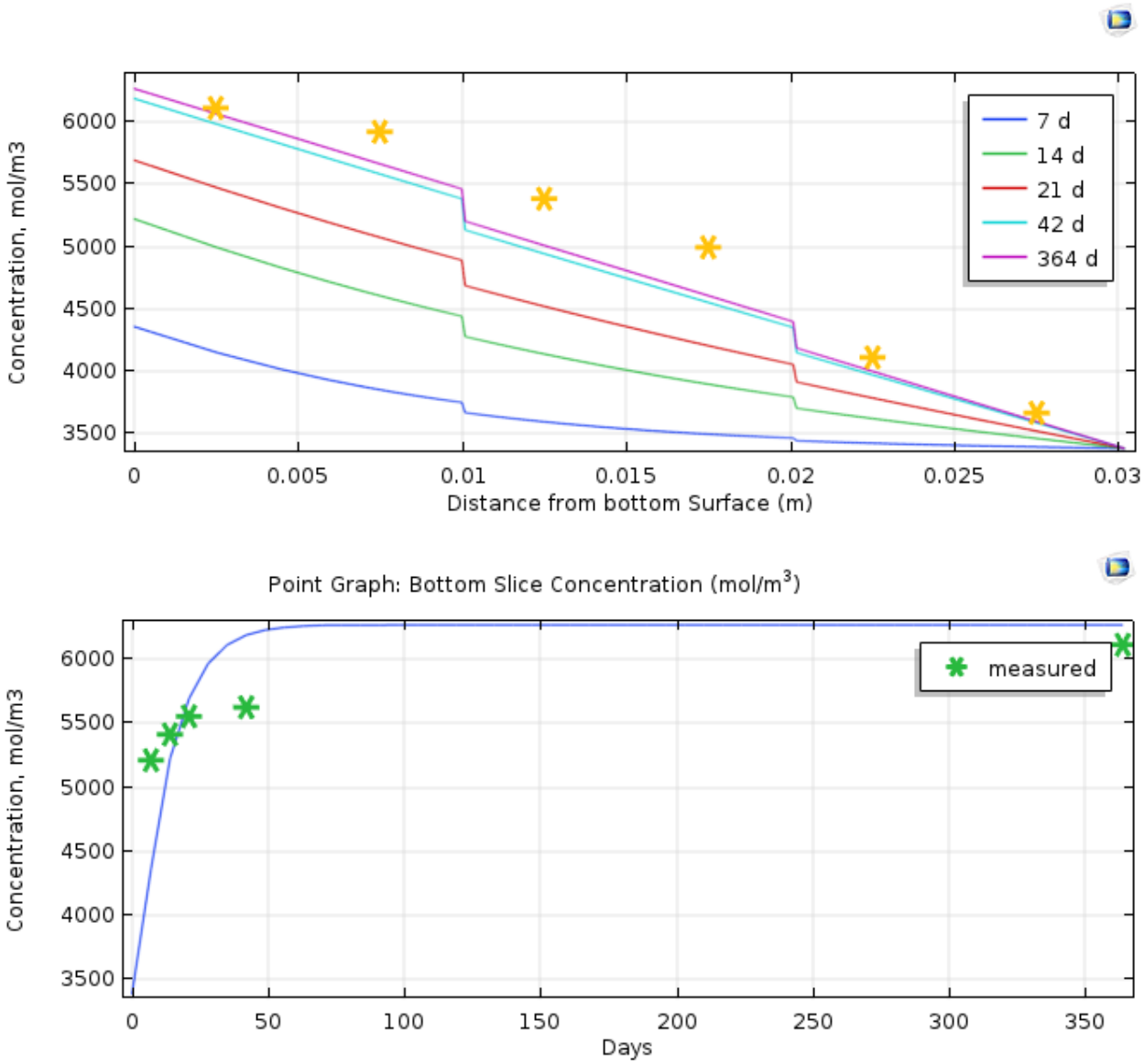

Figure 2.26. COMSOL simulation results for PRF-glued laminates when the moisture dependency of the glueline diffusion coefficient is considered.

MF glued CLT simulation results can be seen in Figure 2.27.

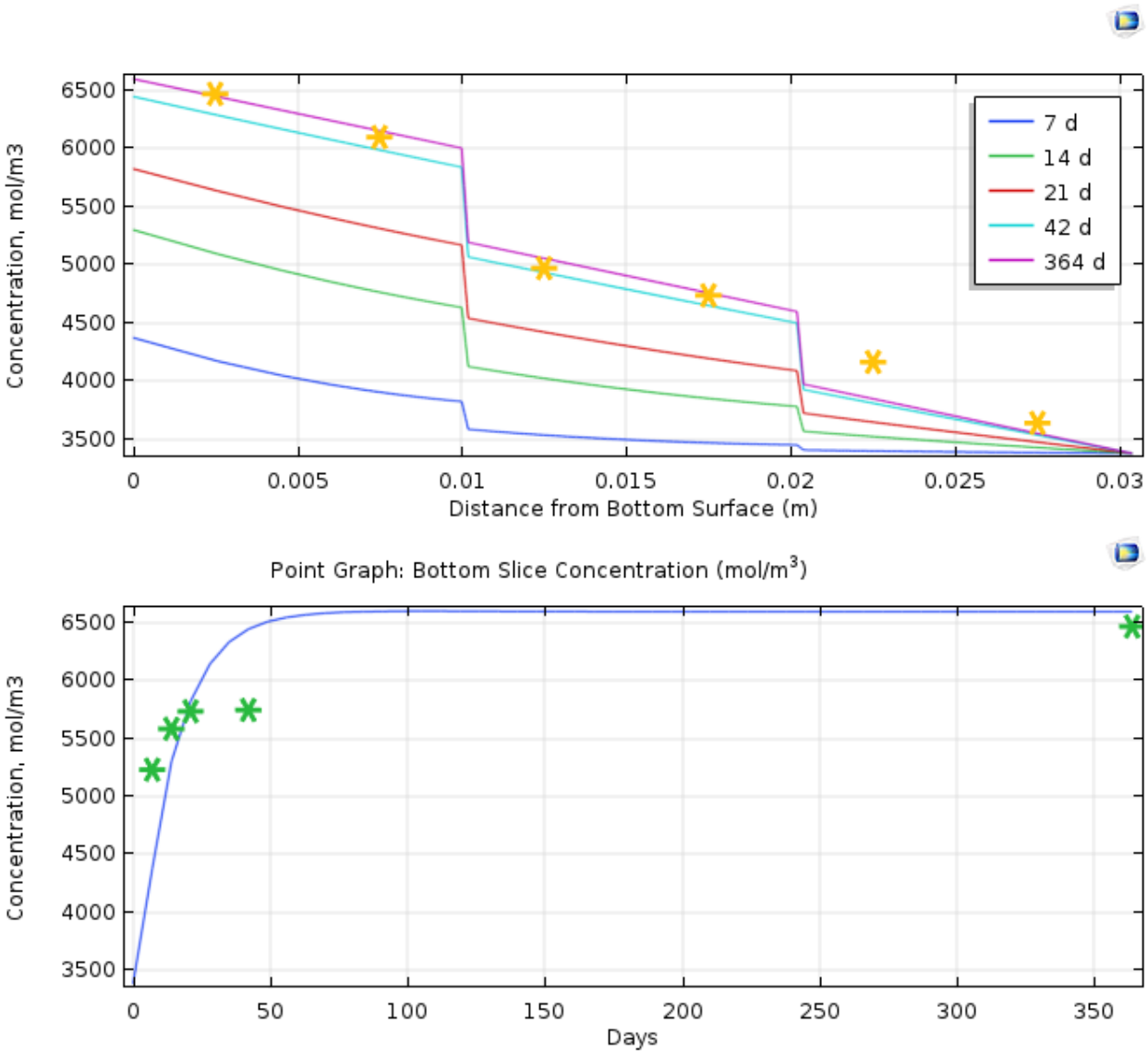

Figure 2.27. COMSOL simulation results for MF-glued laminates when the moisture dependency of the glueline diffusion coefficient is considered.

4.5. Hygrothermal Performance of Southern Pine CLT

WUFI Pro was used to study the hygrothermal performance of southern pine CLT in a building envelope. A virtual wall structure using CLT was constructed based on recommendations from the CLT Handbook US Edition as shown in Figure 2.28. Details regarding the thickness and physical properties of these wall elements are presented in Table 2.7.

Cold year in Wilmington, North Carolina was selected from WUFI Pro's built-in database as the exterior climate. In order to test hygrothermal performance at the most severe case, orientation was chosen as North (from Climate Analysis result), rain exposure factor and rain deposition factor were set to be 1.4 and 1 respectively. The indoor climate chosen was based on ASHRAE 160: air-conditioning, 2.8 ^{0}C floating indoor temperature shift, set points for heating and cooling were 21.1 ^{0}C and 23.9 ^{0}C respectively; two bedrooms and standard construction. Heat resistance values on the exterior and interior surfaces were set to 0.0588 and 0.125 m^{2}K/W respectively.

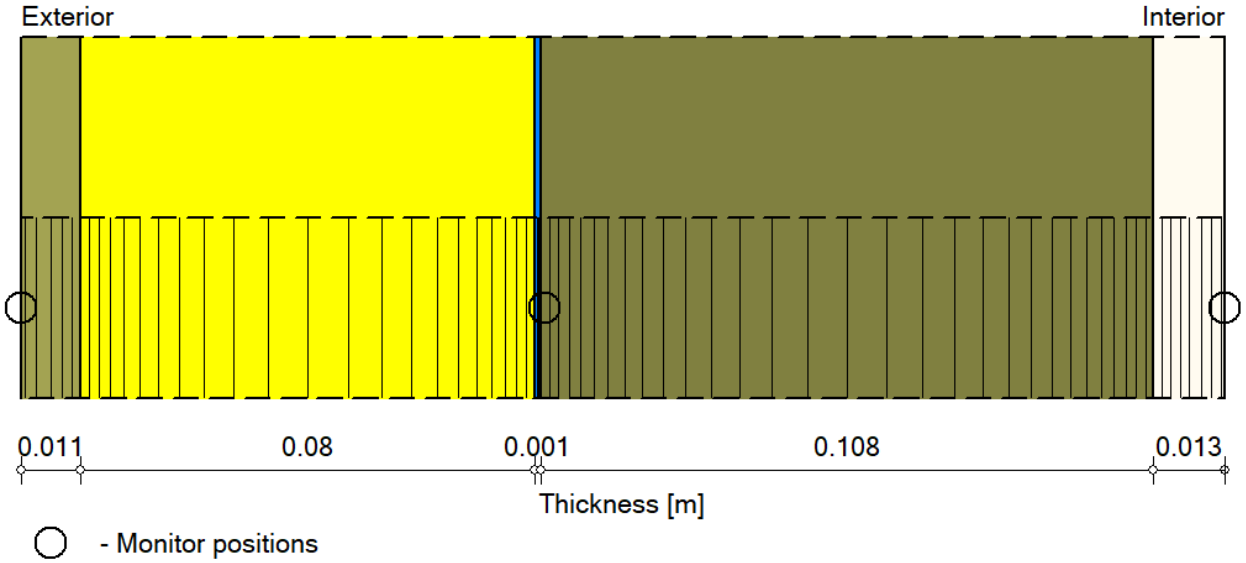

Figure 2.28. Wall assembly with a total thickness of 0.21m for the case study. From left to right: mineral wool, weather resistive barrier, 3-ply CLT and gypsum board.

Table 2.7. Size and physical properties of the wall assembly elements.

layer	thickness (mm)	thermal conductivity (W/mK)	heat capacity (J/kgK)	diffusion resistance factor
composite wood siding	11	0.094	1880	53.1
mineral wool	80	0.04	850	1.3
weather resistive barrier	1	2.3	2300	100
3-ply CLT	108	0.12	2500	203
gypsum board	13	0.2	850	8.3

The simulation was run for 3 years with an interval of 1 hour. The initial conditions of all wall elements were set to be in equilibrium at 65% relative humidity, 20 ^{0}C. Simulation result of total water content is shown in Figure 2.29. Although there were moisture content fluctuations during the simulation period, moisture accumulation did not occur.

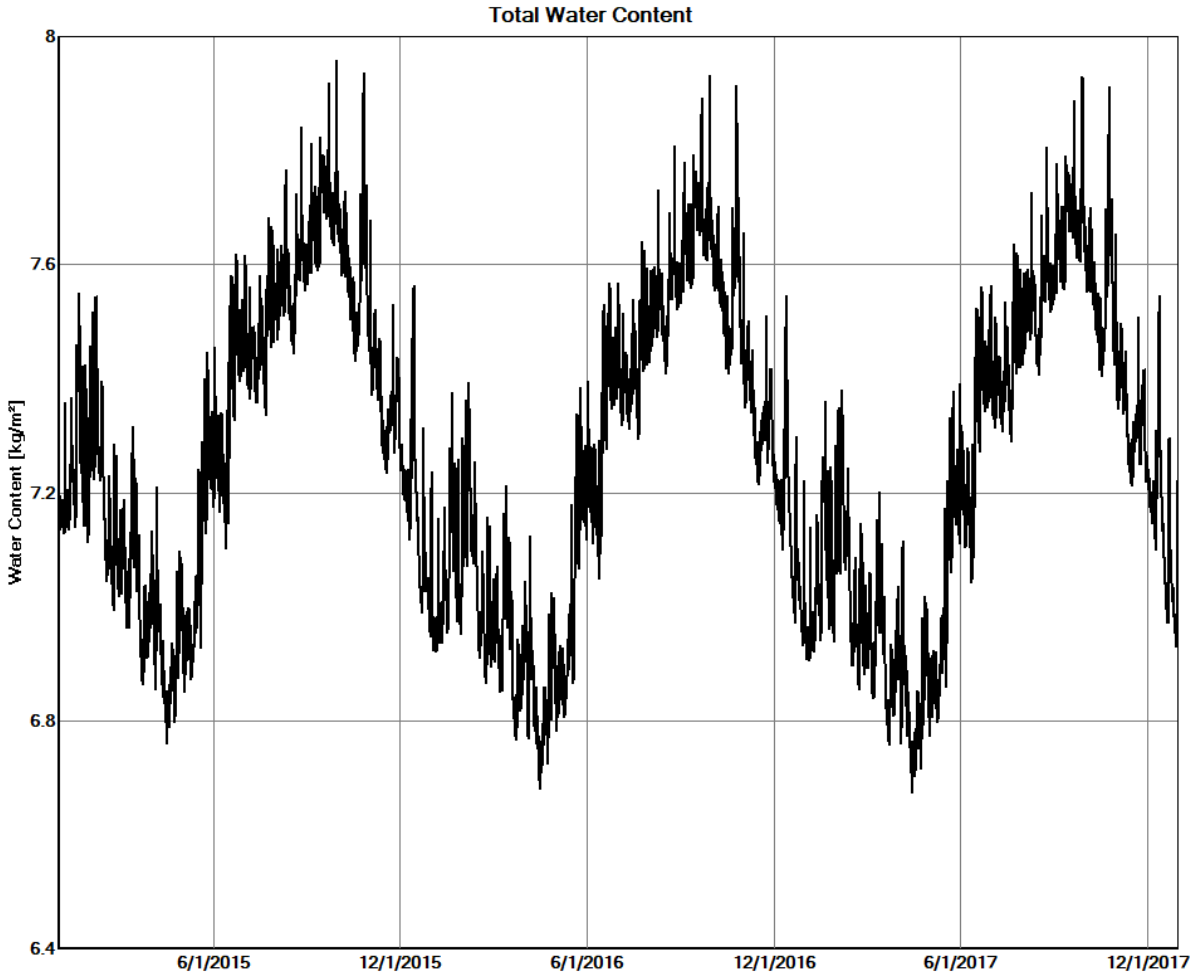

Figure 2.29. Total water content during the 3-year simulation period.

In order to evaluate the most vulnerable positions for moisture accumulation, a close examination of water content in the 3-ply CLT was performed. As shown in Figure 2.30, the maximum average moisture content was about 13.7%, while the minimum was around 12.5%.

Same with the total moisture content curve, it can be seen that there was no moisture accumulation in the 3-ply CLT.

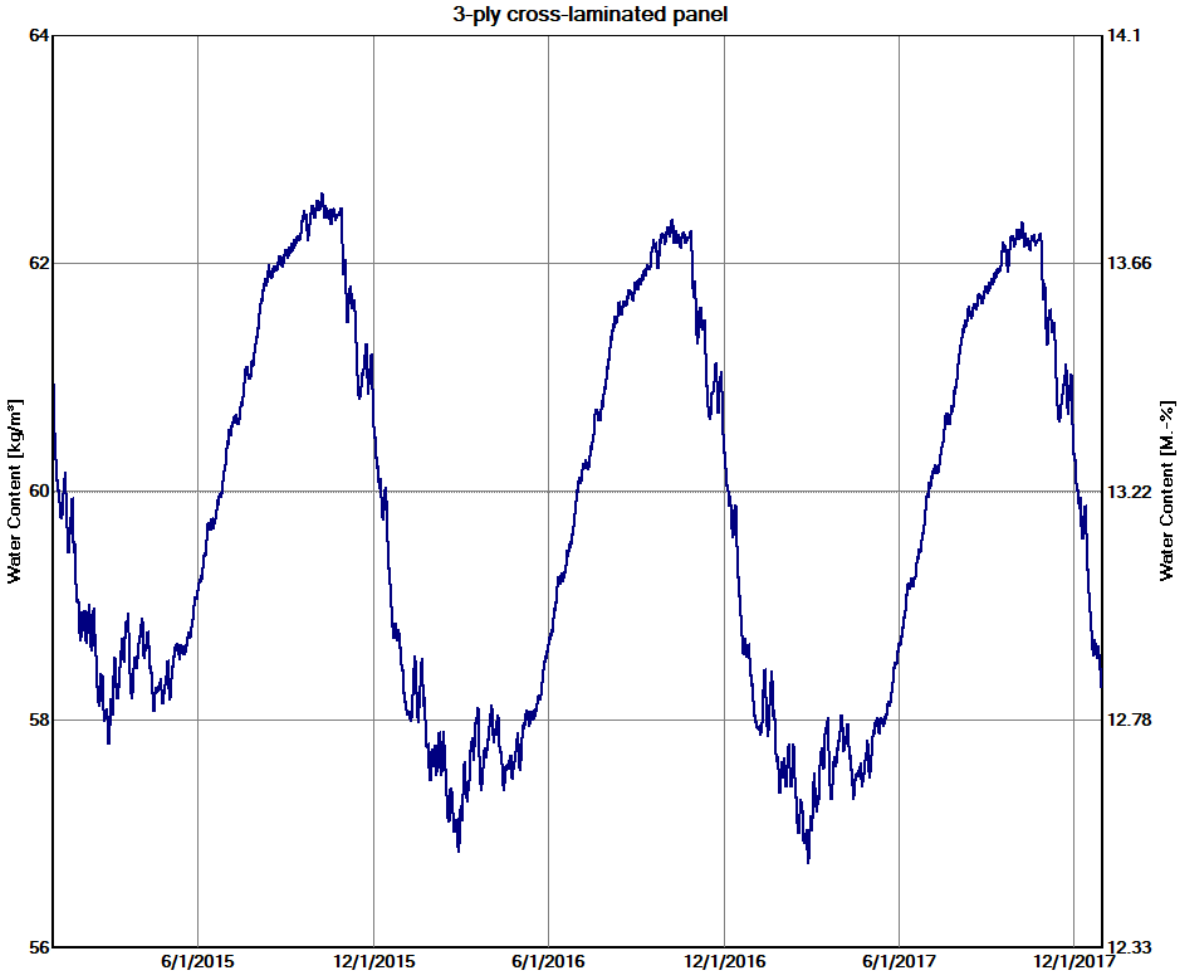

Figure 2.30. Water content in 3-ply cross-laminated timber during a 3-year simulation period.

To further evaluate the possibility of mold growth, the temperature and relative humidity profiles (

Figure 2.31), together with the isopleth (Figure), at the left side of the 3-ply CLT were examined. Once again, there was no apparent moisture accumulation at this monitor position. The most extreme conditions were at around 80% relative humidity and 26 ^{0}C, which gave an equivalent moisture content of around 17%. This moisture content is below the 20% moisture

content threshold for fungal growth. The isopleths in Figure 2.32 also confirmed that even at most severe scenario, the occurrences of favorable mold growth condition were still very rare

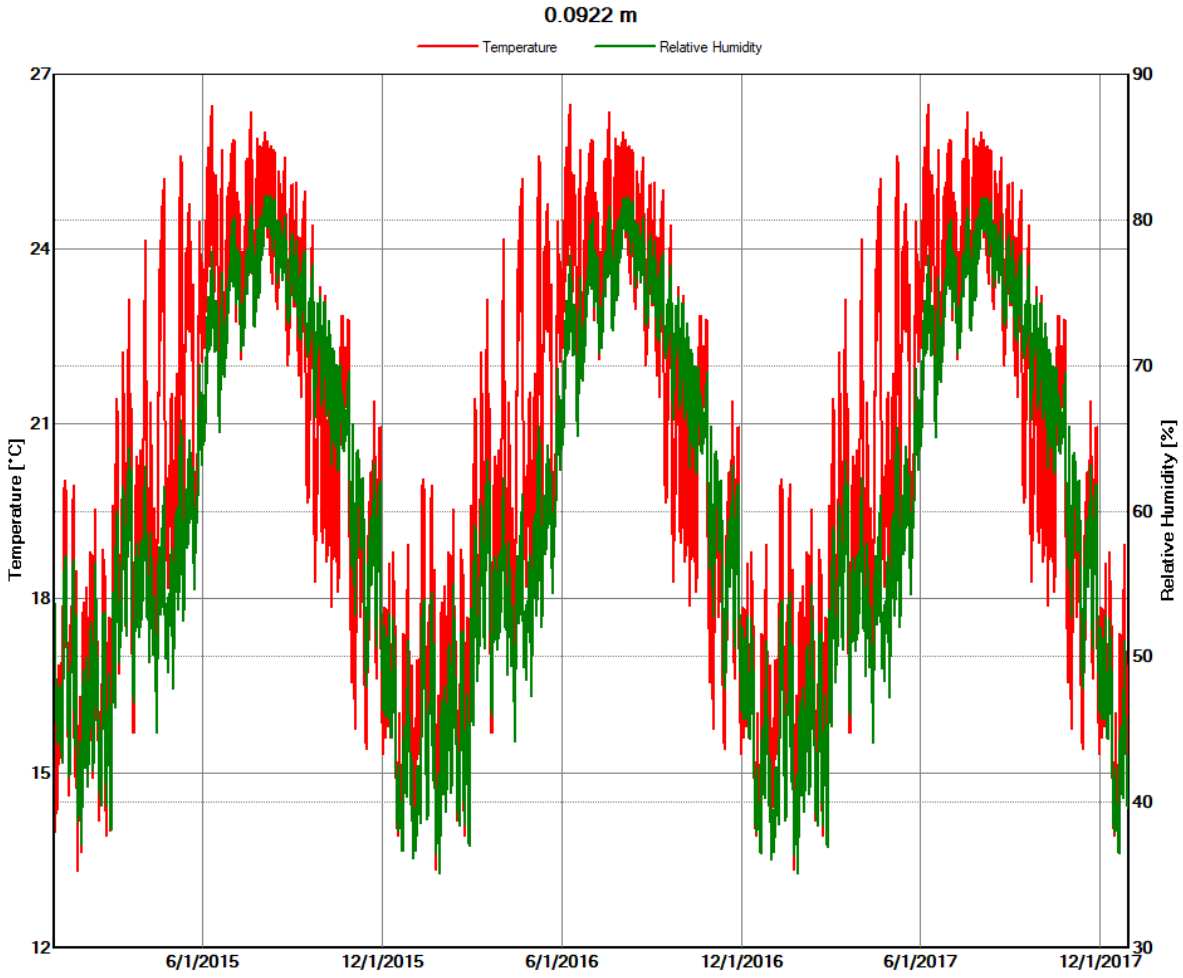

during the whole simulation period.

Figure 2.31. Temperature and relative humidity profiles at the left side monitor position of a 3-ply CLT during a 3-year simulation period.

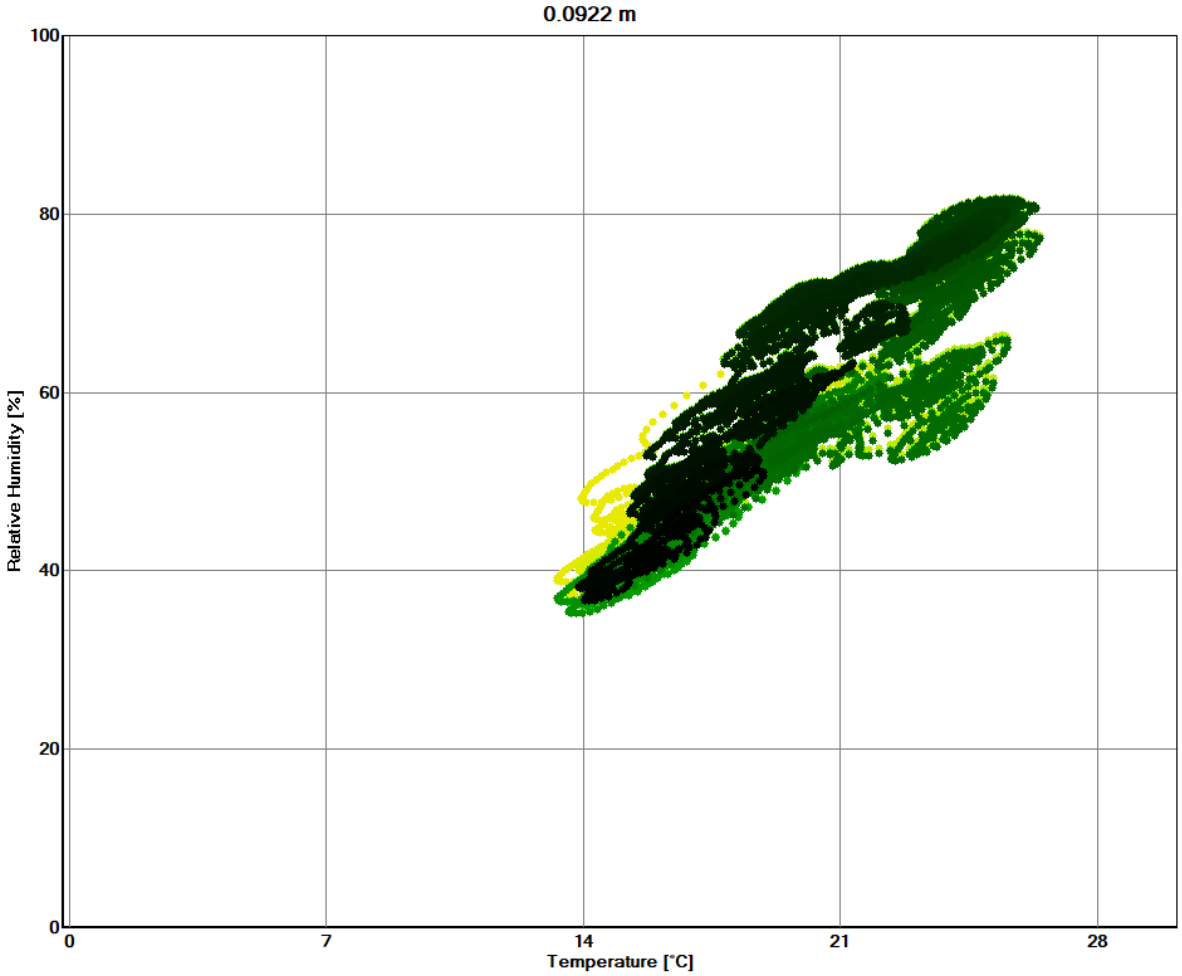

Figure 2.32. Isopleth at the left side monitor position of a 3-ply CLT during a 3-year simulation period.

5. Conclusions

In order to study the moisture transport in southern pine cross-laminated timber, sorption isotherm measurements were performed first to obtain the relationship between relative humidity and moisture content. Then unsteady-state diffusion (desorption) measurements were conducted to find the moisture diffusion coefficient of solid southern pine. Thereafter, steady-state diffusion experiments were performed on solid southern pine. The steady-state diffusion results, when coupled with COMSOL simulation, verified the linear moisture content distribution along the thickness direction and hence the constant moisture diffusion coefficient. Then, the moisture diffusion properties of laminates were evaluated by the steady-state diffusion cup method to obtain the diffusion coefficient of the glueline. Lastly, the hygrothermal performance of a typical CLT building envelope was evaluated through WUFI simulations.

From the results of the study, it could be concluded that:

1. The equilibrium moisture content of southern pine at a given relative humidity at 20°C can be calculated using the Hailwood-Horrobin sorption model.
2. An average diffusion coefficient value of 3.0×10^{-6} cm^2/s may be used to describe the transport of water in solid southern pine below the fiber saturation point.
3. The glueline moisture diffusion coefficient is independent of adhesive type, but depends on glueline thickness and moisture content.
4. A well-constructed CLT wall assembly does not provide favorable conditions for mold growth.

CHAPTER 3. MOISTURE INDUCED WARPING AND STRESSES IN SOUTHERN PINE CROSS-LAMINATED TIMBER

When wood and wood products (including CLT) lose or absorb water, they will shrink or swell accordingly. The big difference between shrinkage or swelling in different directions is the primary reason for warping in cross section when lumber is subjected to moisture changes in use. This raises concerns of dimensional stability, especially when CLT is used as a load bearing element. Therefore, warping studies of southern pine CLT were presented in this chapter.

1. Literature Review

1.1. Shrinkage and Swelling of Wood

Wood is composed of hollow fibers or cells, most of which lie nearly along the tree trunk direction (longitudinal direction). The two coordinate systems, geometric (denoted as x, y and z or in other similar terms) and principal material axes (denoted as L, T and R or 1, 2 and 3), commonly used in wood analysis are shown in Figure 3.1. Being a hygroscopic material, wood absorbs or loses moisture when the relative humidity of the surrounding air changes. With time, the moisture in wood will come into equilibrium with the surrounding air, and this moisture content is referred as equilibrium moisture content (EMC) (Skaar, 1984).

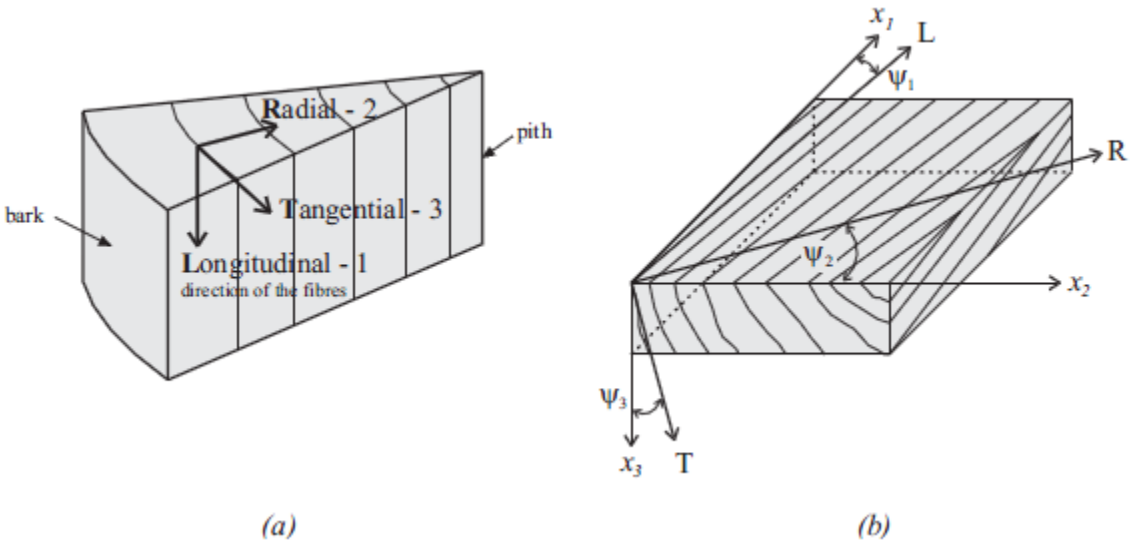

Figure 3.1. (a) The orthotropic directions in wood; (b) geometric (x_1, x_2, x_3) and orthotropic (L, R, T) axes of a wood block with angles required to relate the two coordinate systems.

In general, wood does not shrink until the moisture content drops below fiber saturation point (FSP), where FSP is defined as the moisture content at which the cell wall is saturated with bound water but no liquid water exists inside cell cavities (Stamm, 1935). Below FSP, when wood loses (or gains) moisture, bound water is removed from (or absorbed in) the cell wall and that results in the decrease (or increase) of cell wall thickness. The degree of shrinkage or swelling is often expressed as the percentage of dimensional change. The percent shrinkage (%s) is given as:

$$\%s = \frac{change\ in\ dimension}{initial\ dimension} \times 100 = \frac{D_{MC_2} - D_{MC_1}}{D_{MC_2}} \times 100 \qquad (1)$$

where D_{MC_1} is the dimension (length or volume) at moisture content MC_1, and D_{MC_2} is the dimension at moisture content MC_2, with MC_2 being greater than MC_1.

Similarly, the percent swelling (%S) is given as:

$$\%S = \frac{change\ in\ dimension}{initial\ dimension} \times 100 = \frac{D_{MC_2} - D_{MC_1}}{D_{MC_1}} \times 100 \quad (2)$$

Most often the maximum percent shrinkage values (that is from green to ovendry condition) are listed in Wood Handbook and other books. Assuming a linear relationship between wood dimension and moisture content (below FSP), the percent shrinkage, $\%s_{M2-M1}$, from moisture content MC_2 to MC_1 can be determined as:

$$\%s_{M2-M1} = \frac{\%s_{g-o}(MC_2 - MC_1)}{30 - 0.01 \times (\%s_{g-o})(30 - MC_2)} \quad (3)$$

where $\%s_{g-o}$ is the maximum percent shrinkage from green to ovendry condition.

For most calculations, Equation (3) can be simplified as:

$$\%s_{M2-M1} = \frac{\%s_{g-o}(MC_2 - MC_1)}{30} \quad (4)$$

Mainly due to the alignment of fibers or cells, hygroexpansion is usually much greater transversely (tangentially or radially) than longitudinally. The tangential and radial shrinkage coefficients are also considerably different from each other, with the mean tangential/radial shrinkage (T/R) ratio of about two. The high T/R ratio is the primary reason for warping in cross section when lumber is first dried or subjected to moisture loss in use (Skaar, 1984). Figure 3.2 illustrates some of the common warping when wood is dried from green condition.

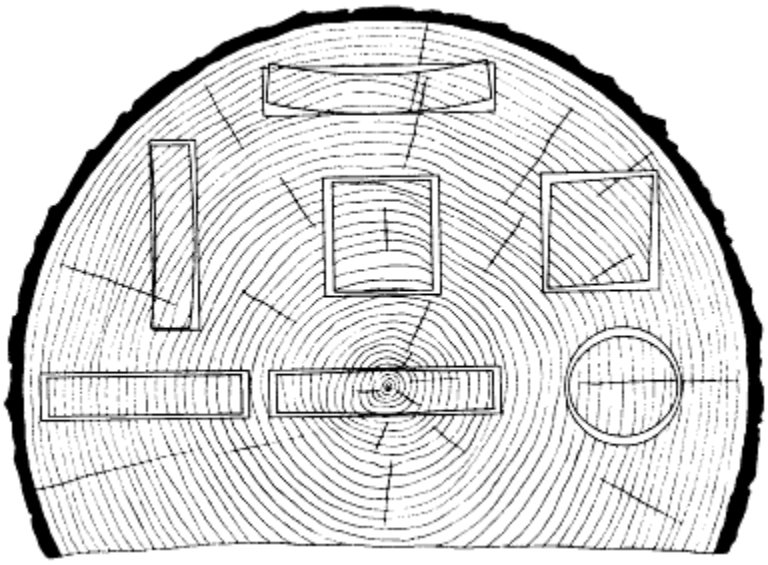

Figure 3.2. Cross-sectional distortions in wood after drying. (Courtesy of USDA, Forest Products Laboratory)

1.2. Modeling of Strain, Stress and Deformation

1.2.1. Stress and Strain

The state of stress at a point can be expressed by nine stress components acting on the sides of an elemental cube with the sides parallel to the axes of the reference coordinate system, as depicted in Figure 3.3 (Daniel et al., 1994):

$$\begin{bmatrix}\sigma_{11}\\ \sigma_{22}\\ \sigma_{33}\\ \sigma_{23}\\ \sigma_{31}\\ \sigma_{12}\\ \sigma_{32}\\ \sigma_{13}\\ \sigma_{21}\end{bmatrix} = \begin{bmatrix} C_{1111} & C_{1122} & C_{1133} & C_{1123} & C_{1131} & C_{1112} & C_{1132} & C_{1113} & C_{1121}\\ C_{2211} & C_{2222} & C_{2233} & C_{2223} & C_{2231} & C_{2212} & C_{2232} & C_{2213} & C_{2221}\\ C_{3311} & C_{3322} & C_{3333} & C_{3323} & C_{3331} & C_{3312} & C_{3332} & C_{3313} & C_{3321}\\ C_{2311} & C_{2322} & C_{2333} & C_{2323} & C_{2331} & C_{2312} & C_{2332} & C_{2313} & C_{2321}\\ C_{3111} & C_{3122} & C_{3133} & C_{3123} & C_{3131} & C_{3112} & C_{3132} & C_{3113} & C_{3121}\\ C_{1211} & C_{1222} & C_{1233} & C_{1223} & C_{1231} & C_{1212} & C_{1232} & C_{1213} & C_{1221}\\ C_{3211} & C_{3222} & C_{3233} & C_{3223} & C_{3231} & C_{3212} & C_{3232} & C_{3213} & C_{3221}\\ C_{1311} & C_{1322} & C_{1333} & C_{1323} & C_{1331} & C_{1312} & C_{1332} & C_{1313} & C_{1321}\\ C_{2111} & C_{2122} & C_{2133} & C_{2123} & C_{2131} & C_{2112} & C_{2132} & C_{2113} & C_{2121}\end{bmatrix}\begin{bmatrix}\varepsilon_{11}\\ \varepsilon_{22}\\ \varepsilon_{33}\\ \varepsilon_{23}\\ \varepsilon_{31}\\ \varepsilon_{12}\\ \varepsilon_{32}\\ \varepsilon_{13}\\ \varepsilon_{21}\end{bmatrix} \quad (5)$$

where $[\sigma_{ij}]$ is the stress matrix; $[\varepsilon_{ij}]$ is the strain matrix; $[C_{ijkl}]$ is the stiffness matrix.

Similarly, the state of deformation can also be expressed by:

$$\begin{bmatrix}\varepsilon_{11}\\ \varepsilon_{22}\\ \varepsilon_{33}\\ \varepsilon_{23}\\ \varepsilon_{31}\\ \varepsilon_{12}\\ \varepsilon_{32}\\ \varepsilon_{13}\\ \varepsilon_{21}\end{bmatrix} = \begin{bmatrix} S_{1111} & S_{1122} & S_{1133} & S_{1123} & S_{1131} & S_{1112} & S_{1132} & S_{1113} & S_{1121}\\ S_{2211} & S_{2222} & S_{2233} & S_{2223} & S_{2231} & S_{2212} & S_{2232} & S_{2213} & S_{2221}\\ S_{3311} & S_{3322} & S_{3333} & S_{3323} & S_{3331} & S_{3312} & S_{3332} & S_{3313} & S_{3321}\\ S_{2311} & S_{2322} & S_{2333} & S_{2323} & S_{2331} & S_{2312} & S_{2332} & S_{2313} & S_{2321}\\ S_{3111} & S_{3122} & S_{3133} & S_{3123} & S_{3131} & S_{3112} & S_{3132} & S_{3113} & S_{3121}\\ S_{1211} & S_{1222} & S_{1233} & S_{1223} & S_{1231} & S_{1212} & S_{1232} & S_{1213} & S_{1221}\\ S_{3211} & S_{3222} & S_{3233} & S_{3223} & S_{3231} & S_{3212} & S_{3232} & S_{3213} & S_{3221}\\ S_{1311} & S_{1322} & S_{1333} & S_{1323} & S_{1331} & S_{1312} & S_{1332} & S_{1313} & S_{1321}\\ S_{2111} & S_{2122} & S_{2133} & S_{2123} & S_{2131} & S_{2112} & S_{2132} & S_{2113} & S_{2121}\end{bmatrix}\begin{bmatrix}\sigma_{11}\\ \sigma_{22}\\ \sigma_{33}\\ \sigma_{23}\\ \sigma_{31}\\ \sigma_{12}\\ \sigma_{32}\\ \sigma_{13}\\ \sigma_{21}\end{bmatrix} \quad (6)$$

The compliance matrix $[S_{ijkl}]$ is the inverse of the stiffness matrix $[C_{ijkl}]$.

In general, it requires 81 elastic components to fully describe a material. However, by considering the symmetry of stress and strain tensors, the number of independent elastic constants can be reduced to 36. This number can be further reduced to 21 by the energy relations. In the case of orthotropic materials, only 9 independent elastic constants are needed to represent the state of stress or deformation at a point:

$$\begin{bmatrix}\sigma_1\\ \sigma_2\\ \sigma_3\\ \tau_4=\tau_{23}\\ \tau_5=\tau_{31}\\ \tau_6=\tau_{12}\end{bmatrix} = \begin{bmatrix} C_{11} & C_{12} & C_{13} & 0 & 0 & 0\\ C_{21} & C_{22} & C_{23} & 0 & 0 & 0\\ C_{31} & C_{32} & C_{33} & 0 & 0 & 0\\ 0 & 0 & 0 & C_{44} & 0 & 0\\ 0 & 0 & 0 & 0 & C_{55} & 0\\ 0 & 0 & 0 & 0 & 0 & C_{66}\end{bmatrix}\begin{bmatrix}\varepsilon_1\\ \varepsilon_2\\ \varepsilon_3\\ \gamma_4\\ \gamma_5\\ \gamma_6\end{bmatrix} \quad (7)$$

And:

$$\begin{bmatrix}\varepsilon_1\\ \varepsilon_2\\ \varepsilon_3\\ \gamma_4=\gamma_{23}\\ \gamma_5=\gamma_{31}\\ \gamma_6=\gamma_{12}\end{bmatrix} = \begin{bmatrix} S_{11} & S_{12} & S_{13} & 0 & 0 & 0\\ S_{21} & S_{22} & S_{23} & 0 & 0 & 0\\ S_{31} & S_{32} & S_{33} & 0 & 0 & 0\\ 0 & 0 & 0 & S_{44} & 0 & 0\\ 0 & 0 & 0 & 0 & S_{55} & 0\\ 0 & 0 & 0 & 0 & 0 & S_{66}\end{bmatrix}\begin{bmatrix}\sigma_1\\ \sigma_2\\ \sigma_3\\ \tau_4\\ \tau_5\\ \tau_6\end{bmatrix} \quad (8)$$

Table 3.8. Independent elastic component numbers of various types of materials.

Material	No. of independent elastic components
general anisotropic material	81
anisotropic material considering symmetry of stress and strain tensors	36
anisotropic material with elastic energy considerations	21
general orthotropic material	9
orthotropic material with transverse isotropy	5
isotropic material	2

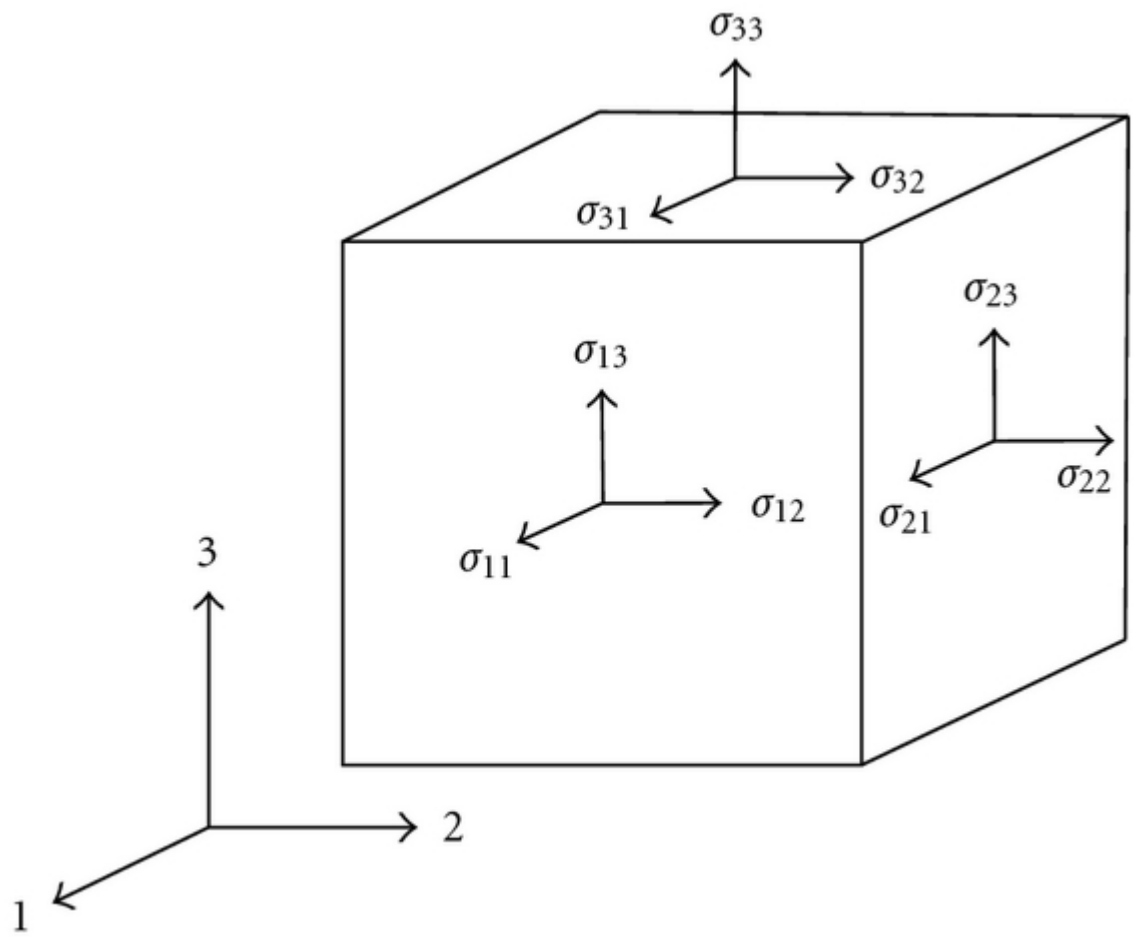

Figure 3. State of stress at a point in a general continuum.

To have more physical meaning, the above equations can be transformed by using engineering constants (moduli and Poisson's ratios):

$$\begin{bmatrix}\varepsilon_1\\ \varepsilon_2\\ \varepsilon_3\\ \gamma_4\\ \gamma_5\\ \gamma_6\end{bmatrix}=\begin{bmatrix} \frac{1}{E_1} & -\frac{\nu_{21}}{E_2} & -\frac{\nu_{31}}{E_3} & 0 & 0 & 0\\ -\frac{\nu_{12}}{E_1} & \frac{1}{E_2} & -\frac{\nu_{32}}{E_3} & 0 & 0 & 0\\ -\frac{\nu_{13}}{E_1} & -\frac{\nu_{23}}{E_2} & \frac{1}{E_3} & 0 & 0 & 0\\ 0 & 0 & 0 & \frac{1}{G_{23}} & 0 & 0\\ 0 & 0 & 0 & 0 & \frac{1}{G_{13}} & 0\\ 0 & 0 & 0 & 0 & 0 & \frac{1}{G_{12}} \end{bmatrix}\begin{bmatrix}\sigma_1\\ \sigma_2\\ \sigma_3\\ \tau_4\\ \tau_5\\ \tau_6\end{bmatrix} \tag{9}$$

where E_i are Young's moduli; ν_{ij} is Poisson's ratio; G_{ij} is shear modulus.

Normally the orthotropic axes do not coincide with the geometric axes (as shown is Figure 3.4), thus transformation between the two coordinate systems is needed. A two dimensional transformation is given here:

$$\begin{bmatrix}\sigma_1\\ \sigma_2\\ \tau_6\end{bmatrix}=[T]\begin{bmatrix}\sigma_x\\ \sigma_y\\ \tau_s\end{bmatrix} \tag{10}$$

$$[T]=\begin{bmatrix} \cos\theta^2 & \sin\theta^2 & 2\cos\theta\sin\theta\\ \sin\theta^2 & \cos\theta^2 & -2\cos\theta\sin\theta\\ -\cos\theta\sin\theta & \cos\theta\sin\theta & \cos\theta^2-\sin\theta^2 \end{bmatrix} \tag{11}$$

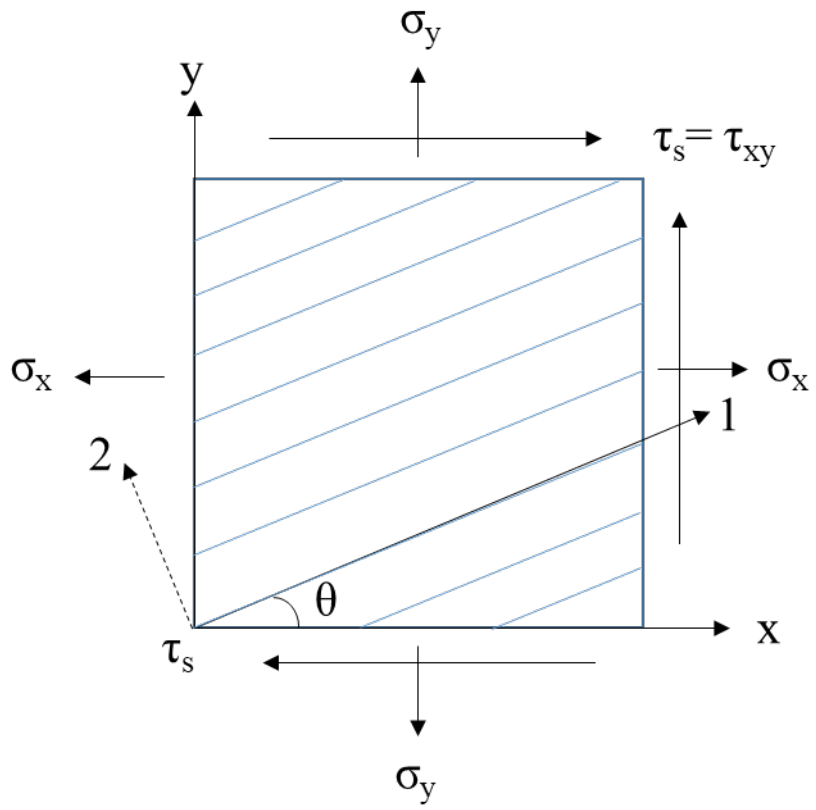

Figure 3.4. Transformation between geometric and orthotropic coordinate systems (two dimensional).

1.2.2. Strain-deformation Relations

Given the basics of stress and strain relations, it is more helpful to introduce the strain-deformation relations when dealing with a laminate. The x-y plane equidistant from the top and bottom surfaces of the laminates is called midplane or reference plane. The midplane displacements u_0 in x-direction and v_0 in y-direction, and out-of-plane displacement w are functions of x and y only:

$$u_0 = u_0(x, y)$$
$$v_0 = v_0(x, y) \quad (12)$$

$$w = f(x, y)$$

The rotation of x and y axis are:

$$\alpha_x = \frac{\partial w}{\partial x}$$

$$\alpha_y = \frac{\partial w}{\partial y} \tag{13}$$

The in-plane displacement of a point are:

$$u = u_0 - z\frac{\partial w}{\partial x}$$

$$v = v_0 - z\frac{\partial w}{\partial y} \tag{14}$$

where z is the through-the-thickness coordinate.

The strain-displacement relations of elasticity for small displacements is:

$$\varepsilon_x = \frac{\partial u}{\partial x} = \frac{\partial u_0}{\partial x} - z\frac{\partial^2 w}{\partial x^2}$$

$$\varepsilon_y = \frac{\partial v}{\partial y} = \frac{\partial v_0}{\partial y} - z\frac{\partial^2 w}{\partial y^2} \tag{15}$$

$$\gamma_{xy} = \gamma_s = \frac{\partial u}{\partial y} + \frac{\partial v}{\partial x} = \frac{\partial u_0}{\partial y} + \frac{\partial v_0}{\partial x} - 2z\frac{\partial^2 w}{\partial x \partial y}$$

The curvatures of the laminate are:

$$\kappa_x = -\frac{\partial^2 w}{\partial x^2} \tag{16}$$

$$\kappa_y = -\frac{\partial^2 w}{\partial y^2}$$

$$\kappa_{xy} = \kappa_s = -2\frac{\partial^2 w}{\partial x \partial y}$$

Then we can determine the strains at any point by the reference plane strains and the curvatures:

$$\begin{bmatrix}\varepsilon_x \\ \varepsilon_y \\ \gamma_s\end{bmatrix} = \begin{bmatrix}\varepsilon_x^0 \\ \varepsilon_y^0 \\ \gamma^0\end{bmatrix} + z\begin{bmatrix}\kappa_x^0 \\ \kappa_y^0 \\ \kappa_s^0\end{bmatrix} \tag{17}$$

For the kth layer of a multidirectional laminate whose midplane is at a distance $\bar{z}_k$ from the laminate reference plane, the stress-strain relations referred to the material axes are:

$$\begin{bmatrix}\sigma_1 \\ \sigma_2 \\ \tau_6\end{bmatrix}_k = \begin{bmatrix}Q_{11} & Q_{12} & 0 \\ Q_{21} & Q_{22} & 0 \\ 0 & 0 & Q_{66}\end{bmatrix}\begin{bmatrix}\varepsilon_1 \\ \varepsilon_2 \\ \gamma_6\end{bmatrix}_k \tag{18}$$

where $Q_{ij} = C_{ij} - \frac{C_{i3}C_{j3}}{C_{33}}$ $(i,j = 1,2,6)$.

It can also be transferred to the laminate coordinate system as:

$$\begin{aligned}\begin{bmatrix}\sigma_x \\ \sigma_y \\ \tau_s\end{bmatrix}_k &= \begin{bmatrix}Q_{xx} & Q_{xy} & Q_{xs} \\ Q_{yx} & Q_{yy} & Q_{ys} \\ Q_{sx} & Q_{sy} & Q_{ss}\end{bmatrix}\begin{bmatrix}\varepsilon_x \\ \varepsilon_y \\ \gamma_s\end{bmatrix}_k \\ &= \begin{bmatrix}Q_{xx} & Q_{xy} & Q_{xs} \\ Q_{yx} & Q_{yy} & Q_{ys} \\ Q_{sx} & Q_{sy} & Q_{ss}\end{bmatrix}\begin{bmatrix}\varepsilon_x^0 \\ \varepsilon_y^0 \\ \gamma_s^0\end{bmatrix} + \mathrm{z}\begin{bmatrix}Q_{xx} & Q_{xy} & Q_{xs} \\ Q_{yx} & Q_{yy} & Q_{ys} \\ Q_{sx} & Q_{sy} & Q_{ss}\end{bmatrix}\begin{bmatrix}\kappa_x^0 \\ \kappa_y^0 \\ \kappa_s^0\end{bmatrix}\end{aligned} \tag{19}$$

Or in a combined form:

$$[\sigma]_{x,y}^k = [Q]_{x,y}^k[\varepsilon^0]_{x,y} + z[Q]_{x,y}^k[\kappa^0]_{x,y} \tag{20}$$

1.2.3. Force and Moment Resultants

Due to the discontinuous stresses from layer to layer, it is easier to deal with the integrated effect of stresses on the laminate. Therefore, force and moment related expressions are needed to study laminate deformation. For kth layer of a laminate, the stresses can be replaced by the resultant forces and moments:

$$\begin{bmatrix} N_x^k \\ N_y^k \\ N_s^k \end{bmatrix} = \int_{-t/2}^{t/2} \begin{bmatrix} \sigma_x \\ \sigma_y \\ \sigma_s \end{bmatrix} dz \tag{21}$$

$$\begin{bmatrix} M_x^k \\ M_y^k \\ M_s^k \end{bmatrix} = \int_{-t/2}^{t/2} \begin{bmatrix} \sigma_x \\ \sigma_y \\ \sigma_s \end{bmatrix} z dz \tag{22}$$

where t is the thickness of kth layer; z is the z-coordinate of a point; N_x^k, N_y^k are normal forces per unit length, N_s^k is the shear strength per unit length; M_x^k, M_y^k are bending moments per unit length, M_s^k is twisting moment per unit length.

For a n-ply laminate, the total force and moment resultants can be obtained by summing the effect of each layer as:

$$\begin{bmatrix} N_x^k \\ N_y^k \\ N_s^k \end{bmatrix} = \sum_{k=1}^{n} \int_{z_{k-1}}^{z_k} \begin{bmatrix} \sigma_x \\ \sigma_y \\ \sigma_s \end{bmatrix} dz$$

$$\begin{bmatrix} M_x^k \\ M_y^k \\ M_s^k \end{bmatrix} = \sum_{k=1}^{n} \int_{z_{k-1}}^{z_k} \begin{bmatrix} \sigma_x \\ \sigma_y \\ \sigma_s \end{bmatrix} z dz \tag{23}$$

When taking integration of the above equations, the stiffness $[Q]_{x,y}^{k}$, reference plane strains $[\varepsilon^0]_{x,y}$ and curvatures $[\kappa]_{x,y}$ can be taken out since they are not functions of z. Therefore the integration can be determined as:

$$
\begin{aligned}
[N]_{x,y} &= \left[\sum_{k=1}^{n}[Q]_{x,y}^{k}\int_{z_{k-1}}^{z_k}dz\right][\varepsilon^0]_{x,y} + \left[\sum_{k=1}^{n}[Q]_{x,y}^{k}\int_{z_{k-1}}^{z_k}zdz\right][\kappa]_{x,y} \\
&= \left[\sum_{k=1}^{n}[Q]_{x,y}^{k}(z_k - z_{k-1})\right][\varepsilon^0]_{x,y} + \left[\frac{1}{2}\sum_{k=1}^{n}[Q]_{x,y}^{k}(z_k^2 - z_{k-1}^2)\right][\kappa]_{x,y} \\
&= [A]_{x,y}[\varepsilon^0]_{x,y} + [B]_{x,y}[\kappa]_{x,y}
\end{aligned}
\tag{24}
$$

$$
\begin{aligned}
[M]_{x,y} &= \left[\frac{1}{2}\sum_{k=1}^{n}[Q]_{x,y}^{k}(z_k^2 - z_{k-1}^2)\right][\varepsilon^0]_{x,y} + \left[\frac{1}{3}\sum_{k=1}^{n}[Q]_{x,y}^{k}(z_k^3 - z_{k-1}^3)\right][\kappa]_{x,y} \\
&= [B]_{x,y}[\varepsilon^0]_{x,y} + [D]_{x,y}[\kappa]_{x,}
\end{aligned}
\tag{25}
$$

where

$$
\begin{aligned}
A_{ij} &= \sum_{k=1}^{n} Q_{ij}^{k}\,(z_k - z_{-1}) \\
B_{ij} &= \frac{1}{2}\sum_{k=1}^{n} Q_{ij}^{k}\,(z_k^2 - z_{k-1}^2) \\
D_{ij} &= \frac{1}{3}\sum_{k=1}^{n} Q_{ij}^{k}\,(z_k^3 - z_{k-1}^3)
\end{aligned}
\tag{26}
$$

with *i,j* =*x*, *y*, *s*.

The matrix [A] is extensional stiffness matrix relating in-plane loads to strains; [B] is coupling stiffness matrix relating in-plane loads to curvatures and moments to in-plane strains; [C] is bending laminate stiffness matrix relating moments to curvatures.

The in-plane force and moment resultants related to the reference plane strains and curvatures can also be expressed in a combined form as:

$$\begin{bmatrix} N_x \\ N_y \\ N_s \\ \cdots \\ M_x \\ M_y \\ M_s \end{bmatrix} = \begin{bmatrix} A_{xx} & A_{xy} & A_{xs} \vdots B_{xx} & B_{xy} & B_{xs} \\ A_{yx} & A_{yy} & A_{ys} \vdots B_{yx} & B_{yy} & B_{ys} \\ A_{sx} & A_{sy} & A_{ss} \vdots B_{sx} & B_{sy} & B_{ss} \\ \cdots & \cdots & \cdots \cdots \cdots & \cdots & \cdots & \cdots \\ B_{xx} & B_{xy} & B_{xs} \vdots D_{xx} & D_{xy} & D_{xs} \\ B_{yx} & B_{yy} & B_{ys} \vdots D_{yx} & D_{yy} & D_{ys} \\ B_{sx} & B_{sy} & B_{ss} \vdots D_{sx} & D_{sy} & D_{ss} \end{bmatrix} \begin{bmatrix} \varepsilon_x^0 \\ \varepsilon_y^0 \\ \gamma_s^0 \\ \cdots \\ \kappa_x^0 \\ \kappa_y^0 \\ \kappa_{xy}^0 \end{bmatrix} \tag{27}$$

1.2.4. Hygrothermal Effects

In addition to the external loads, normally when a material experiences a temperature and/or moisture content change, it will deform to some extent and may cause residual stresses and warpage. This is the so called hygrothermal effect. When a unidirectional lamina is subjected to a uniform temperature change (ΔT) and moisture concentration change (Δc), it will produce hygrothermal deformation. Assuming the thermal and moisture expansion coefficients are constant and the thermal and moisture expansions are not coupled, the hygrothermal strains referred to its principle material axes are:

$$\begin{bmatrix} e_1 \\ e_2 \\ e_6 \end{bmatrix} = \begin{bmatrix} \alpha_1 \\ \alpha_2 \\ 0 \end{bmatrix} \Delta T + \begin{bmatrix} \beta_1 \\ \beta_2 \\ 0 \end{bmatrix} \Delta c \tag{28}$$

where $[e_i]$ is the hygrothermal effect strain matrix; $[\alpha_i]$ and $[\beta_i]$ are the thermal and moisture expansion coefficient matrix; ΔT is the temperature change; Δc is the moisture concentration change.

The transformation of hygrothermal strains to the geometric axes is given by:

$$e_x = e_1 m^2 + e_2 n^2$$

$$e_x = e_1 n^2 + e_2 m^2 \tag{29}$$

$$e_s = e_{xy} = 2(e_1 - e_2)mn$$

where $m = \cos\theta$, $\mathrm{n} = \sin\theta$.

When a multidirectional laminate is subjected to mechanical and hygrothermal load, the load-deformation relations of the *k*th lamina are given below based on the hygrothermalelastic superposition principle:

$$\begin{bmatrix}\varepsilon_x \\ \varepsilon_y \\ \gamma_s\end{bmatrix}_k = \begin{bmatrix}S_{xx} & S_{xy} & S_{xs} \\ S_{yx} & S_{yy} & S_{ys} \\ S_{sx} & S_{sy} & S_{ss}\end{bmatrix}_k \begin{bmatrix}\sigma_x \\ \sigma_y \\ \tau_s\end{bmatrix}_k + \begin{bmatrix}e_x \\ e_y \\ e_s\end{bmatrix}_k \tag{30}$$

The stresses in *k*th lamina can then be determined by:

$$\begin{aligned}\begin{bmatrix}\sigma_x \\ \sigma_y \\ \tau_s\end{bmatrix}_k &= \begin{bmatrix}Q_{xx} & Q_{xy} & Q_{xs} \\ Q_{yx} & Q_{yy} & Q_{ys} \\ Q_{sx} & Q_{sy} & Q_{ss}\end{bmatrix}_k \begin{bmatrix}\varepsilon_x - e_x \\ \varepsilon_y - e_y \\ \gamma_s - e_s\end{bmatrix}_k \\ &= \begin{bmatrix}Q_{xx} & Q_{xy} & Q_{xs} \\ Q_{yx} & Q_{yy} & Q_{ys} \\ Q_{sx} & Q_{sy} & Q_{ss}\end{bmatrix}_k \begin{bmatrix}\varepsilon_x^0 + z\kappa_x - e_x \\ \varepsilon_y^0 + z\kappa_y - e_y \\ \gamma_x^0 + z\kappa_x - e_s\end{bmatrix}_k\end{aligned} \tag{31}$$

By integration, the force and moment resultants are given by:

$$\begin{bmatrix} N_x \\ N_y \\ N_s \end{bmatrix} = \begin{bmatrix} A_{xx} & A_{xy} & A_{xs} \\ A_{yx} & A_{yy} & A_{ys} \\ A_{sx} & A_{sy} & A_{ss} \end{bmatrix} \begin{bmatrix} \varepsilon_x^0 \\ \varepsilon_y^0 \\ \gamma_s^0 \end{bmatrix} + \begin{bmatrix} B_{xx} & B_{xy} & B_{xs} \\ B_{yx} & B_{yy} & B_{ys} \\ B_{sx} & B_{sy} & B_{ss} \end{bmatrix} \begin{bmatrix} \kappa_x \\ \kappa_y \\ \kappa_s \end{bmatrix} - \begin{bmatrix} N_x^{HT} \\ N_y^{HT} \\ N_s^{HT} \end{bmatrix}$$

$$\begin{bmatrix} M_x \\ M_y \\ M_s \end{bmatrix} = \begin{bmatrix} B_{xx} & B_{xy} & B_{xs} \\ B_{yx} & B_{yy} & B_{ys} \\ B_{sx} & B_{sy} & B_{ss} \end{bmatrix} \begin{bmatrix} \varepsilon_x^0 \\ \varepsilon_y^0 \\ \gamma_s^0 \end{bmatrix} + \begin{bmatrix} D_{xx} & D_{xy} & D_{xs} \\ D_{yx} & D_{yy} & D_{ys} \\ D_{sx} & D_{sy} & D_{ss} \end{bmatrix} \begin{bmatrix} \kappa_x \\ \kappa_y \\ \kappa_s \end{bmatrix} - \begin{bmatrix} M_x^{HT} \\ M_y^{HT} \\ M_s^{HT} \end{bmatrix} \quad (32)$$

where the hygrothermal force and moment resultants are defined as:

$$\begin{bmatrix} N_x^{HT} \\ N_y^{HT} \\ N_s^{HT} \end{bmatrix} = \sum_{k=1}^{n} \begin{bmatrix} Q_{xx} & Q_{xy} & Q_{xs} \\ Q_{yx} & Q_{yy} & Q_{ys} \\ Q_{sx} & Q_{sy} & Q_{ss} \end{bmatrix}_k \begin{bmatrix} e_x \\ e_y \\ e_s \end{bmatrix}_k t_k \quad (33)$$

$$\begin{bmatrix} M_x^{HT} \\ M_y^{HT} \\ M_s^{HT} \end{bmatrix} = \sum_{k=1}^{n} \begin{bmatrix} Q_{xx} & Q_{xy} & Q_{xs} \\ Q_{yx} & Q_{yy} & Q_{ys} \\ Q_{sx} & Q_{sy} & Q_{ss} \end{bmatrix}_k \begin{bmatrix} e_x \\ e_y \\ e_s \end{bmatrix}_k \bar{z}_k t_k \quad (34)$$

where t_k is the thickness of *k*th lamina, $\bar{z}_k = (z_k + z_{k-1})/2$.

Rearranging Equation (32) gives:

$$\begin{bmatrix} \bar{N}_x \\ \bar{N}_y \\ \bar{N}_s \end{bmatrix} = \begin{bmatrix} N_x \\ N_y \\ N_s \end{bmatrix} + \begin{bmatrix} N_x^{HT} \\ N_y^{HT} \\ N_s^{HT} \end{bmatrix} = \begin{bmatrix} A_{xx} & A_{xy} & A_{xs} \\ A_{yx} & A_{yy} & A_{ys} \\ A_{sx} & A_{sy} & A_{ss} \end{bmatrix} \begin{bmatrix} \varepsilon_x^0 \\ \varepsilon_y^0 \\ \gamma_s^0 \end{bmatrix} + \begin{bmatrix} B_{xx} & B_{xy} & B_{xs} \\ B_{yx} & B_{yy} & B_{ys} \\ B_{sx} & B_{sy} & B_{ss} \end{bmatrix} \begin{bmatrix} \kappa_x^0 \\ \kappa_y^0 \\ \kappa_{xy}^0 \end{bmatrix}$$

$$\begin{bmatrix} \bar{M}_x \\ \bar{M}_y \\ \bar{M}_s \end{bmatrix} = \begin{bmatrix} M_x \\ M_y \\ M_s \end{bmatrix} + \begin{bmatrix} M_x^{HT} \\ M_y^{HT} \\ M_s^{HT} \end{bmatrix} = \begin{bmatrix} B_{xx} & B_{xy} & B_{xs} \\ B_{yx} & B_{yy} & B_{ys} \\ B_{sx} & B_{sy} & B_{ss} \end{bmatrix} \begin{bmatrix} \varepsilon_x^0 \\ \varepsilon_y^0 \\ \gamma_s^0 \end{bmatrix} + \begin{bmatrix} D_{xx} & D_{xy} & D_{xs} \\ D_{yx} & D_{yy} & D_{ys} \\ D_{sx} & D_{sy} & D_{ss} \end{bmatrix} \begin{bmatrix} \kappa_x^0 \\ \kappa_y^0 \\ \kappa_{xy}^0 \end{bmatrix} \quad (35)$$

where $[\bar{N}]$ and $[\bar{M}]$ are the total force and moment resultants equivalent to the sums of mechanical and hygrothermal components, respectively.

Since strains are continuous through the laminate thickness, it is more preferable to deal with strains. The inversion of load-deformation and moment-deformation relations in a combined form gives the strains and curvatures of the reference plane:

$$\begin{bmatrix} \varepsilon_x^0 \\ \varepsilon_y^0 \\ \gamma_s^0 \\ \cdots \\ \kappa_x^0 \\ \kappa_y^0 \\ \kappa_{xy}^0 \end{bmatrix} = \begin{bmatrix} a_{xx} & a_{xy} & a_{xs} \vdots b_{xx} & b_{xy} & b_{xs} \\ a_{yx} & a_{yy} & a_{ys} \vdots b_{yx} & b_{yy} & b_{ys} \\ a_{sx} & a_{sy} & a_{ss} \vdots b_{sx} & b_{sy} & b_{ss} \\ \cdots & \cdots & \cdots \cdots \cdots & \cdots & \cdots \\ b_{xx} & b_{xy} & b_{xs} \vdots d_{xx} & d_{xy} & d_{xs} \\ b_{yx} & b_{yy} & b_{ys} \vdots d_{yx} & d_{yy} & d_{ys} \\ b_{sx} & b_{sy} & b_{ss} \vdots d_{sx} & d_{sy} & d_{ss} \end{bmatrix} \begin{bmatrix} \bar{N}_x \\ \bar{N}_y \\ \bar{N}_s \\ \cdots \\ \bar{M}_x \\ \bar{M}_y \\ \bar{M}_s \end{bmatrix} \tag{36}$$

For unloaded laminate, the hygrothermoelastic relations can be reduced as:

$$\begin{bmatrix} N_x^{HT} \\ N_y^{HT} \\ N_s^{HT} \end{bmatrix} = \begin{bmatrix} A_{xx} & A_{xy} & A_{xs} \\ A_{yx} & A_{yy} & A_{ys} \\ A_{sx} & A_{sy} & A_{ss} \end{bmatrix} \begin{bmatrix} \varepsilon_x^0 \\ \varepsilon_y^0 \\ \varepsilon_s^0 \end{bmatrix} + \begin{bmatrix} B_{xx} & B_{xy} & B_{xs} \\ B_{yx} & B_{yy} & B_{ys} \\ B_{sx} & B_{sy} & B_{ss} \end{bmatrix} \begin{bmatrix} \kappa_x^0 \\ \kappa_y^0 \\ \kappa_{xy}^0 \end{bmatrix}$$

$$\begin{bmatrix} M_x^{HT} \\ M_y^{HT} \\ M_s^{HT} \end{bmatrix} = \begin{bmatrix} B_{xx} & B_{xy} & B_{xs} \\ B_{yx} & B_{yy} & B_{ys} \\ B_{sx} & B_{sy} & B_{ss} \end{bmatrix} \begin{bmatrix} \varepsilon_x^0 \\ \varepsilon_y^0 \\ \varepsilon_s^0 \end{bmatrix} + \begin{bmatrix} D_{xx} & D_{xy} & D_{xs} \\ D_{yx} & D_{yy} & D_{ys} \\ D_{sx} & D_{sy} & D_{ss} \end{bmatrix} \begin{bmatrix} \kappa_x^0 \\ \kappa_y^0 \\ \kappa_{xy}^0 \end{bmatrix} \tag{37}$$

Similarly, the inversion gives the reference plane strains and curvatures:

$$\begin{bmatrix} \varepsilon_x^0 \\ \varepsilon_y^0 \\ \varepsilon_s^0 \end{bmatrix} = \begin{bmatrix} a_{xx} & a_{xy} & a_{xs} \\ a_{yx} & a_{yy} & a_{ys} \\ a_{sx} & a_{sy} & a_{ss} \end{bmatrix} \begin{bmatrix} N_x^{HT} \\ N_y^{HT} \\ N_s^{HT} \end{bmatrix} + \begin{bmatrix} b_{xx} & b_{xy} & b_{xs} \\ b_{yx} & b_{yy} & b_{ys} \\ b_{sx} & b_{sy} & b_{ss} \end{bmatrix} \begin{bmatrix} M_x^{HT} \\ M_y^{HT} \\ M_s^{HT} \end{bmatrix}$$

$$\begin{bmatrix} \kappa_x^0 \\ \kappa_y^0 \\ \kappa_{xy}^0 \end{bmatrix} = \begin{bmatrix} c_{xx} & c_{xy} & c_{xs} \\ c_{yx} & c_{yy} & c_{ys} \\ c_{sx} & c_{sy} & c_{ss} \end{bmatrix} \begin{bmatrix} N_x^{HT} \\ N_y^{HT} \\ N_s^{HT} \end{bmatrix} + \begin{bmatrix} d_{xx} & d_{xy} & d_{xs} \\ d_{yx} & d_{yy} & d_{ys} \\ d_{sx} & d_{sy} & d_{ss} \end{bmatrix} \begin{bmatrix} M_x^{HT} \\ M_y^{HT} \\ M_s^{HT} \end{bmatrix} \tag{38}$$

1.3. Deformation Monitoring – ARAMIS Adjustable

In the previous sections, stress, strain and deformation relations have been discussed. The deformation measurement technique should now be introduced. Though there exist several different approaches to measure the deformation, digital imaging correlation (DIC) is used here. DIC is a full-field image analysis method and can determine the displacements and contour of an object either loaded or unloaded in two or three dimensions. The correlation algorithm is based on the tracking of grey values of in small local neighborhood facets (Dantec Dynamics, 2018).

As one of the DIC measuring systems, ARAMIS Adjustable (shown in Figure 3.5) is chosen here due to advantages such as live tracking, high resolution and non-contact measurement. It can be used for point-based or full-field analysis of either statically or dynamically loaded elements. According to measuring volumes and distances, different pairs of sensors can be used and thus offer a wide measurement range.

Figure 3.5. ARAMIS Adjustable with sensors and dual LED illumination mounted.

1.4. Warping Studies on CLT

Due to its crosswise layup, cross-laminated timber exhibits great strength properties and dimensional stabilities. However, being a hygroscopic material, CLT also suffers from moisture induced issues. Numerous studies have been conducted on the strength properties and moisture

related issues on CLT (Gereke et al., 2009; Gereke et al., 2010; Gereke, Gustafsson et al., 2011; Hochreiner et al., 2014; Stürzenbecher et al., 2010).

Among them, experimental and numerical hygroscopic warping studies of 3-layer Norway spruce cross-laminated timber panels glued with polyurethane were conducted by Gereke et al. (Gereke et al., 2009; Gereke et al., 2011). Good agreement was obtained between experimental and numerical data. Results indicated that stiffness, the moisture-induced swelling and the mechano-sorptive coefficient in the minor direction have major influences on the hygroscopic warping of 3-layer CLT panels. Furthermore, the studies showed that these parameters could be controlled by changing layer ratio (ratio of the total outer layer thickness to panel thickness) and annual growth ring orientation. A 45° orientation of the annual growth ring was recommended due to the low stiffness perpendicular to the grain which leads to small couplings. Layer ratio was suggested to be as small as possible without losing the mechanical restraint effect due to cross lamination.

In a work that tried to experimentally identify the failure mechanisms of CLT panels (made of Norway spruce, glued with polyurethane) subjected to concentrated load, linear variable differential transformer (LVDTs) and digital image correlation (DIC) measurement system ARAMIS were used to obtain information on warping and shear distortion (Hochreiner et al., 2014). It found, as compared to LVDTs, that ARAMIS was very reliable in obtaining the horizontal displacement. An example of the cross section warping at different load levels is shown in Figure 3.6, from which an almost linear distribution of layer-wise horizontal displacement can be observed.

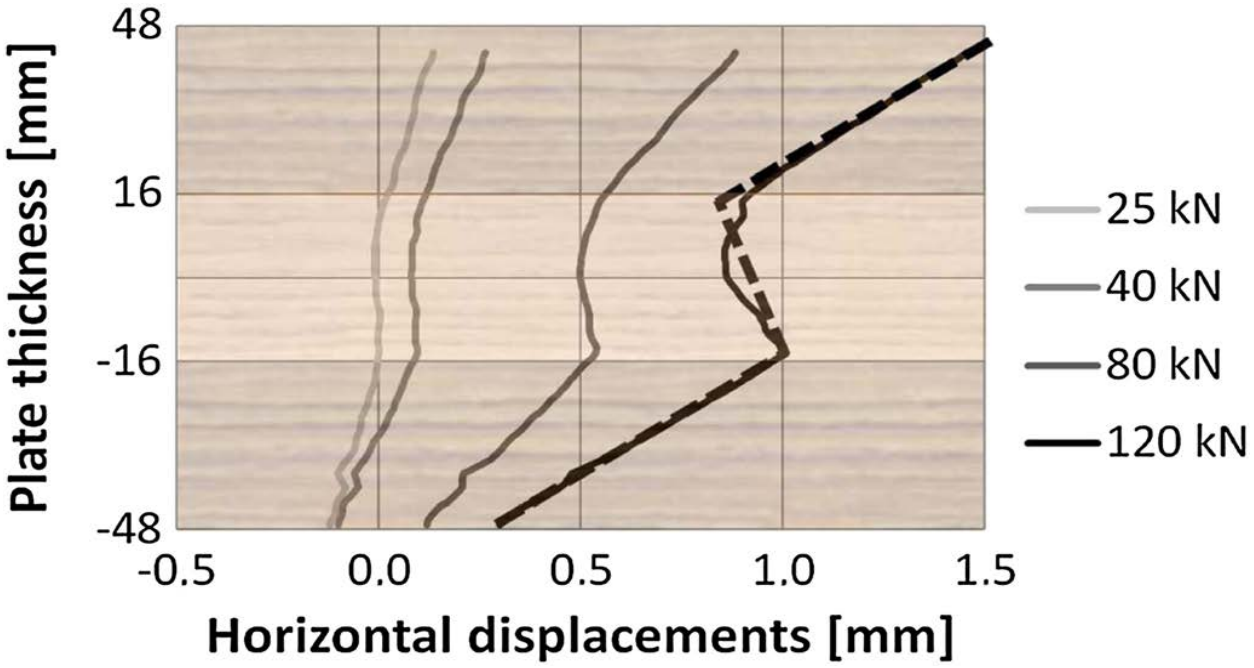

Figure 3.6. Warping at different loads (Hochreiner et al., 2014)

2. Problem Statement and Objectives

When used in construction, the strength properties and dimensional stability of CLT panels is of vital importance as demanded by many regulations. There have been numerous studies on this subject, and several models have been developed to predict warping behavior (Gereke et al., 2009; Ormarsson et al., 1998). However, due to wood species and adhesive type differences, more research needs to be done on the warping of CLT panels.

The overall goal of this study is to evaluate the suitability of the hygrothermal model and determine the effect of different adhesives (polyurethane, phenol resorcinol formaldehyde, and melamine formaldehyde) on the warping of 3-layer edge glued **southern pine** cross-laminated timber.

The hypotheses are:

- ARAMIS Adjustable is suitable for southern pine CLT warping measurement.
- Adhesive types have no or little effect on warping of southern pine CLT.
- Hygrothermal modeling may be used to estimate the warping of CLT panels.

3. Materials and Methods:

The 3-layer CLT panels were made of flatsawn southern yellow pine lumber bought from a local store in Raleigh, North Carolina. All lumber was ripped and planed to 1cm × 10cm (thickness × width) after purchase, then conditioned at 65% RH, 20℃ in a climate chamber. After equilibrium, lumber was cut to 30 cm long, then edge glued to make laminas 1cm × 30cm × 30cm (thickness × length × width). Three laminas were face glued according to the procedures specified by adhesive manufactures to make CLT panels with the dimensions of 30cm × 30cm × 3cm (thickness × length × width). Three commonly used adhesives were chosen in this study, namely phenol resorcinol formaldehyde (PRF), melamine formaldehyde (MF) and polyurethane (PU). In total, six CLT panels were made, two for each adhesive. Once made, the edges of each panel were sealed with DAP SiliconePlus to force one dimensional moisture transfer, then conditioned at 65% RH, 20℃ again until equilibrium.

Then panels were placed in a custom designed container filled with distilled water on three supports as shown in Figure 3.7. The gaps between the container sides and panel edges were sealed with plastic wraps and DAP SiliconePlus. Once assembled, the whole setup was stored in the climate chamber at 65% RH, 20℃, so that a 65%/100% RH gradient could be maintained across the panel thickness.

Warping measurements were performed on days 1, 2, 4, 7, 14, 21, 35 and 42 by ARAMIS Adjustable. For each sample, the z-directional displacement measurements were made on 9 points, shown as Point A, B, C, D, E, F, G, H and I in Figure 3.8. For each point, 6 pictures were taken at the frequency of 1 hertz, then the average was taken for further analysis (Equation 39-41). To facilitate the analysis thereafter, longitudinal and transverse directions of each sample's outermost layer coincided with the x and y axis of the ARAMIS Adjustable measuring

coordinate system respectively. The positions of measurements and supports are shown in Figure 3.8.

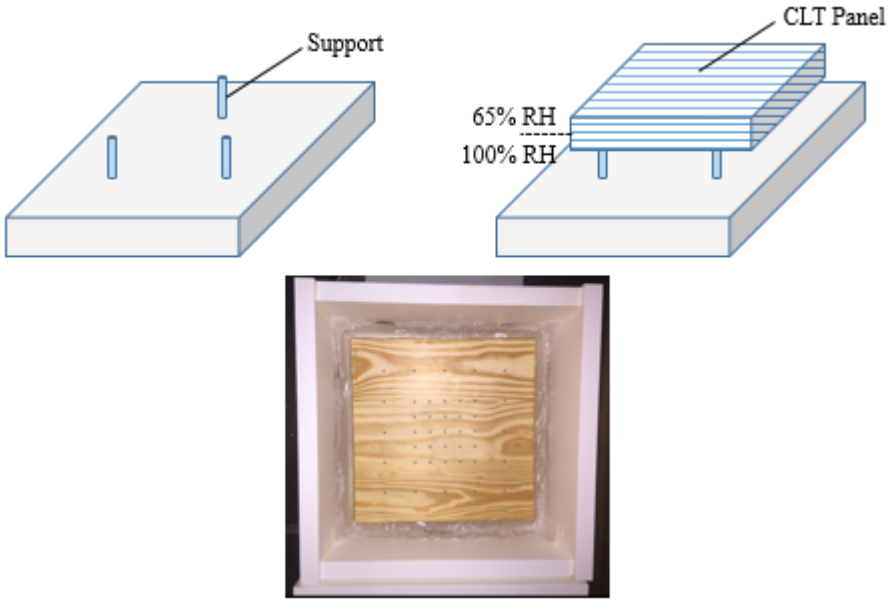

Figure 3.7. Warping test setup.

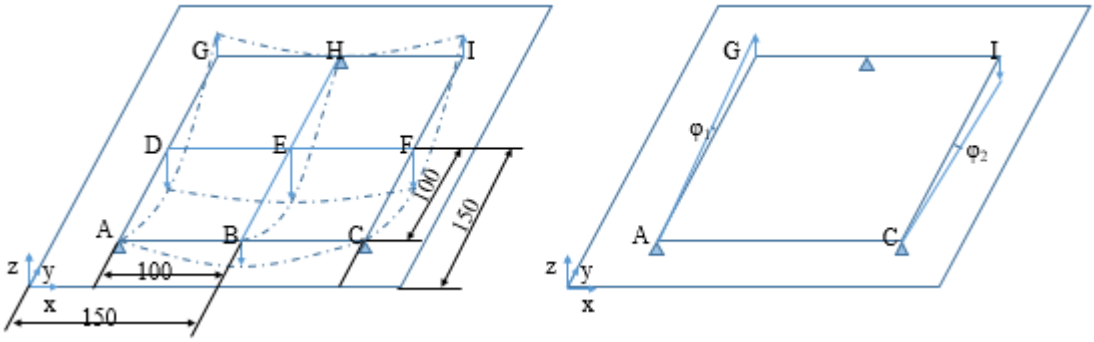

Figure 3.8. Measuring points (left) and definition of twist deformation (right).

The cup deformation in the x-z plane was determined by:

$$cup_{xz} = \frac{1}{2}(\bar{\mu}_z^{ADG} + \bar{\mu}_z^{CFI}) - \bar{\mu}_z^{BEH} \tag{39}$$

The cup deformation in the y-z plane was calculated by:

$$cup_{yz} = \frac{1}{2}(\bar{\mu}_z^{ABC} + \bar{\mu}_z^{GHI}) - \bar{\mu}_z^{DEF} \tag{40}$$

where $\bar{\mu}_z^{ijk}$ is the mean value of the displacement in the measuring points i, j and k.

The twist deformation was obtained by:

$$twist = |\varphi_1 - \varphi_2| = |\tan^{-1}(\mu_z^G/200) - \tan^{-1}(\mu_z^I/200)| \quad (41)$$

4. Results and Discussion

4.1. Deformation measurement resolution

As mentioned in Section 1.4, one of the advantages of ARAMIS Adjustable is its high resolution. It has to be pointed out that the in-plane deformation measurement resolution can be as high as several micrometers. However, when it comes to the out-of-plane deformation, which is the case for this CLT warping study, the resolution will be lower. Therefore, the resolution level has to be determined before the warping measurement.

This was carried out by measuring a sequence of deformations of a reference plate in a short period of time (one minute in this case), therefore deformation was assumed to be zero

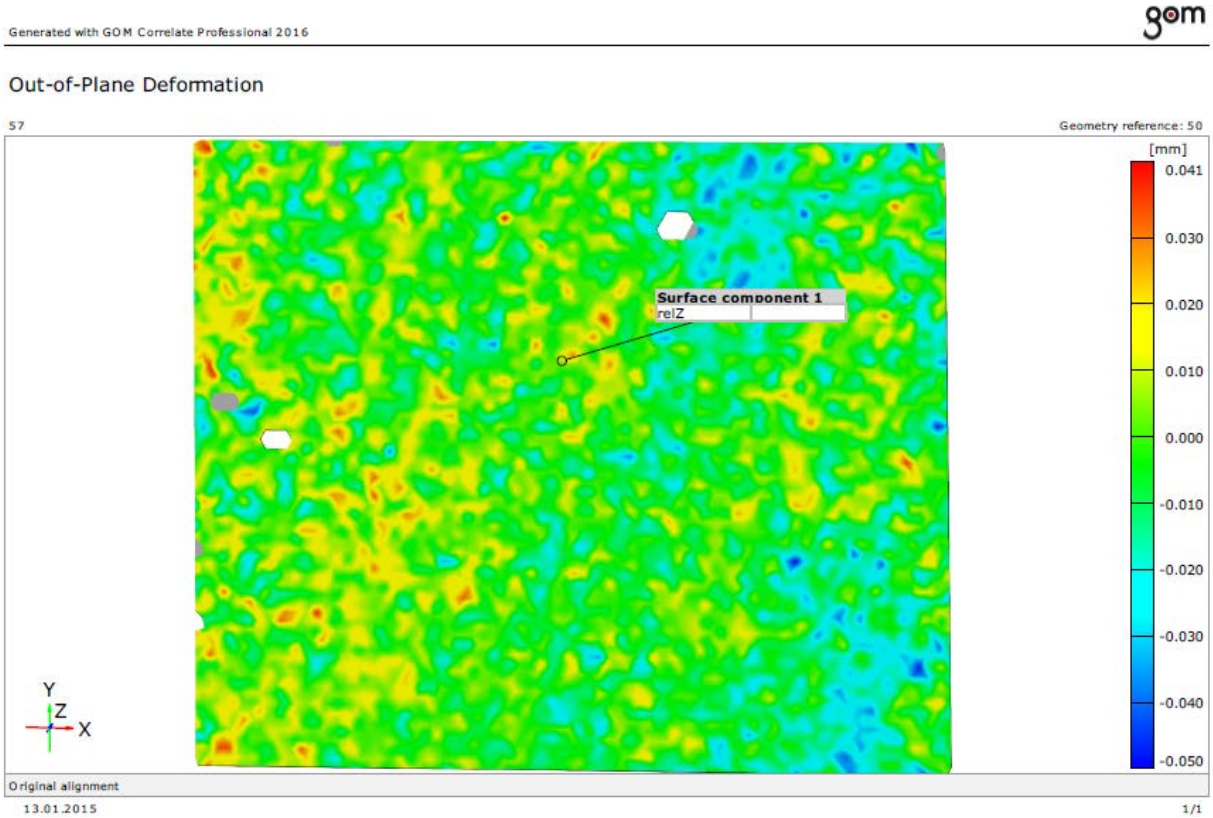

Figure 3.9. Out-of-plane deformation of reference plate.

during the measurement. The calculated deformation was then checked, as shown in Figure 3.9 (250mm×300mm). It can be seen that the deviation of z-deformation (out-of-plane) was about ±0.05mm, which is sufficiently high in terms of its measuring volume.

Then one 5-foot (1524 mm) arc mold and one 10-foot (3048 mm) arc mold were made to test the system's capability of measuring out of plane displacement. As shown in Figure 3.10-3.11, the radii obtained by ARAMIS Adjustable were 1568 mm and 3180 mm, respectively. The errors were less than 5%.

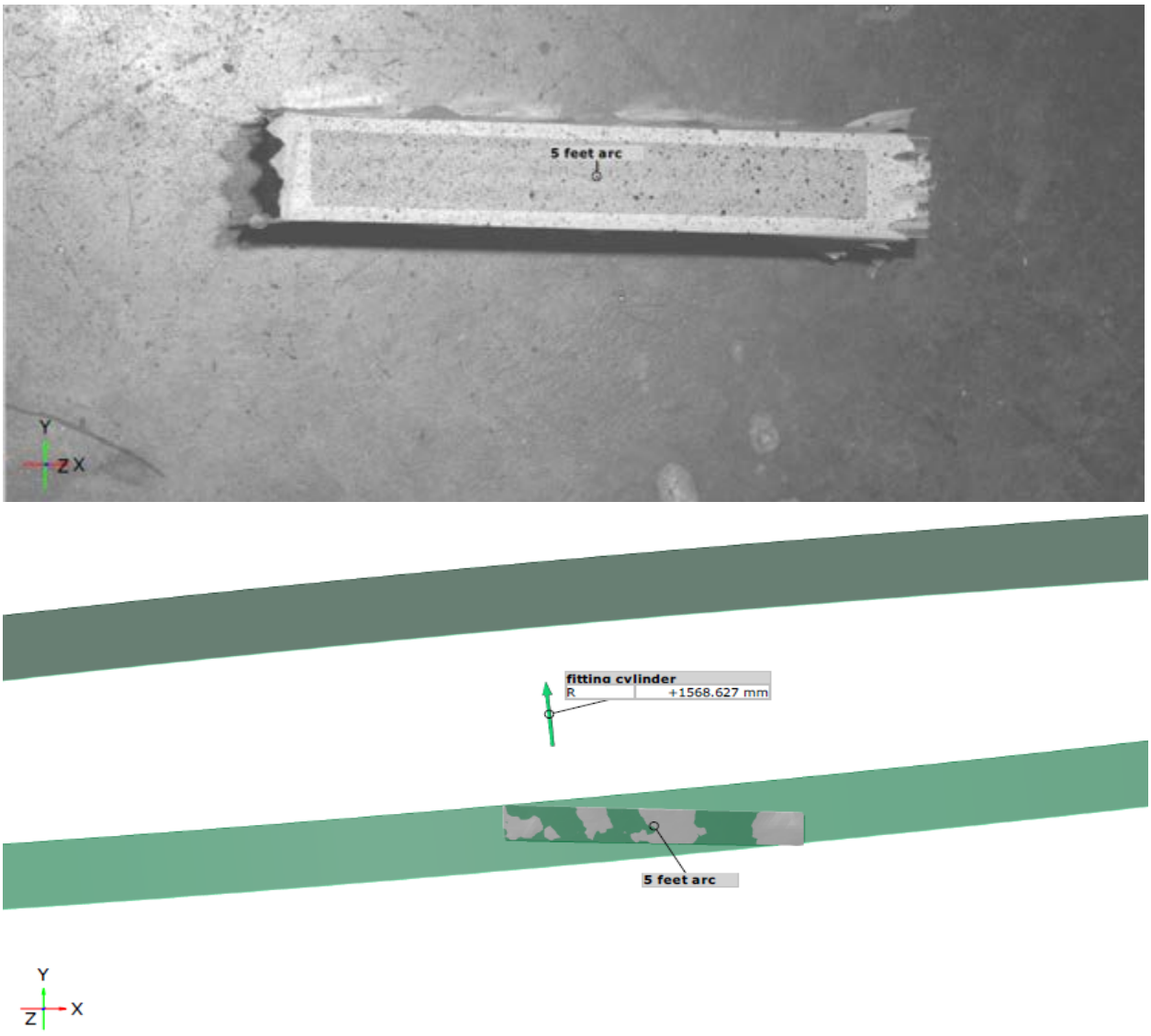

Figure 3.10. Five-foot arc mold (top) and fitting results by ARAMIS Adjustable.

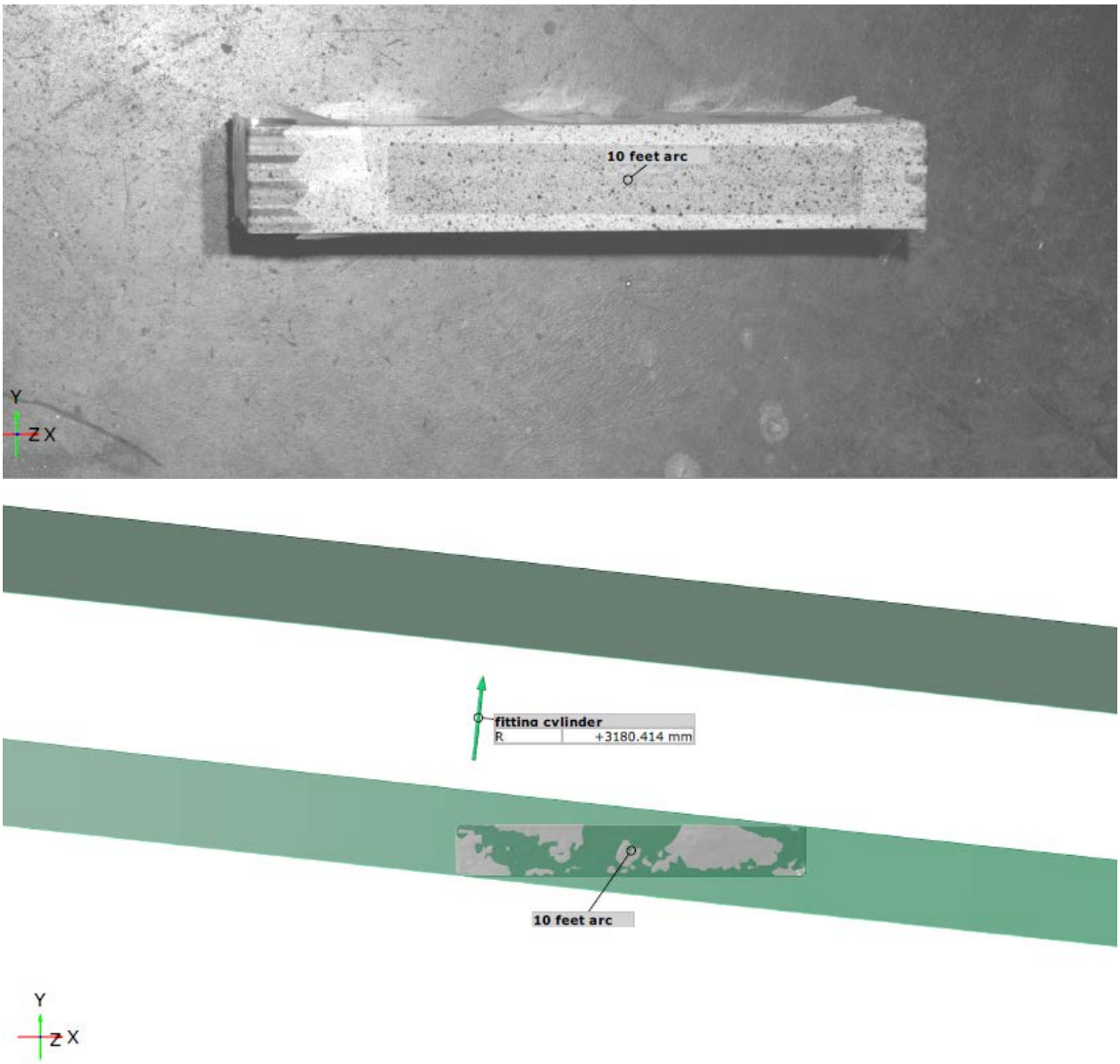

Figure 3.11. Ten-foot arc mold (top) and fitting results by ARAMIS Adjustable.

4.2. Warping measurement results

Results of warping measurements after 42 days are listed in Table 3.9. It can be seen that the warping in the yz-plane is greater than that in the xz-plane, with the cup_{yz} about two times larger than cup_{xz} for each sample. This is mainly due to y axis is along the tangential direction of the outer layers, while x axis is along the longitudinal direction.

Table 3.9. Results of warping measurement after 42 days.

	cup_{xz} (mm)	cup_{yz} (mm)	twist (^{o})
PU	0.115	0.333	0.168
PRF	0.162	0.423	0.133
MF	0.226	0.433	0.090

The warping development, including $cup_{yz,}$ cup_{xz} and twist, over time for PU glued southern pine CLT are presented in Figure 3.12-14. After the rapid increase in Figure 3.12, cup_{yz} reached its maximum between 10 to 15 days, then it kept decreasing at a much slower rate. This is well expected. As discussed in the Diffusion Chapter, the bottom layer picked up moisture quickly initially and caused large moisture content differences within and across layers. Hence initially, the swelling of the bottom layer was mainly along the y axis (or tangential direction). This resulted in a strong cup_{yz} increase. Then the middle layer and top layer also started to pick up moisture and swell in opposition to the swelling of bottom layer causing cup_{yz} to decrease after the maximum (around 0.45 mm) and cup_{xz} increased as a result. The cup_{xz} and twist however showed no maximum and kept increasing from the beginning.

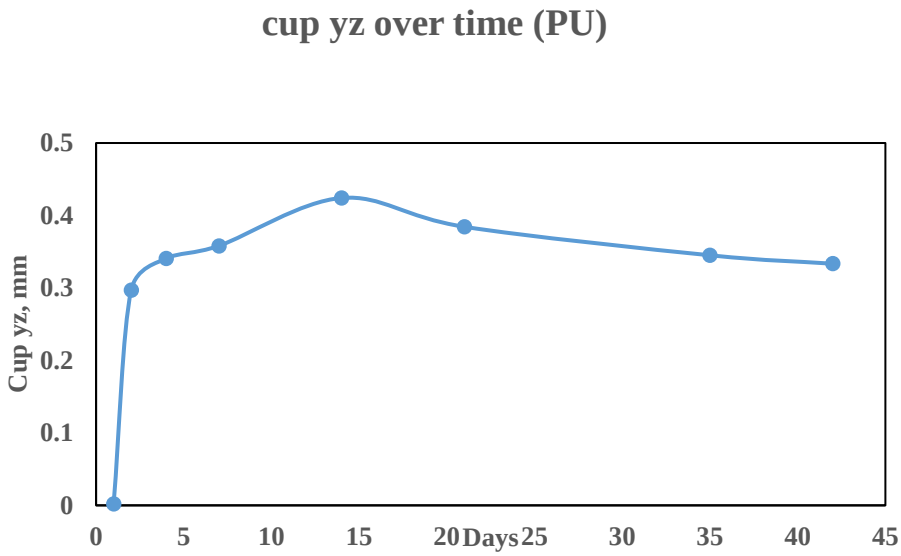

Figure 3.12. Development of cup_{yz} over time for PU glued southern pine CLT sample.

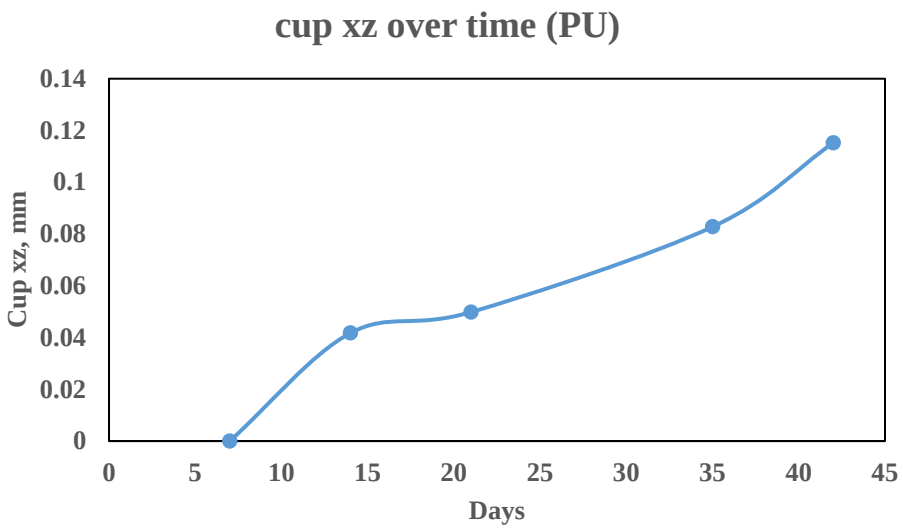

Figure 3.13. Development of cup_{xz} over time for PU glued southern pine CLT sample.

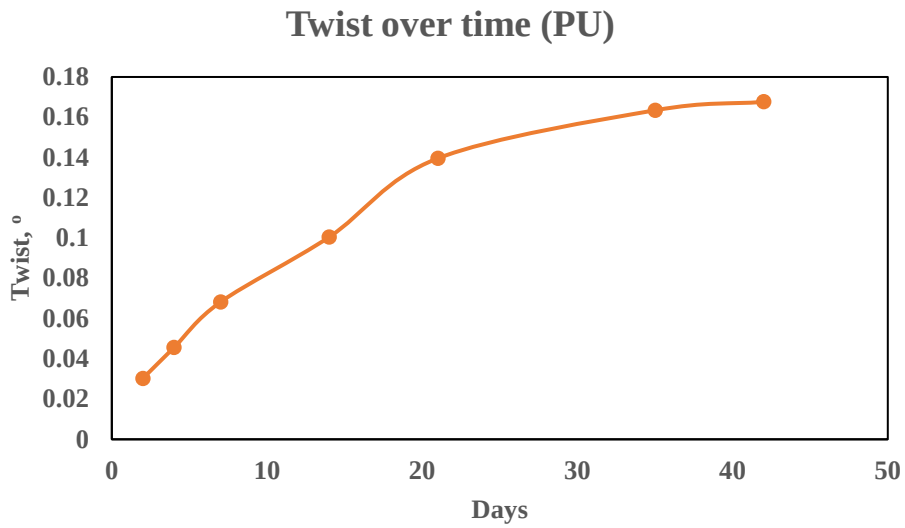

Figure 3.14. Development of twist over time for PU glued southern pine CLT sample.

The scenarios for PRF- and MF- glued southern pine CLT samples were similar as shown in Figure 3.15-17 and Figure 3.18-20. The maximum cup_{yz} were around 0.44mm and 0.52mm for PRF- and MF-glued samples respectively. The fact that they all behaved similarly is expected as the bonding of each adhesive is stronger than wood itself and it is proved in Diffusion Chapter that adhesive types have no or little effect on diffusion. Therefore, the trends of all 3 southern pine CLT were similar to each other.

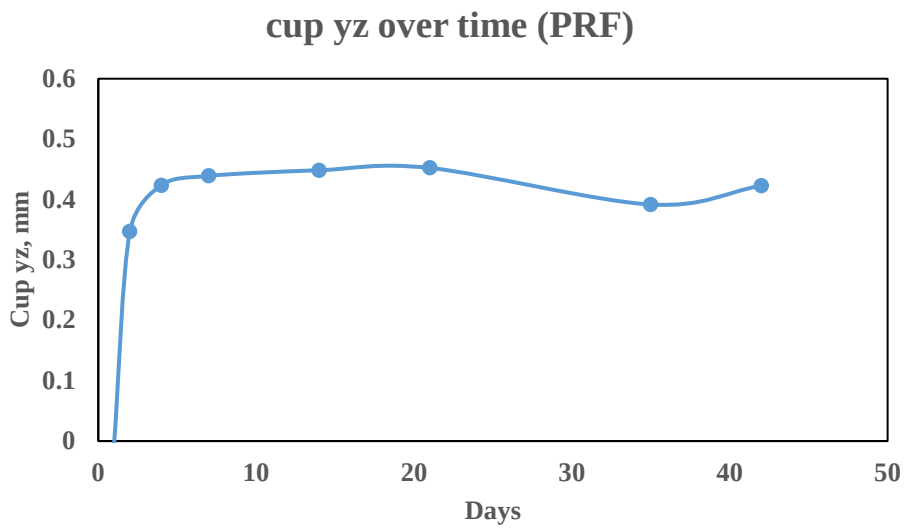

Figure 3.15. Development of cup_{yz} over time for PRF glued southern pine CLT sample.

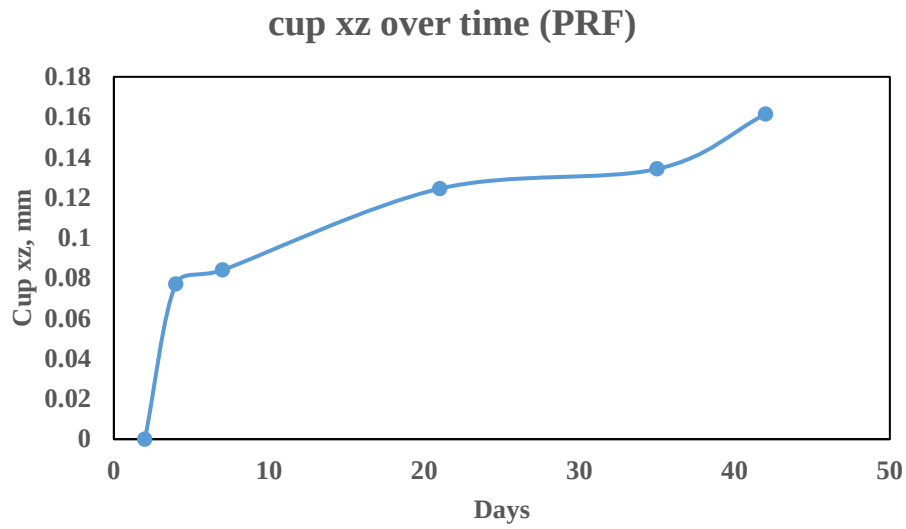

Figure 3.16. Development of cup_{xz} over time for PRF glued southern pine CLT sample.

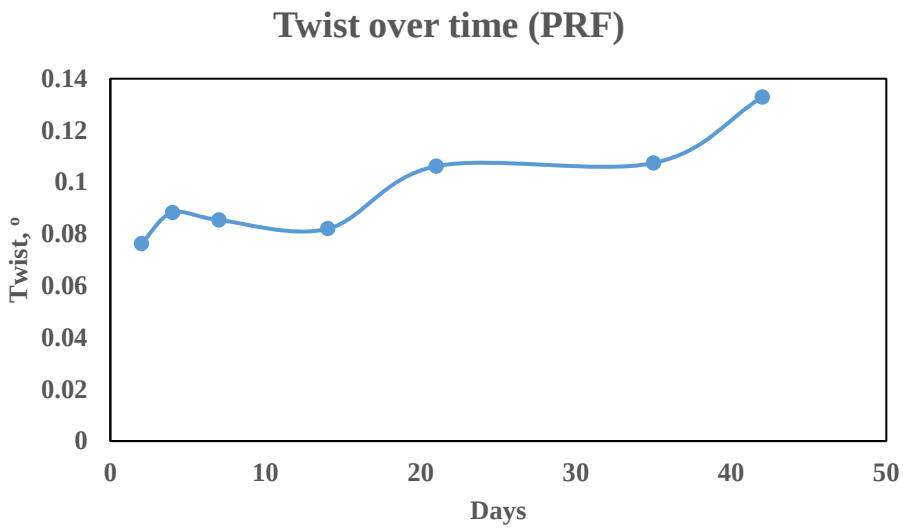

Figure 3.17. Development of twist over time for PRF glued southern pine CLT sample.

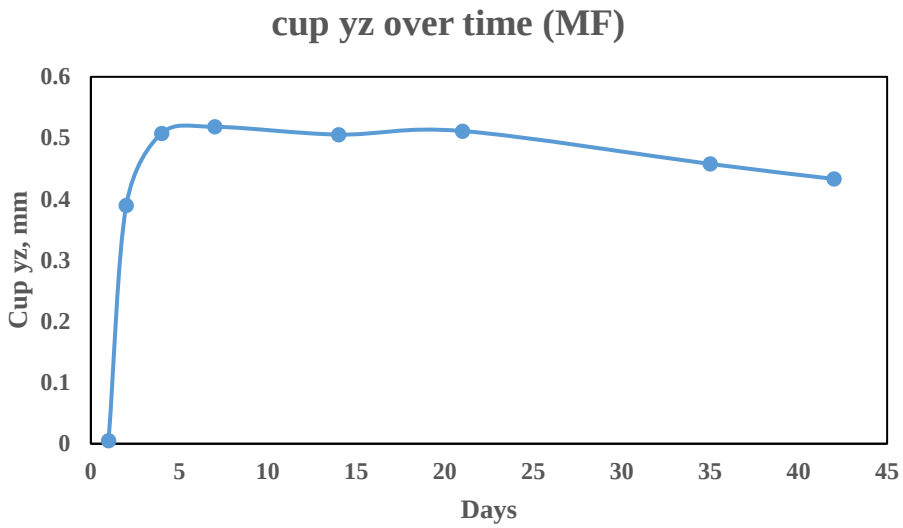

Figure 3.18. Development of cupyz over time for PRF glued southern pine CLT sample.

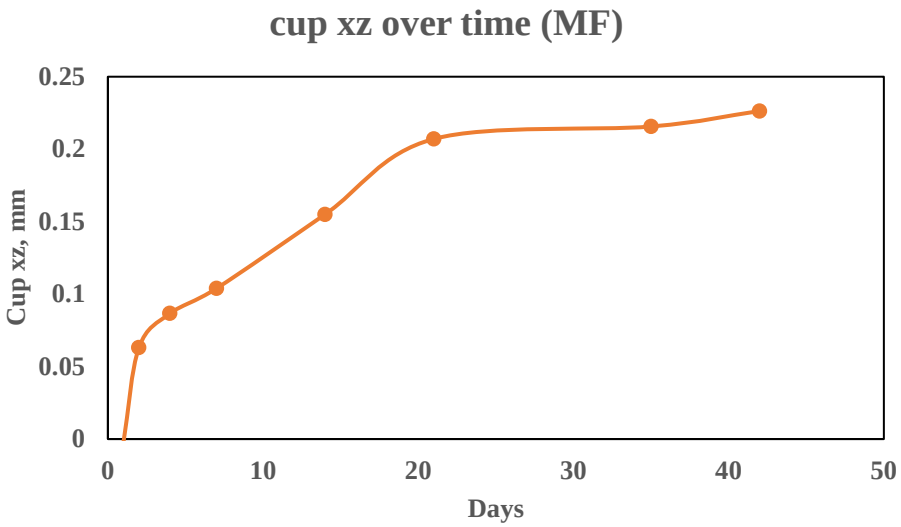

Figure 3.19. Development of cup_{xz} over time for PRF glued southern pine CLT sample.

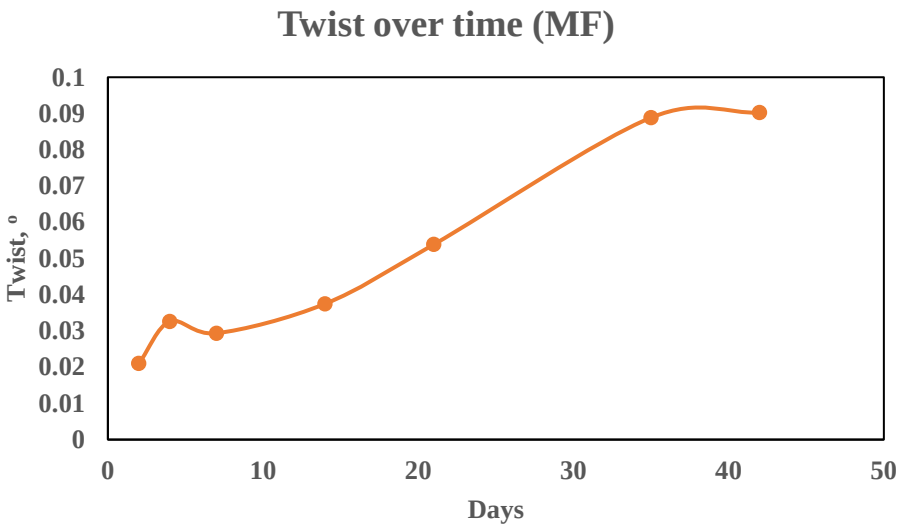

Figure 3.20. Development of twist over time for MF glued southern pine CLT sample.

4.3. Warping model

As discussed in Section 1.3, the hygrothermal warping model will be applied to southern pine CLT to study the warping effect. The elastic parameters at 12% moisture content from Wood Handbook are listed in Table 3.10. As mentioned in the Diffusion Chapter, the elastic properties increase with decreasing moisture content below fiber saturation point (FSP), therefore elastic properties can not be treated as constants when moisture content differs from

12%. Relations between moisture content and elastic properties need to be considered then. Based on Kretschmann's (2007) study on clear southern pine and the result of CLT moisture distribution in the Diffusion Chapter, the elastic parameters for individual layers of CLT were calculated and listed in Table 3.11.

Table 3.10. Elastic parameters at 12% moisture content from Wood Handbook

E1 (pa)	E2 (pa)	G12 (pa)	ν12	ν21
1.36E+10	6.69E+08	7.65E+08	0.292	0.014

Table 3.11. Elastic parameters for individual layers of CLT.

	E_1 (pa)	E_2 (pa)	G_{12} (pa)	ν_{12}	ν_{21}
Top	1.36E+10	6.69E+08	7.65E+08	0.292	0.014
Middle	1.23E+10	6.03E+08	7.26E+08	0.220	0.011
Bottom	7.49E+09	3.01E+08	4.59E+08	0.190	0.008

The configuration of southern pine CLT is [0/90/0], the longitudinal shrinkage coefficients is 0.00005 in/in/%MC, the transverse shrinkage coefficient is 0.0020 in/in/%MC. The thickness of each layer is 10 mm with a total of 30 mm for each CLT sample. As shown in the Diffusion Chapter, a linear moisture content distribution can be expected along the thickness direction (z-direction), which can be approximated by:

$$w = -300z + 17 \tag{42}$$

where w is the moisture content, %; z is the z coordinate, meters. Here for the middle plane or reference plane, z=0.

By substituting the parameters in Table 4, the shrinkage coefficients and Equation (39) into Equation (33) and (34) yields

$$\begin{bmatrix} N_x^{HT} \\ N_y^{HT} \\ N_s^{HT} \end{bmatrix} = \sum_{k=1}^{n} \int_{z_{k-1}}^{z_k} \begin{bmatrix} Q_{xx} & Q_{xy} & Q_{xs} \\ Q_{yx} & Q_{yy} & Q_{ys} \\ Q_{sx} & Q_{sy} & Q_{ss} \end{bmatrix}_k \begin{bmatrix} \beta_x \\ \beta_y \\ \beta_s \end{bmatrix}_k [12 - (-300z + 17)]dz \tag{43}$$

$$\begin{bmatrix} M_x^{HT} \\ M_y^{HT} \\ M_s^{HT} \end{bmatrix} = \sum_{k=1}^{n} \int_{z_{k-1}}^{z_k} \begin{bmatrix} Q_{xx} & Q_{xy} & Q_{xs} \\ Q_{yx} & Q_{yy} & Q_{ys} \\ Q_{sx} & Q_{sy} & Q_{ss} \end{bmatrix}_k \begin{bmatrix} \beta_x \\ \beta_y \\ \beta_s \end{bmatrix}_k [12 - (-300z + 17)]zdz \tag{44}$$

Integration of Equation (40) and (41) results in

$$\begin{bmatrix} N_x^{HT} \\ N_y^{HT} \\ N_{xy}^{HT} \end{bmatrix} = \begin{bmatrix} -123261 \\ -125864 \\ 0 \end{bmatrix} N/m$$

$$\begin{bmatrix} M_x^{HT} \\ M_y^{HT} \\ M_{xy}^{HT} \end{bmatrix} = \begin{bmatrix} -229.945 \\ 230.250 \\ 0 \end{bmatrix} Nm/m$$

Substituting the hygrothermal force and moment resultants above into Equation (38) gives the reference plane strain and curvatures as:

$$\begin{bmatrix} \varepsilon_x^0 \\ \varepsilon_y^0 \\ \gamma_{xy}^0 \\ \kappa_x^0 \\ \kappa_y^0 \\ \kappa_{xy}^0 \end{bmatrix} = \begin{bmatrix} -0.00063 \\ -0.00097 \\ 0 \\ 0.0259 \\ 0.1287 \\ 0 \end{bmatrix} \tag{45}$$

Then cup_{xz} and cup_{yz} can be determined by (see Figure 21):

$$\text{Cup} = \frac{(L+\Delta L)^2}{8(R-\frac{h}{2})} = \frac{(L+L\times\varepsilon^0)^2}{8(\frac{1}{\kappa}-\frac{h}{2})} \quad (46)$$

The results were 0.130mm and 0.645mm for cup_{xz} and cup_{yz}, respectively. Compared to warping measurement in Table 3.2, though the model predicted cup_{yz} does not agree so well, it gives a good estimation of the deformation given the fact that wood is an anisotropic material, the maximums of cup_{yz} were close to the predicted value. The predicted cup_{xz} agreed better with the measured value except for MF glued southern pine CLT.

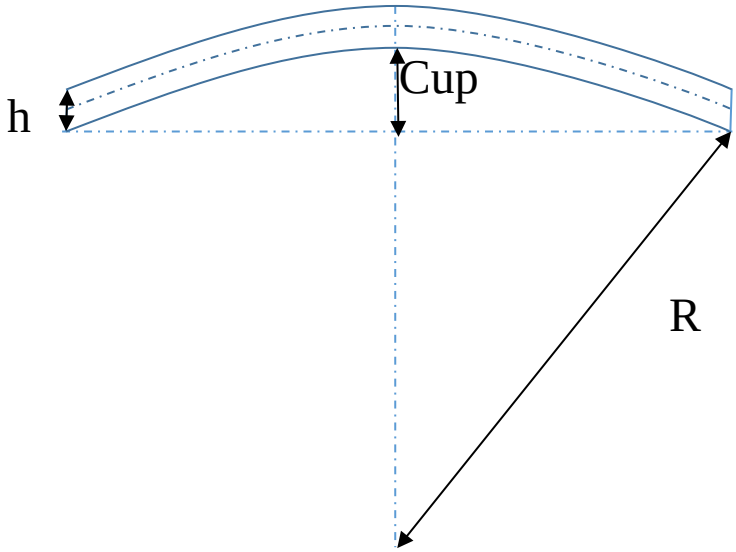

Figure 3.21. Illustration of the cup formation calculation: h is the thickness of the panel, R is the radius of the bottom surface.

The cup formation in solid southern pine with the same moisture profile was also calculated by the model to give a comparison between CLT and solid wood. cup_{xz} and cup_{yz} were determined to be 0.075 mm and 2.792 mm, respectively. It is very obvious that the cup_{yz} of solid southern pine is about 4 times larger than that of southern pine CLT. This is because there is no mechanical constraint in solid southern pine for transverse swelling. The cup_{xz} of solid southern pine is smaller than that of southern pine CLT, because there is no additional warping caused by the transverse swelling of the middle layer in CLT.

Internal stresses in southern pine CLT were calculated, using hygrothermal warping model, along the thickness of each sample, as shown in Figure 3.22 and 3.23. Steady-state internal stresses along the x-direction are given in Figure 3.22. Since the longitudinal direction of the top and bottom layers was along the x-direction, the free expansions (swelling) in this direction of these two layers were much lower than that of the middle layer. Therefore, the top and bottom layer were under tension, while the middle layer was under compression. Meanwhile, the bottom surface of the middle layer was subjected to a larger moisture content change than its top surface, hence the compression at its bottom surface was greater than that at its top surface.

Steady-state internal stresses along the y-direction are presented in Figure 3.23. Scenarios here were the opposite of those in the previous figure. The transverse direction of top and bottom layers was along the y-direction, therefore it tended to expand more in this direction of these two layers than that of the middle layer. As a result, the top and bottom layer were under compression, while the middle layer was under tension. Similarly, the bottom surface of the middle layer was subjected to a larger moisture content change than its top surface, hence the tension at its bottom surface was greater than that at its top surface.

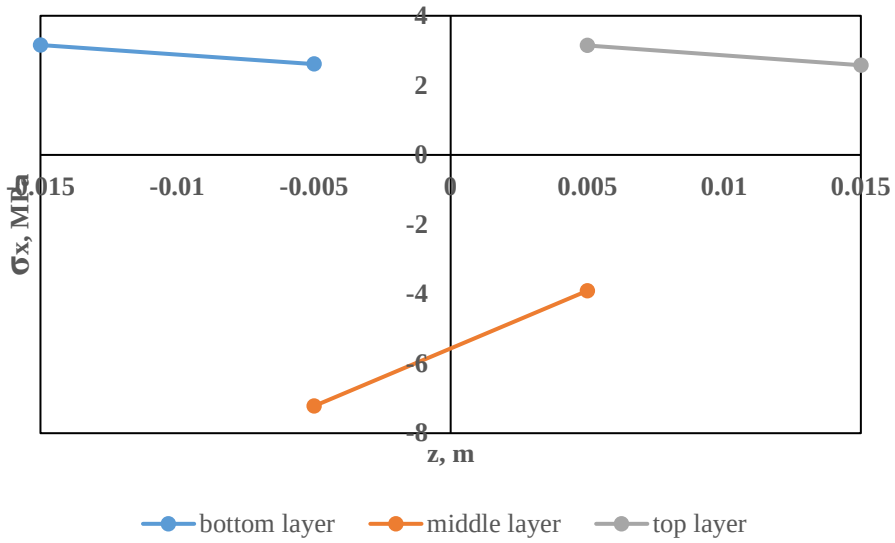

Figure 3.22. Steady-state internal stresses along the x-direction, σ_x, where z coordinate is in the z-direction. The negative sign of stresses represents compression, while the positive sign represents tension.

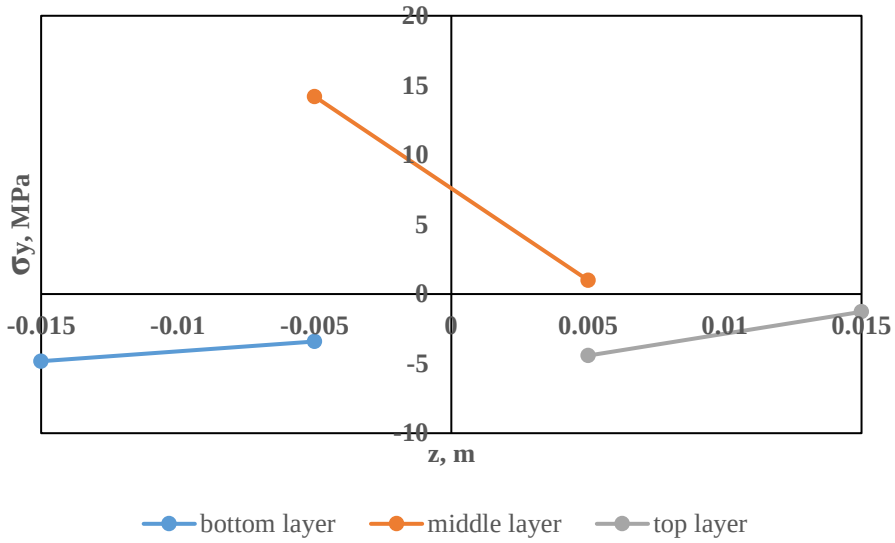

Figure 3.23. Steady-state internal stresses along the y-direction, σ_y, where z coordinate is in the z-direction. The negative sign of stresses represents compression, while the positive sign represents tension.

5. Conclusions

Warping measurements using ARAMIS Adjustable were carried out to study the deformation of southern pine cross-laminated timber when subjected to a moisture gradient. Three types of adhesives were used to prepare samples: polyurethane (PU), phenol resorcinol formaldehyde (PRF) and melamine formaldehyde (MF). Hygrothermal modeling was used to predict the deformation and compare with the measurement. It can be concluded from the results that:

- Aramis Adjustable can offer sufficient resolution to warping measurement.
- The proposed model gives a good estimation of the deformation of southern pine CLT when subjected to a 65%/100% relative humidity gradient. It also revealed that the cross lamination method improves dimensional stability as compared to solid wood.
- Adhesive types present no or little effect on the warping of CLT.

CHAPTER 4. FIRE PERFORMANCE OF SOUTHERN PINE CROSS-LAMINATED

Since it is made from a combustible material, there is concern regarding the fire safety of cross-laminated timber. Therefore in this chapter, to improve the fire performance of southern pine CLTs, factors such as adhesive types, face gluing and edge gluing are analyzed by means of fire tests and thermal analyses.

1. Literature Review

1.1. Charring of Wood

One of the biggest challenges of wood utilization in construction use is fire safety, which is determined by the charring rate of wood. The charring rate of wood generally refers to the dimensional rate, in inches per hour, at which wood converts to char (White & Nordheim, 1992). It is widely accepted that char does not have any strength or stiffness, therefore charring rate has been the topic of interest to many structural designers in order to estimate the loss of load-carrying capacity over time of wooden products.

When exposed to fire, wood undergoes thermal degradation as illustrated in Figure 4.1.

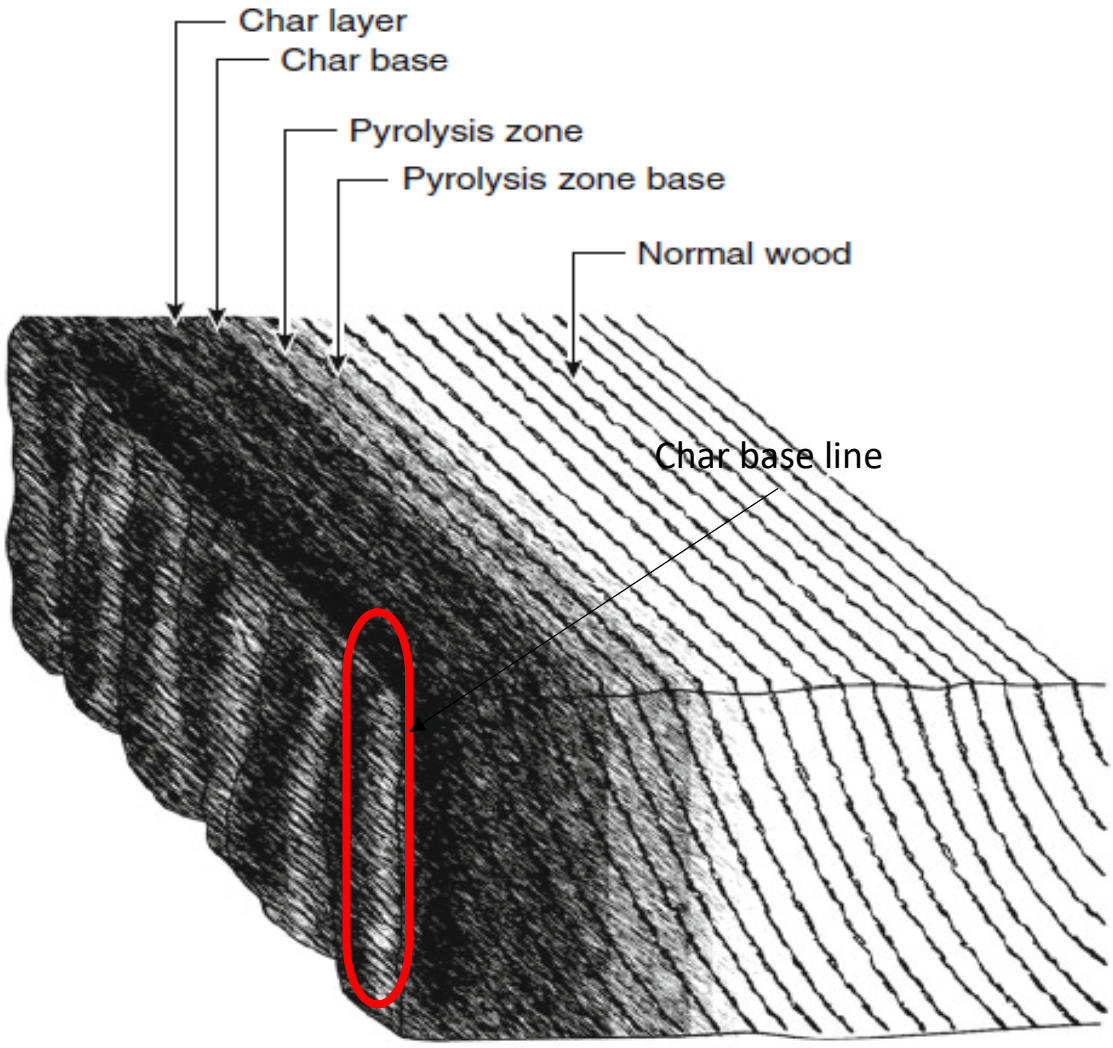

Figure 4.1. Degradation of wood under fire, showing the gradation of layers from the char layer to normal wood (White, 2016).

The **char** forms a layer of insulation on the exposed surface of wood and increases the thermal resistance between the exposed surface and the pyrolysis front, causing a decreasing heat release rate after the first peak charring rate (the first inflection point on the char depth versus time curve). There is a distinct demarcation (a black line as shown in Figure) between the charred and uncharred wood. The location of the char base is generally considered to be the position of the 300 ℃ isotherm, which is a widely accepted rounded value and close to 288 ℃

which is used in North America (Cachim and Franssen, 2009; Friquin et al, 2010; Konig, 2005; White, 2016).

Pyrolysis is the process where the extreme temperature created by the fire results in the decomposition of wood components to a mixture of tar, volatiles and highly reactive carbonaceous char. The gas phase oxidation of the volatiles and tar causes flaming combustion, while the solid phase oxidation of the remaining char produces smoldering or glowing combustion (Friquin, 2011).

As specified in EN 5 (EN, 1995), the **charring rate** (β) is assumed to be constant with the value of 0.65 mm/min for most woods. Therefore the char depth of the wood at a given time can be calculated by:

$$d_{char} = \beta t \tag{1}$$

where d_{char} is the char depth; β is the charring rate; t is the time.

However, charring rate in reality varies with and depends on many factors such as wood species, density, permeability, moisture content and chemical composition. To obtain the charring rate data, numerous studies have been conducted using exposure condition (prescribed time/temperature curve) specified in ASTM E119 (ASTM, 2011) or ISO 834 (International Organization for Standardization, 2000).

Lawson et al.(1951) studied the charring rate of Douglas fir for up to 29 minutes by using a test procedure similar to ISO 834 and found a slightly nonlinear result:

$$\beta_t = \frac{1.04}{t^{0.2}} \tag{2}$$

where β_t is the instantaneous charring rate; t is the time. From this, the test-average charring rate can be determined by:

$$\beta = \frac{1.30}{t^{0.2}} \tag{3}$$

They found that the average charring rate was 0.635 mm/min for Douglas fir.

White and Nordheim (1992) conducted forty ASTM E119 fire tests to understand the dependence of charring rates on variables such as wood species, density, permeability and chemical composition. Three levels of moisture content were used in their experiment: 6, 9 and 11 percent. They found that a nonlinear time-location model, similar to Lawson et al. (1951), reflects more accurately the location of char base at a given time than a simple linear model does:

$$t = mx^{1.23} \tag{4}$$

where t is the time for thermocouple to reach 288 ℃, x is the char depth; m is the char rate coefficient; the power 1.23 is a fitted value and has no specific interpretation. They also found that the two most important properties in the charring rate of wood are density and moisture content.

More recently, Frangi and Fontana (2003) conducted test on spruce beams for 30-110 minutes exposure time in an ISO 834 furnace and found a charring rate of 0.7 mm/min when the remaining section thickness is greater than 50 mm, while for the case of less than 50 mm, the rate increases according to the following equation:

$$\beta = 2.36 - 0.033w \tag{5}$$

where w is the remaining section thickness. They found no effect of density (over the range of 340-500 kg/m^3) and moisture content (over the range of 8-15%) on the charring rate.

In the US CLT Handbook, a non-linear charring rate model is adopted to calculate the fire resistance rating (Erol Karacabeyli, 2013):

$$t_{300℃} = \left(\frac{x}{\beta}\right)^{1.23} \quad (6)$$

where $t_{300\,℃}$ is the time it takes to reach 300 $℃$ (a generally accepted indicator of the char layer base), x is the depth in inches, β is the charring rate in inches/hour.

Since the nominal charring rate, β_n, is based on one-hour exposure time, the char slope, m, can therefore be determined by substituting Equation (4) into (6):

$$m = \frac{1}{\beta_n^{1.23}} \quad (7)$$

where β_n is in inches/hour.

1.2. Thermal Analysis

Adhesives have been widely used in wood products to bond pieces together. Under fire or elevated temperature conditions, thermal degradation can take place not only in the wood pieces, but also in the adhesives along the gluelines. To better understand the fire performance of wood products, it is of vital importance to do thermal analyses of adhesives. Techniques like thermogravimetric analysis (TGA) and differential scanning calorimetry (DSC) were used in this work to study the thermal degradation of selected adhesives. A brief introduction of these techniques is provided below.

Thermogravimetric Analysis (TGA):

Thermogravimetric analysis is a thermal analysis method in which mass changes of materials are measured as a function of time (isothermal), or as a function of elevating temperature (with a constant heating rate). TGA is commonly performed to analyze properties of materials that have mass loss or gain due to, for example, loss of volatiles, oxidation and decomposition. It can provide not only physical phenomena information like vaporization, sublimation and desorption, but also information regarding chemical properties (such as dehydration, decomposition, oxidation and so on) (Coats and Redfern, 1963; Pielichowski and Njuguna, 2005).

Through the programmable furnace, TGA can continuously weigh the sample while it is heated up to 2000 °C. It can also be coupled with Fourier transform infrared spectroscopy (FTIR) and mass spectrometry for gas composition analysis. As various physical and chemical properties are changed during the heating process, the resulting mass changes are recorded correspondingly. Mass changes are plotted on the y-axis and temperature on the x-axis. First derivatives of mass changes are often added to the plot to provide more in-depth information. A typical TGA thermogram can have a horizontal portion, which indicates no weight change; a sloping portion with the slope indicating the rate of weight loss; and an inflection, which could be two consecutive or overlapping reactions.

Differential Scanning Calorimetry (DSC):

Differential scanning calorimetry is a method of thermal analysis in which the difference of heat needed to change the temperature of the sample and the reference is recorded as a function of temperature. The temperatures of both the sample and reference are kept nearly equal

throughout the test. The basic principle of DSC is that a physical transformation such as phase change in the sample will need more or less heat input than the reference to keep them at the same temperature. There are two types of processes: endothermic and exothermic. When it is an endothermic process, for example vaporization or sublimation, the sample will absorb heat and therefore will need more heat input than the reference. On the other hand, if it is an exothermic process, such as crystallization, the sample will need less heat input. This difference in heat flow between the sample and the reference is very useful in understanding the phase changes during the process (Menczel et al., 2009).

1.3. Effect of Adhesives on Charring Rates

The use of adhesives in wood products is very common. Since wood adhesives are designed for specific uses, there is a wide variety of adhesives available in the commercial market with different properties including thermal properties such as thermal degradation temperature and glass transition temperature. At high temperature conditions such as fire, the increased vibration and mobility of the adhesive polymer cause it to be less resistant to internal or external forces, and the extent of the effect depends on its structure. For instance, crystalline segments can resist the temperature until the melting point is reached. Crosslinks and even non-covalent crosslinks (for example, hydrogen bonds) could limit the effect of elevated temperatures and make the polymer more resistant to softening. Another important aspect at high temperature is the induced interface stress if there exist significant thermal expansion coefficient differences between wood and adhesive. In this project, we studied the thermal properties of three commercial adhesive groups: polyurethane (PU), melamine formaldehyde (MF) and phenol resorcinol formaldehyde (PRF).

PUs are generally used in coatings, but can also be used for wood bonding. The most common way to form polyurethane is by reaction of di- or poly-isocyanate with polyol as shown in Figure 4.2. Depending on the specific application, PUs can be either one-component or two-component systems.

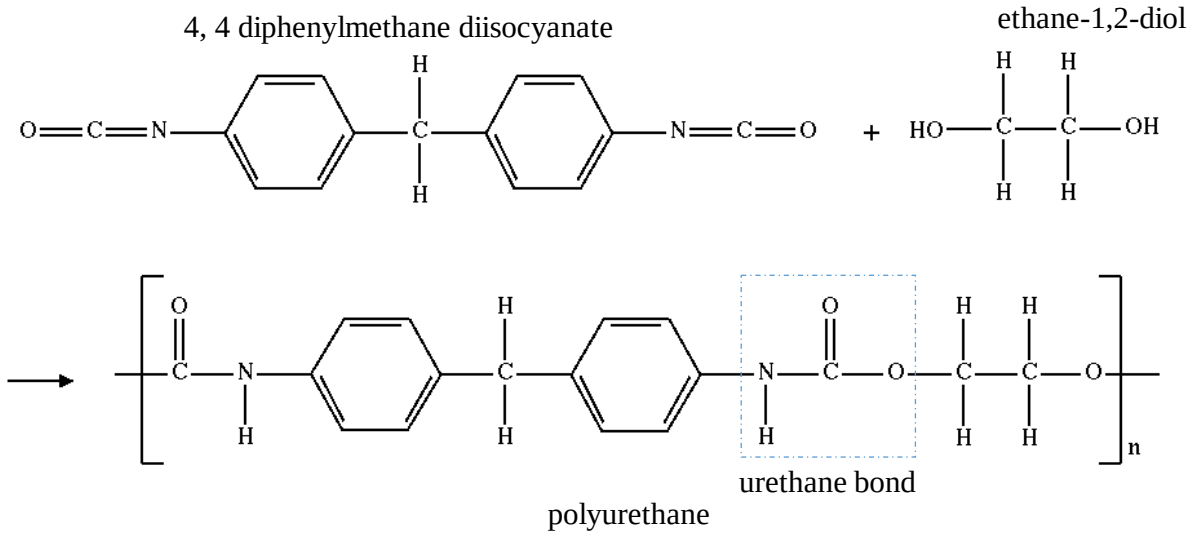

Figure 4.2. Synthesis of polyurethane from 4, 4 diphenylmethane diisocyanate and ethane-1,2-diol.

They have good strength, impact resistance and other advantages. However, the low molecular-weight isocyanate components can be volatile and thus cause health issues (Frihart, 2005). Under heating conditions, the thermal degradation of PU adhesives generally involves the breaking of urethane bonds (-NH-CO-O-) in the 200 to 350 °C range, and the decomposition of ester groups at temperatures above 350 °C (Cangemi et al., 2006; Trovati et al., 2010).

With the aim of lowering cost (compared to resorcinol formaldehyde, RF) but maintaining room-temperature-curing properties (compared to phenol formaldehyde, PF), PRF was developed and is widely used in finger jointing and laminates. The formation mechanism behaves more like RFs than PFs. Therefore, the formation of RF polymer is used here to illustrate the mechanism: 1. Addition step to form hydroxymethyl group, shown in Figure 4.3; 2.

Condensation (or partial polymerization) to form oligomers; 3. Polymerization to form a crosslinked network after applying to the substrate.

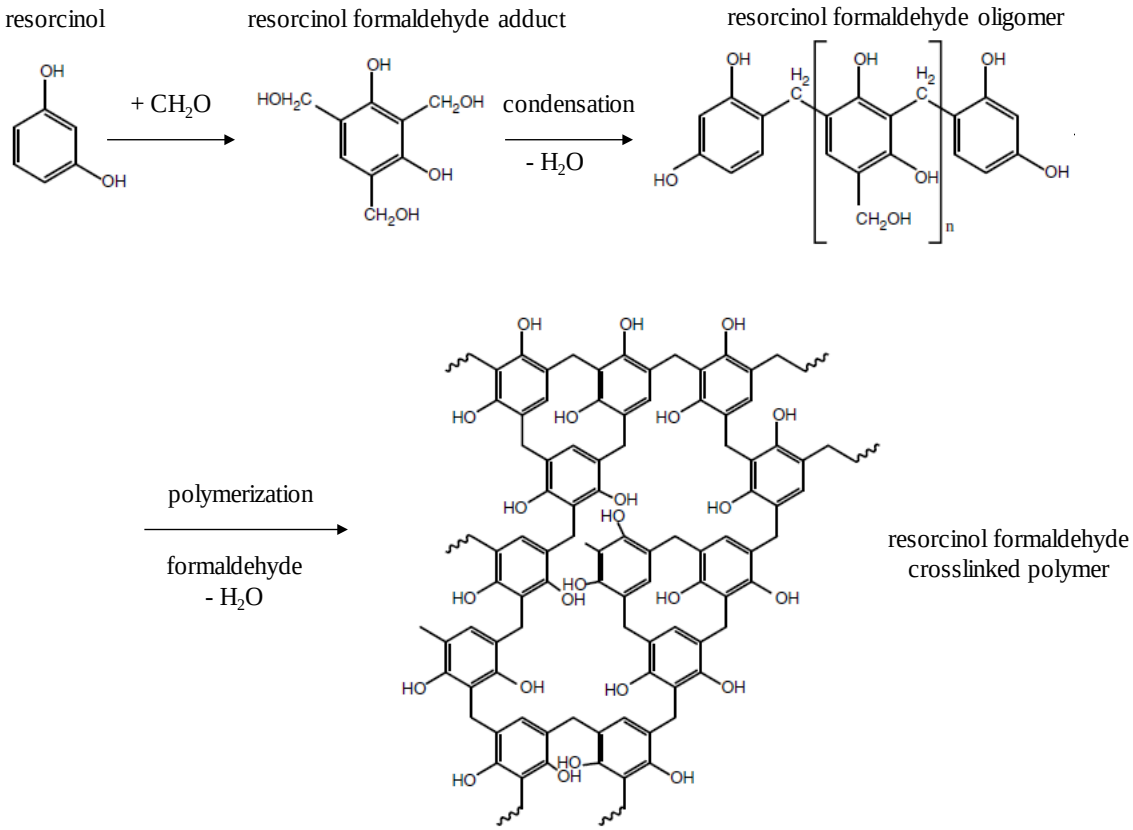

Figure 4.3. Synthesis mechanism of RF polymers from resorcinol and formaldehyde.

PRF has dark color, high bond failure resistance and degradation resistance. The assembly time is usually long due to the room temperature curing. This curing condition could avoid heating up the laminae, which is a desirable property especially when the laminae are large. However, it also results in a long processing time (Frihart, 2005).

Thermal studies have shown that PRFs generally undergo three stages during degradation. The first stage, which is below 300 °C, is attributed to removal of the free water, moisture and other volatile contents like free formaldehyde and phenol produced by the condensation reaction of hydroxyl functional groups (Lee et al., 2012). The second stage occurs in the range of 300 °C to 450 °C, which involves water loss from condensation between phenolic

hydroxyl group and methylene and between the two hydroxyl function groups (Lee et al., 2012). The third stage, occurring above 450 °C, is the main degradation stage and involves pyrolytic reactions; when the temperature exceeds 600 °C, dehydrogenation of the benzene ring occurs (Liu et al., 1995).

Unlike PRFs, which have dark color, MFs are lighter in color. The synthesis of melamine formaldehyde resins generally follows two steps: 1, the addition of formaldehyde to melamine (since melamine is a good nucleophile, it can react with up to 6 formaldehyde groups); 2, condensation and polymerization of melamine formaldehyde. Two types of reaction can occur in the condensation process:

- Reaction of two hydroxymethyl groups to form bismethylene ether:

  $\mathrm{RCH_2OH} + \mathrm{R'CH_2OH} \rightarrow \mathrm{RCH_2OCH_2R'} + \mathrm{H_2O}.$
- Reaction of hydroxymethyl group with the amine group to form methylene bridge:

  $\mathrm{RNH_2} + \mathrm{R'CH_2OH} \rightarrow \mathrm{RHNCH_2R'} + \mathrm{H_2O}.$

  A simplified illustration of this process is shown in Figure 4.4.

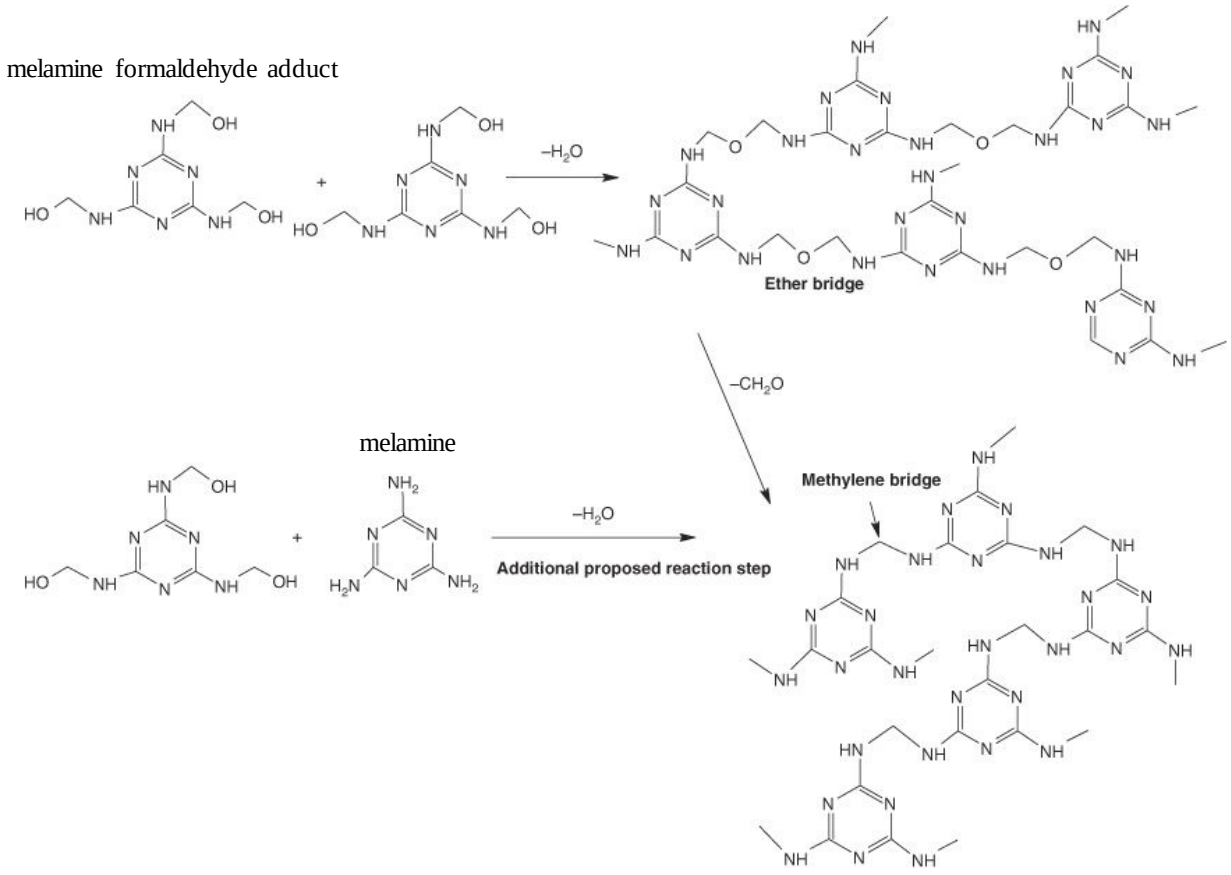

Figure 4.4. Simplified reaction for melamine formaldehyde resin synthesis from melamine and formaldehyde (Merline et al., 2012).

MFs have acceptable water resistance due to the condensation reaction to form oligomers and polymers which is not very reversible. They are generally used for semi-exterior and exterior particleboard and plywood, and also for finger jointing (Frihart, 2005). At elevated temperatures, studies have shown that below 125 °C, weight loss of MF resin is primarily due to water evaporation (Ullah et al., 2014). As the temperature keeps increasing to around 400 °C, products like formaldehyde, methanol and amine from degradations of both side-chain and ring are formed and released (Costa and Camino, 1988). After 400 °C, it's assumed that cyameluric structures are formed gradually. Finally, volatile products are produced by extensive degradation at temperature above 660 °C (Devallencourt et al., 1995).

Some early tests (Schaffer, 1968) were conducted by using a simplified method to study the effect of six different adhesives (phenol-resorcinol; polyvinyl; urea; melamine; 60 percent melamine-40 percent urea by weight, mechanically mixed; and casein) on charring. In that work, it was shown that at the bond line beneath the char layer, phenol-resorcinol adhesive and melamine adhesive had no delamination, while the polyvinyl adhesive showed delamination.

Fire behavior of cross-laminated timber was studied experimentally and numerically in Switzerland and Italy by using polyurethane as the adhesive. The results of finite element-thermal analysis showed that when the protective charcoal layer fell off after each layer was completely charred, the number and thickness of the single plies had a strong influence on the fire behavior of CLT. This was verified by carrying out ISO fire tests in a horizontal furnace at the Swiss Federal Laboratories for Materials Testing and Research (EMPA) to compare the charring rates of solid timber panels, 3×18mm thick CLT panels, and 3×9mm thick CLT panels. The charring rates of the solid timber panels were the lowest, those of the 3×9mm thick CLT panels were the highest. Another group of fire tests carried out at EMPA's and CNR-IVALSA's vertical furnaces suggested that due to a less pronounced falling of the charcoal layer, vertical structural members may exhibit a better fire performance as compared to horizontal ones. It was also mentioned that the adhesive behavior at high temperature could play an important role in the multilayer timber panel fire behavior evaluations (Frangi et al., 2008; Frangi et al., 2009b). Later, in a study of the fire performance of loaded CLT wall elements, it was found that abrupt changes of CLT's load-bearing performance may occur due to the layered structure (Schmid et al., 2015).

Due to the inherent nature of thick timber members to char slowly at a predictable rate, CLT products have the potential to provide excellent fire performance comparable to typical non-combustible building materials (Karacebeyli and Douglas, 2013). Several studies have

focused on the **fire resistance** performance of the CLT structure, including the effect of **adhesive types** (Fragiacomo et al., 2013; Frangi et al., 2012; Schmid et al., 2010). This is mainly in response to the need to accelerate the approval of product standards and the inclusion of **CLT in building codes**. Hasburgh et al. (2016) showed that early smoke penetration could occur when there is a small, open path for air to pass through. This suggested that filling the gaps, for example by means of edge gluing, could prevent early smoke penetration and thus further improve the fire performance of CLT panels. There have not been studies of the effect of **edge gluing** on the fire performance of CLT panels.

1.4. Southern Pine

Southern (yellow) pine generally refers to the four species (shortleaf pine, slash pine, longleaf pine and loblolly pine) growing in the southern United States. They all share similar characteristics, for instance, high density and an abrupt transition from earlywood to latewood. Given its high density and strength properties, southern pine is ideal for general construction. It can be used for home construction, furniture, timber framing and so on.

Historically, longleaf pine was the industry favorite and utilized in almost all structural applications. However, it ran out in around 1900's and has not been commonly available since then. The fast growing loblolly pine is the favorite in industry now. Loblolly pine is one of the most common species in United States, making the access widespread and the price competitive. In the meantime, to be consistent with previous studies of cross-laminated timber, 3-layer **southern pine** (loblolly pine) cross-laminated timber was chosen in this research to study the fire performance.

2. Problem Statement and Objectives

The fire safety of CLT panels in construction is of vital importance as demanded by regulations. There have been numerous studies on this subject, and several models have been developed to predict its fire performance. However, early smoke penetration could occur when there are open paths for air, and solutions have not been investigated. Therefore edge-gluing with three commercially available adhesives (PU, PRF and MF) is proposed in this study with the aim of overcoming the problem. The null hypothesis is that edge-gluing has no effect on the fire performance (characterized by charring rate) of cross-laminated timber.

The overall goal of this research is to study the fire performance of 3-layer **southern pine** cross-laminated panels manufactured by different gluing methods. By comparing charring rate, the specific objectives are to:

- Determine the effect of edge gluing on CLT panel fire performance.
- Evaluate the fire performance of different adhesives (polyurethane, phenol resorcinol formaldehyde, and melamine formaldehyde) used to glue the CLT panels.

3. Materials and Methods

In order to evaluate the influence of adhesive type and edge gluing on the fire performance of CLT panels, a small-scale fire test was performed first using a Bunsen burner (Schaffer, 1968). Three commonly used adhesives were tested: phenol resorcinol formaldehyde (PRF: Adhesive LT5210J and Hardener FM6310J from Hexion Inc.), polyurethane (PU: Gorilla Glue manufactured by the Gorilla Glue Company) and melamine formaldehyde (MF: Adhesive C1263 and Hardener C9563 from AkzoNobel). Thermogravimetric analysis (TGA) and differential scanning calorimetry (DSC) of adhesives were conducted as well to analyze the thermal properties of these adhesives. Based on the small-scale test results and previous unpublished studies, a total of nine southern pine CLT panels were tested in a horizontal fire-resistance furnace with two factors (edge adhesive and face adhesive) and with no replicates (

Table 4.12). The southern yellow pine lumber used in this project was purchased from a local supplier in Raleigh, North Carolina. The samples were flatsawn, with specific gravity around 0.51, moisture content of 12%, and grade stamp of NO. 2.

Table 4.12. List of intermediate-scale fire test specimens: two-factor (edge adhesive and face adhesive) with no replicates.

Specimen No.	Specimen Label	Edge Adhesive	Face Adhesive
1	MFE-MFF	MF	MF
2	PRFE-MFF	PRF	MF
3	PUE-MFF	PU	MF
4	MFE-PRFF	MF	PRF
5	PRFE-PRFF	PRF	PRF
6	PUE-PRFF	PU	PRF
7	MFE-PUF	MF	PU
8	PRFE-PUF	PRF	PU
9	PUE-PUF	PU	PU

3.1. Small-Scale Fire Test

The sample preparation and test procedure for the small-scale fire test is illustrated in Figure 4.5. Southern yellow pine lumber with dimensions of 1 in × 5 ½ in × 12 in (thickness×width×length) were conditioned at 20 ℃, 65% relative humidity (RH) until equilibrium, then glued together to make two 4-layer panels for each adhesive (PU, PRF and MF) with dimensions of 4 in × 5 ½ in × 12 in (thickness×width×length). The gluing specifications are listed in Table 4.13, following the general guidelines provided by the glue manufacturers.

Table 4.13. Gluing specifications for the small-scale fire test samples.

Adhesive	Glue spread (g/m^2)	Glueline pressure (psi)	Pressing time (hrs)
MF	0.260	140	2
PRF	0.189	150	7
PU	0.129	100	4

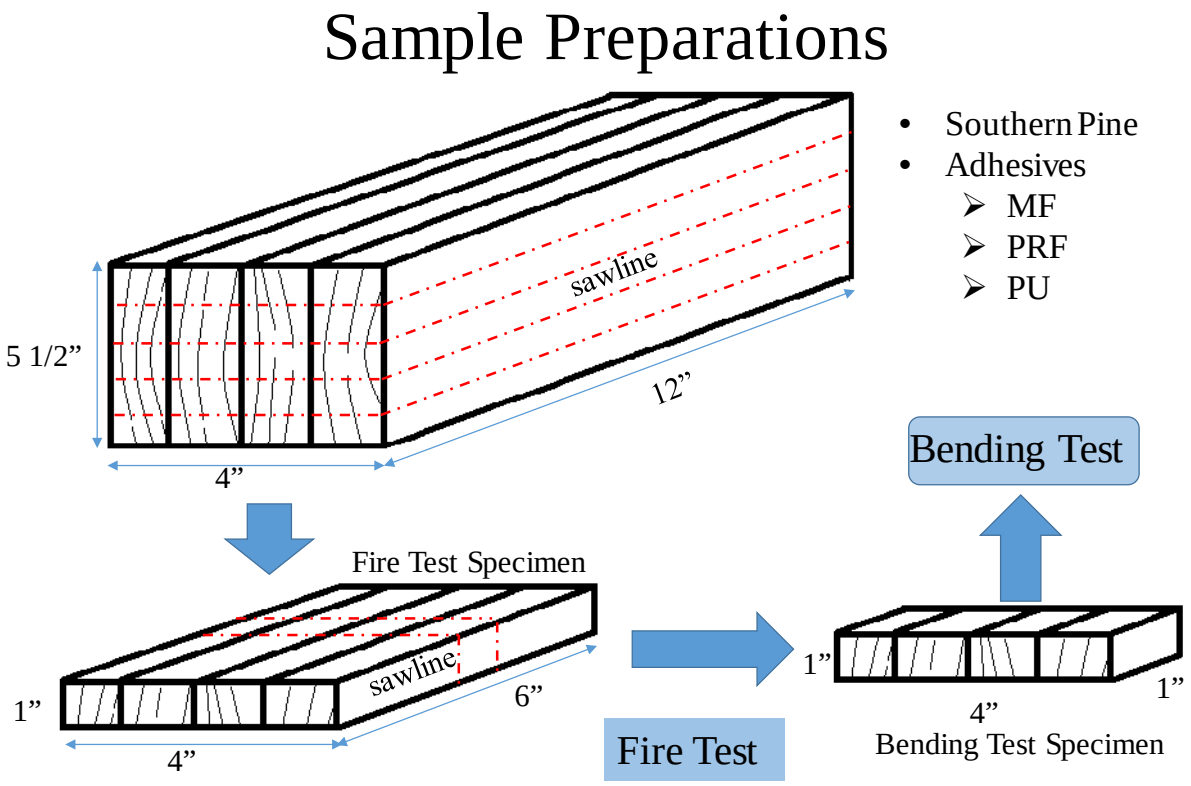

Figure 4.5. Sample preparation and test procedure for the small-scale fire test: Step 1, prepare two glued panels with dimensions of 4 in × 5 ½ in × 12 in (thickness×width×length) for each adhesive; Step 2, cut three pieces (1 in × 4 in × 12 in) from the middle of each panel, then cut in half to obtain two end-matched specimens (one for control, the other for the fire test); Step 3, perform fire tests on the test group specimens.

Once cured, three pieces (1 in × 4 in × 12 in) were cut from the middle of each panel, then cut in half to obtain two end-matched specimens: one for control, the other for the fire test (labeling of test group specimens are shown in

Table 4.14). A fire test was performed by subjecting the specimen to a flame (800 to 900 ^{o}C) from a Bunsen burner for 5 minutes, then rotating the specimen 180^{o} and continuing for another 5 minutes. The test setup is shown in Figure 4.6. After the fire test, a 1 in × 1 in ×4 in

specimen was cut from the center for char depth measurement and static bending test (4 inches span, 2 inches/minute test rate on MTS, Alliance RF/300).

Figure 4.6. Small-scale fire test setup (specimen subjected to flame from a Bunser burner, courtesy of Bryan Dick).

Table 4.14. Labeling of specimens for the small-scale fire test: M, P, G stands for MF-, PRF- and PU-glued specimen, respectively; M11 to M13 stand for specimens cut from the first MF-glued block, M21 to M23 stand for those coming from the other MF-glued block. The same labeling rule works for the other two adhesives groups.

Adhesive	Specimen Label	
MF	M11	M21
	M12	M22
	M13	M23
PRF	P11	P21
	P12	P22
	P13	P23
PU	G11	G21
	G12	G22
	G13	G23

3.2. Thermogravimetric Analysis and Differential Scanning Calorimetry of Adhesives

Thermal studies of adhesives were performed using thermogravimetric analysis (TA Instruments, TGA Q500) and differential scanning calorimetry (TA Instruments, DSC Q100). Adhesive samples were prepared in the form of film by applying adhesive to a flat and easy to peel surface according the manufacturer's or distributor's instruction. After preparation, the samples were stored and conditioned in a climate chamber (20 °C, 65% RH) until equilibrium. Then, samples (at least two replicas for each adhesive type) were taken to the thermal analysis laboratory to conduct TGA and DSC tests.

The TGA tests were carried out over the temperature range of 50~800 °C with a ramping rate of 10.00 °C/min under nitrogen atmosphere and sample size around 10 mg. Two cycles of DSC tests were performed for each specimen over the range of 40~200 °C with a ramping rate of

10.00 °C/min and sample size around 10 mg. The TGA and DSC protocols are provided in the Appendix.

3.3. Intermediate-scale Horizontal Fire Test (ASTM E119)

With the aim to determine the fire performance of CLT panels, a test procedure based on ASTM E119 (ASTM, 2011) was performed. Due to the limitations in the lab, the specimens used were smaller than the specified dimension in the standard. The specimens tested were 3-layer southern pine CLT panels with the dimension of 3.75 in × 40 in ×30 in (thickness×length×width) manufactured in the Hodges Wood Products Laboratory at North Carolina State University. Once lumber was bought from local distributor, it was planed, ripped, and trimmed close to but larger than the desired dimension (in order to have a fresh surface for adhesive application). Then it was conditioned at 20 ℃, 65% relative humidity (RH) until equilibrium. Thereafter, lumber pieces were ripped first and then edge glued by a James L Taylor Clamp Carrier. Once cured, each edge-glued ply was planed to a thickness of 1.25 inches using a Newman-Whitney S-480 Single Planer. Then three plies were face-glued into a CLT using a steam-heated hydraulic press. The gluing specifications for both edge-gluing and face-gluing were the same as those for the small-scale fire test sample as listed in Table 4.13. In total 9 specimens were then shipped to the US Forest Product Laboratory (FPL) in Madison, WI where they were conditioned (at 23 ℃, 50% RH for at least 30 days) and subjected to fire test. Prior to the fire test, the edges of each specimen were covered with 0.5 inch thick ceramic wool insulation as illustrated in Figure 4.7.

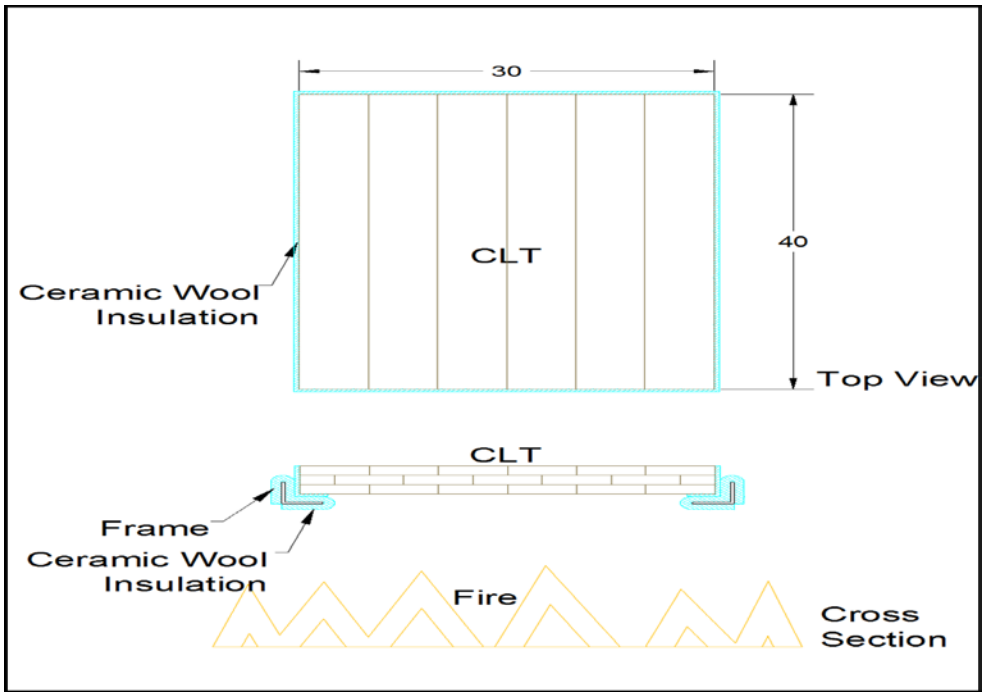

Figure 4.7. Illustration of specimen preparation prior to fire test (Courtesy of Forest Product Laboratory).

A temperature of 300 ℃ was used as an indicator of the char layer base. Thermocouples (30 gauge, Type K glass insulated thermocouple wires) were utilized to monitor the progression of char layer in the CLT panels. Through holes drilled from the non-exposed surfaces, the thermocouples were located at and halfway between the glue lines. Thermocouples were also attached on the fire-exposed and the non-exposed faces. Illustration of the thermocouple locations in the specimen can be found in Figure 4.8 and Table 4.15. Expanding fire-stop putty (McMaster-Carr part number: 9340K23) was used to seal the thermocouple holes and prevent smoke or other gases from flowing through.

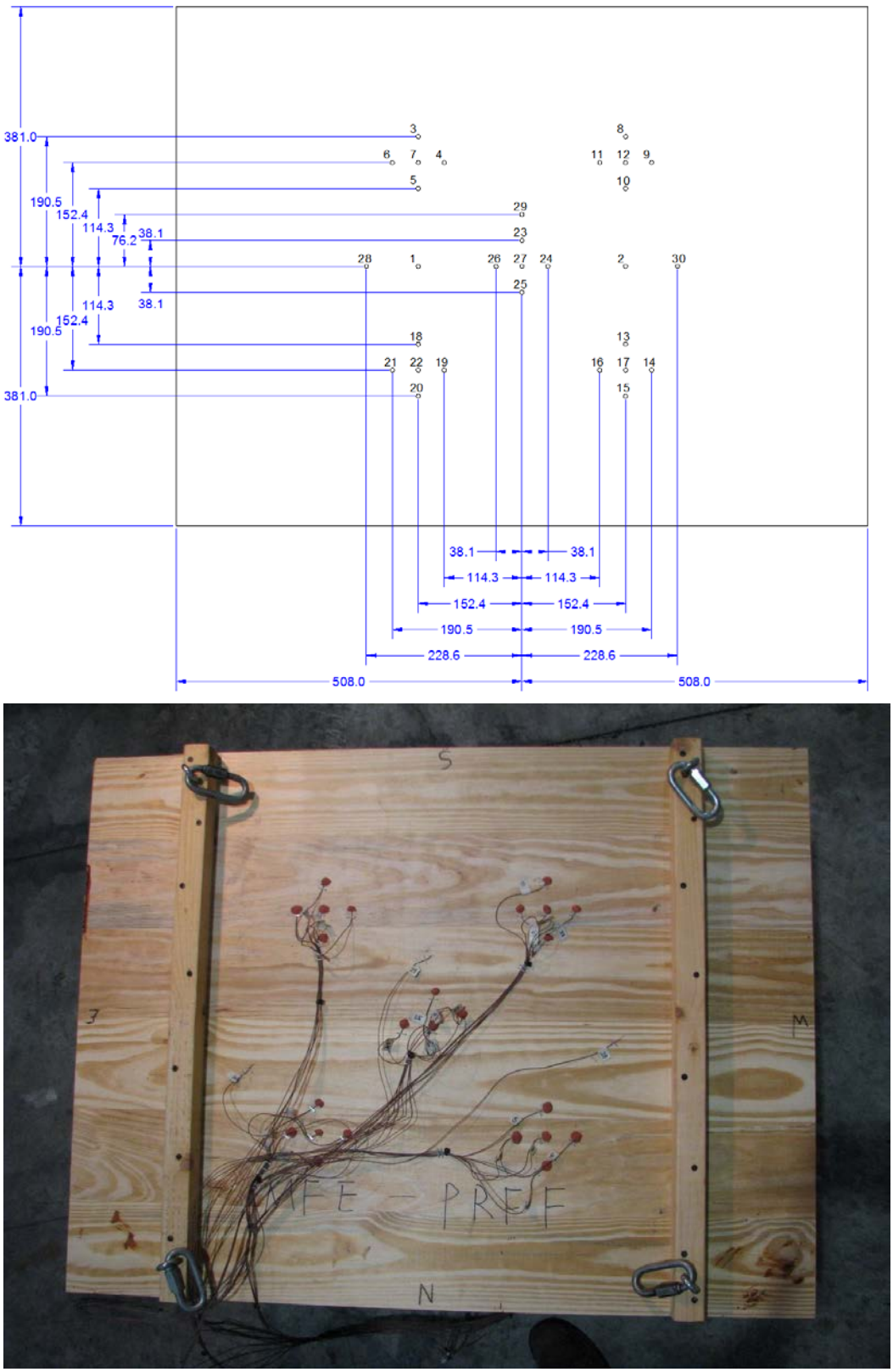

Figure 4.8. Location of thermocouples on the non-exposed surface of the CLT. Dimensions are in mm. (Courtesy of Forest Product Laboratory).

Table 4.15. Locations of thermocouples in the CLT thickness direction.

Thermocouple No.	Dist. From Exposed Surface (mm)	Drill Depth from Unexposed Surface (mm)
1,2	0	
3,8,13,18,23	16	80
4,9,14,19,24	32	64
5,10,15,20,25	48	48
6,11,16,21,26	64	32
7,12,17,22,27	80	16
28,29,30	94	

After conditioning, the specimens were tested in the FPL intermediate-scale horizontal furnace (Figure 4.9). No load was applied to the specimen. Temperature data for the furnace and the specimens were recorded every five seconds. Tests were terminated when thermocouples at the second glueline from the exposed surface reached around 300 ℃ or until flame-through (the time at which the first visible flames passed through the unexposed surface).

Figure 4.9. Intermediate-scale horizontal furnace (Left) and specimen frame (Right) (Courtesy of Forest Product Laboratory).

4. Results and Discussion

4.1. Small-Scale Fire Test

Specimen thicknesses and weights were recorded before the small-scale fire test. Then char depth (from the originally exposed surface to the char base), pyrolysis depth (from the char base to the pyrolysis base) and separation depth (from the char base to the end of separation along the glueline) were measured after the fire test as shown in

Figure . Separation depth can also be verified after the bending test, as shown in Figure . Weight loss associated with the fire test, along with all thickness data, are presented in

Figure 4.11. Side views of small-scale fire test specimen after static bending test (G, P and M stand for PU, PRF and MF respectively).In this figure, it also shows the measurement of char depth (from the exposed surface before fire test to the char base), pyrolysis depth (from char base to pyrolysis base) and separation depth (from char base to the end of glue line separation).

Table 4.16. Bartlett’s Test was first performed to evaluate the homogeneity of variance. Given the confidence level of 95% (unless otherwise mentioned, this value was chosen throughout the paper), as shown in

Table 4.17, the equal variance hypothesis for each variable can not be rejected. Thereafter one-way ANOVA and Duncan's multiple-range test were adopted to analyze the effect of adhesive on different means. Table 4.18 shows that weight losses were similar for all specimens, with an average value of around 19.0 g. This was also true when it came to char depth and pyrolysis depth: differences were not significant, with average value of 7.1 mm and 2.5 mm respectively for all specimens. This agrees well with expectation. Despite being glued with different adhesives, the specimens had the same dimensions and were made from the same batch of southern yellow pine lumber with the same grade. Therefore, under the simplified fire test condition, specimens behaved similarly to solid wood sample (average charring rates are 0.71mm/min and 0.65mm/min for glued specimens and solid wood, respectively).

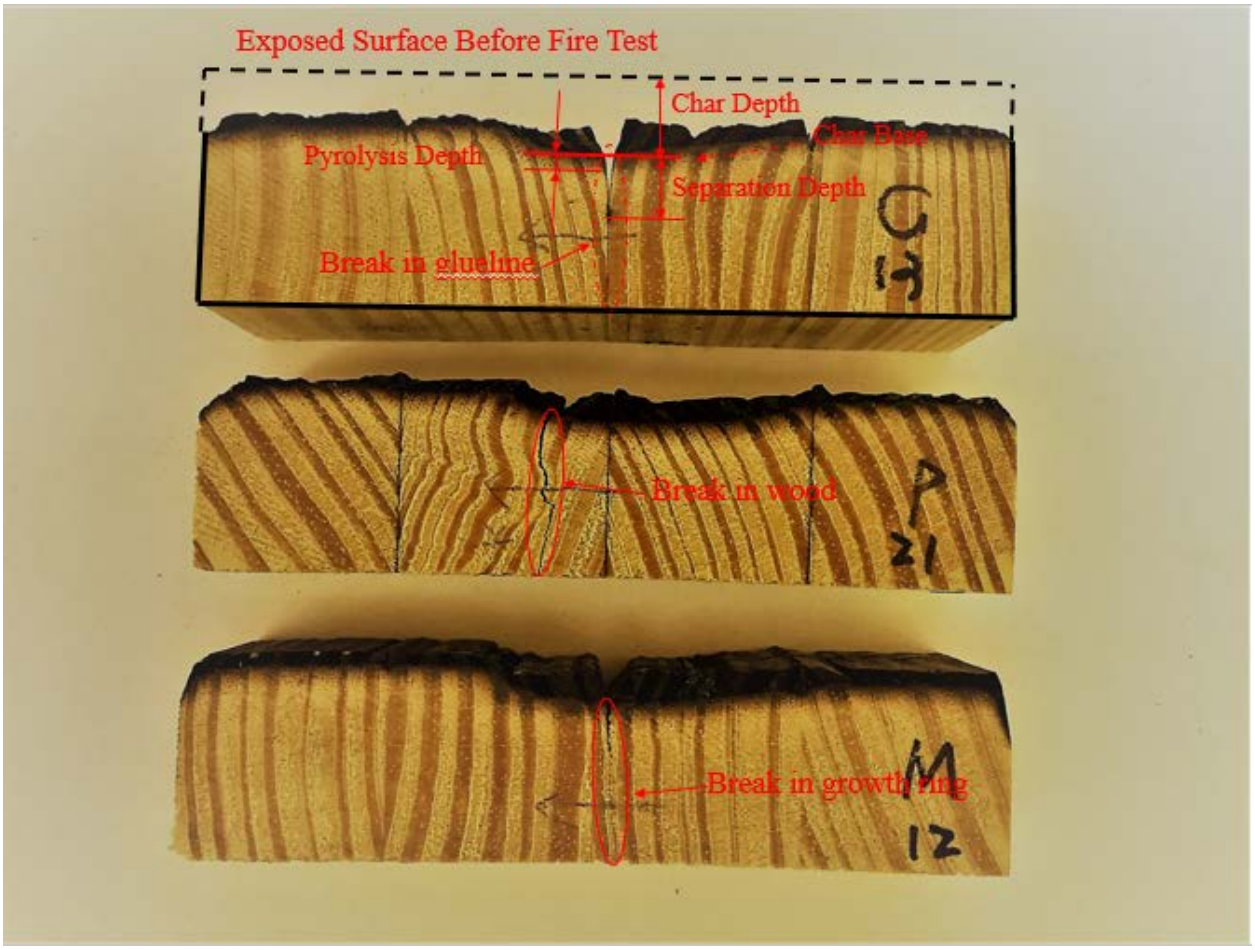

Figure 4.10. Specimens (G, P and M stand for PU, PRF and MF respectively) after the small-scale fire test and bending test. The figure also shows the measurement of char depth (from the exposed surface before fire test to the char base), pyrolysis depth (from char base to pyrolysis base) and separation depth (from char base to the end of glue line separation).

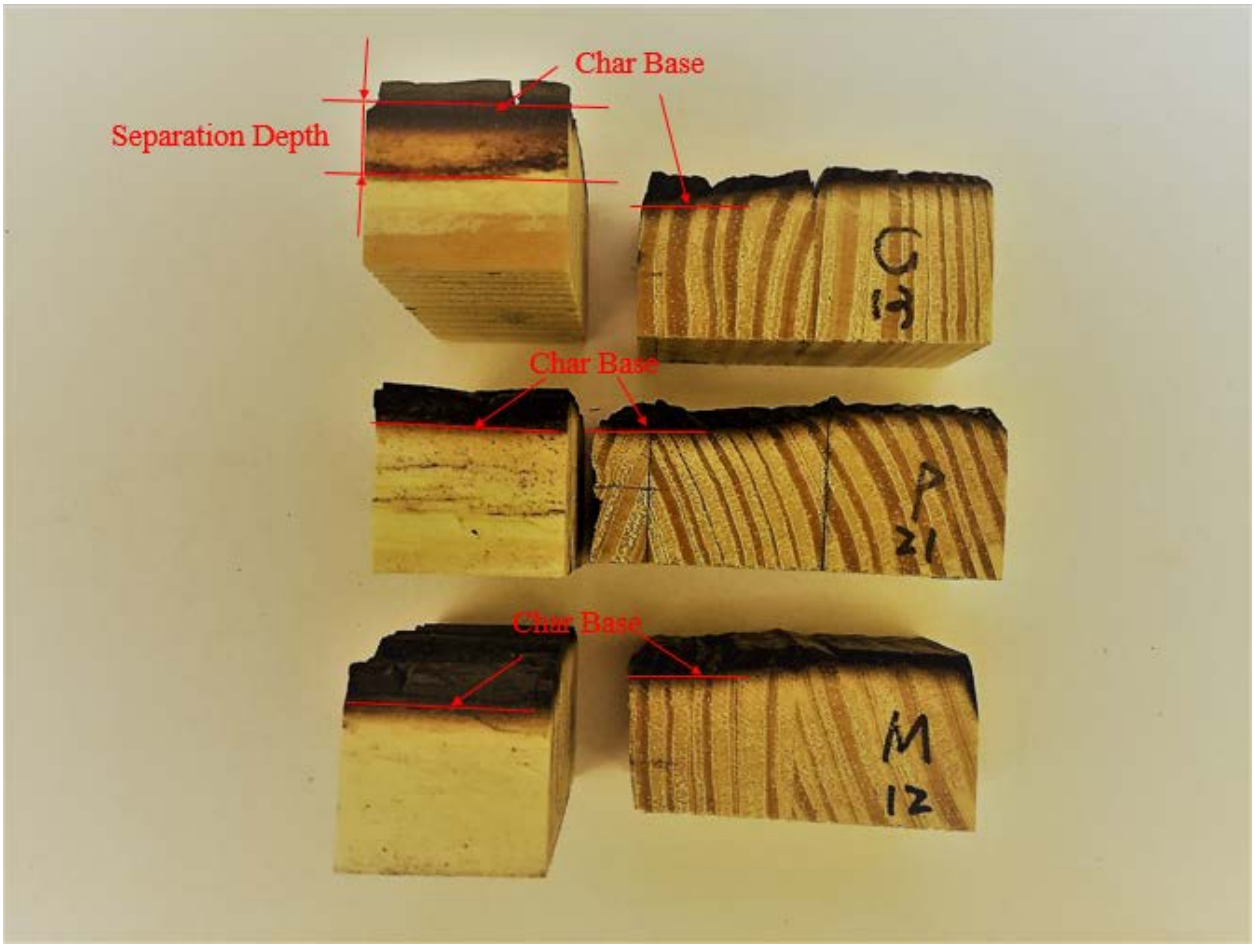

Figure 4.11. Side views of small-scale fire test specimen after static bending test (G, P and M stand for PU, PRF and MF respectively).In this figure, it also shows the measurement of char depth (from the exposed surface before fire test to the char base), pyrolysis depth (from char base to pyrolysis base) and separation depth (from char base to the end of glue line separation).

Table 4.16. Results for the small-scale fire test including weight loss, separation depth, char depth and pyrolysis depth.

Sample ID	Weight Loss (g)	Weight Loss(%)	Panel Thickness (mm)	Separation depth (mm)	Char Depth (mm)	Pyrolysis Depth (mm)
PRF11	20.1	7.6	26.6		6.6	2.6
PRF12	20.7	8.3	27.4		7.4	2.6
PRF13	19.6	7.7	27.9		7.9	2.6
PRF21	19.9	7.5	27.1		6.9	2.4
PRF22	18.0	6.8	27.1		7.1	2.3
PRF23	18.5	6.8	28.0		7.5	2.6
PU11	19.0	7.1	27.2	6.0	6.7	2.5
PU12	17.9	7.0	26.9	5.0	6.9	2.6
PU13	19.4	7.6	26.6	5.0	6.6	2.5
PU21	19.0	7.1	27.2	5.2	7.2	2.4
PU22	18.7	7.2	26.9	4.6	7.3	2.4
PU23	19.7	7.3	28.0	5.4	8.0	2.6
MF11	19.0	6.9	26.4		6.3	2.5
MF12	19.4	7.6	27.1		7.1	2.3
MF13	20.4	8.0	27.7		7.7	2.4
MF21	19.3	7.1	27.2		7.6	2.3
MF22	18.8	6.9	26.9		7.1	2.5
MF23	18.8	6.9	27.1		6.7	2.5

Notes: Separation depth is measured, only when there is glueline separation, as the distance between original exposed surface and the end of glueline separation.

Table 4.17. Bartlett's test for homogeneity of variance for weight loss, char depth and pyrolysis depth.

Weight Loss			
Source	DF	Chi-Square	Pr > ChiSq
Adhesive	2	3.6116	0.1643
Char Depth			
Source	DF	Chi-Square	Pr > ChiSq
Adhesive	2	0.0947	0.9537
Pyrolysis Depth			
Source	DF	Chi-Square	Pr > ChiSq
Adhesive	2	0.8212	0.6633

Table 4.18. ANOVA analysis results for weight loss, char depth and pyrolysis depth.

Weight Loss

Source	DF	Sum of Squares	Mean Square	F Value	Pr > F
Adhesive	2	0.20231180	0.10115590	0.54	0.5930
Error	15	2.80330819	0.18688721		
Corrected Total	17	3.00561999			

Char Depth

Source	DF	Sum of Squares	Mean Square	F Value	Pr > F
Adhesive	2	0.08361111	0.04180556	0.16	0.8520
Error	15	3.87208333	0.25813889		
Corrected Total	17	3.95569444			

Pyrolysis Depth

Source	DF	Sum of Squares	Mean Square	F Value	Pr > F
Adhesive	2	0.03444444	0.01722222	1.46	0.2629
Error	15	0.17666667	0.01177778		
Corrected Total	17	0.21111111			

Visual observations were made after each fire test. As shown in Figure 4.12, char layer delamination, quantified by separation depth (Table 4.5, Figure 4.10, and Figure 4.11), was substantial in PU (polyurethane) glued specimens, while less obvious in the other two groups. This confirmed findings from our earlier unpublished research, in which severe delamination occurred in face-glued PU samples, as illustrated in Figure 4.13. This was mainly due to the difference in performance of each adhesive under fire exposure: polyurethane exhibited less stability than did melamine formaldehyde and phenol resorcinol formaldehyde. Further studies regarding the thermal stabilities of each adhesive will be discussed later in this work.

Bending test data are summarized in

Table 4.19; statistical analysis results are presented in Table 4.9-4.11. The data show that PU-glued specimens had the highest bending strength with the mean of 1671.4 N before fire test. However, after the small scale fire test, the mean peak loads were not significantly different from each other, which means PU glue specimens lost the most strength during the fire test. This was as expected and also mainly due to thermal stability difference of adhesives, or in other words, PU was less stable under fire condition than MF and PRF.

Table 4.19. Bending test results of control group specimens (left) and fire test group specimens (right).

Specimen ID	Time to Break (S)	Peak Load (N)	Specimen ID	Time to Break (S)	Peak Load (N)
PRF11C	3.6	1662.6	PRF11	3.6	368.1
PRF12C	2.2	1188.7	PRF12	2.6	330.1
PRF13C	1.8	1172.3	PRF13	2.2	229.6
PRF21C	2.2	1075.7	PRF21	3.0	444.1
PRF22C	2.8	1223.6	PRF22	2.6	171.6
PRF23C	2.2	1407.7	PRF23	1.8	447.6
PU11C	4.0	1732.1	PU11	2.6	196.6
PU12C	3.4	1497.8	PU12	3.2	337.0
PU13C	3.8	1819.1	PU13	3.4	314.8
PU21C	3.0	1638.1	PU21	3.0	208.8
PU22C	2.8	1672.2	PU22	3.0	194.7
PU23C	2.2	1669.2	PU23	2.4	244.7
MF11C	2.0	1104.2	MF11	2.2	387.2
MF12C	2.0	996.9	MF12	3.0	119.3
MF13C	3.0	1563.6	MF13	3.2	363.2
MF21C	3.6	1686.5	MF21	3.2	411.3
MF22C	2.2	1419.4	MF22	2.4	346.5
MF23C	2.0	1336.6	MF23	2.6	492.0

Notes: 1, all sample ID with "C" at last stand for control samples; 2, PRF22 broke along the glue line; 3, MF12 broke along the growth ring.

Table 4.20. Bartlett's test for homogeneity of variance for peak load.

Peak Load for Control Group			
Source	DF	Chi-Square	Pr > ChiSq
Adhesive	2	3.3786	0.1846
Peak Load for Test Group			
Source	DF	Chi-Square	Pr > ChiSq
Adhesive	2	2.1907	0.3344

Table 4.21. ANOVA analysis results for peak load.

Peak Load For Control Group

Source	DF	Sum of Squares	Mean Square	F Value	Pr > F
Adhesive	2	506271.896	253135.948	6.00	0.0122
Error	15	632746.716	42183.114		
Corrected Total	17	1139018.612			

Peak Load For Test Group

Source	DF	Sum of Squares	Mean Square	F Value	Pr > F
Adhesive	2	36046.1188	18023.0594	1.67	0.2207
Error	15	161522.9403	10768.1960		
Corrected Total	17	197569.0591			

Table 4.22. Duncan grouping for Control Group.

Duncan Grouping	Mean	N	Adhesive
A	1671.4	6	PU
B	1351.2	6	MF
B	1288.4	6	PRF

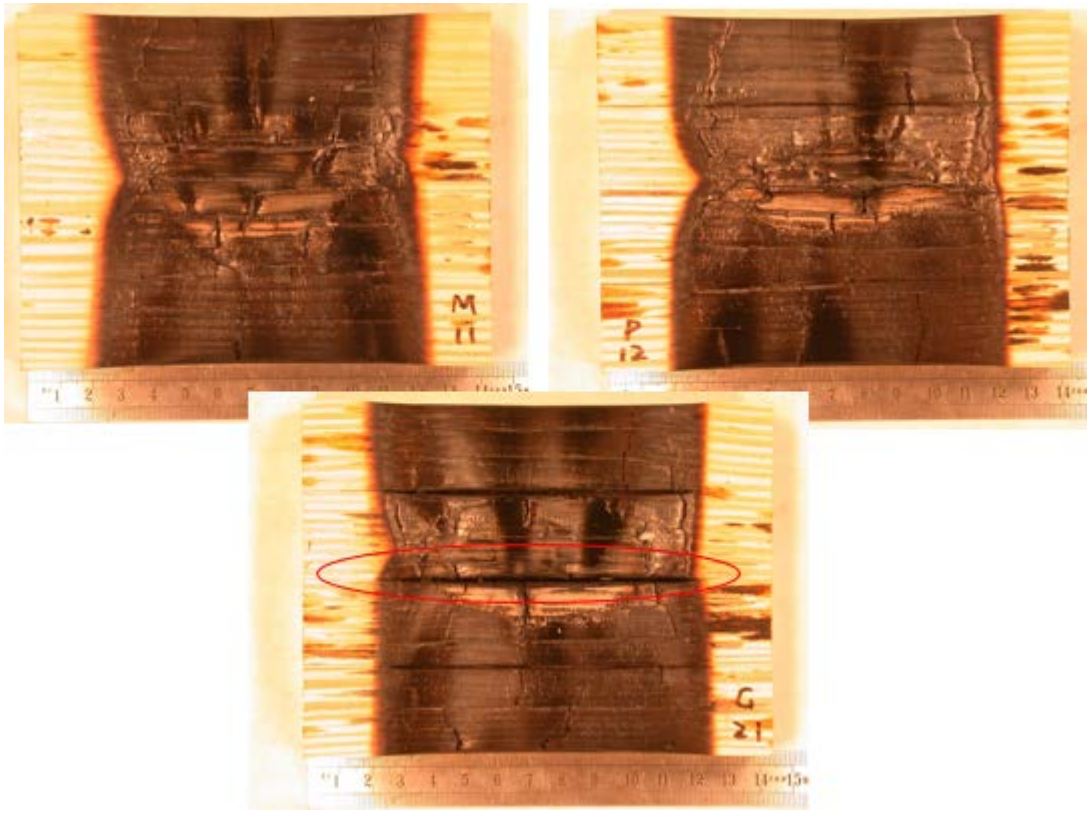

Figure 4.12. Visual observations after simplified fire test: “M”, “P” and “G” stand for MF, PRF and PU glued sample respectively.

Figure 4.13. Previous unpublished fire test results: PU glued sample (top) had severe delamination; MF (middle) had less delamination; PRF had no delamination.

4.2. Thermal Studies of Adhesives

To better understand the fire performance of CLT panels, TGA was first carried out to study the thermal stabilities of the adhesives used in this work. Figures 4.14-4.16 display the representative TGA profile of each adhesive in nitrogen atmosphere. The temperatures at 30% and 60% weight loss, and the residue percentage at 800°C are marked in each graph.

The weight loss of MF in Figure 4.14. Representative thermogravimetric analysis profile for melamine formaldehyde.

4.14 before the peak at around 180 °C was mainly due to the evaporation of water/moisture and volatile contents, which were generated during adhesive curing (Merline et al., 2013; Ullah et al., 2014). This is also confirmed by the DSC profile of MF in Figure 4.17. MF then underwent faster weight loss and had a peak differential weight loss at around 350 °C due to the formation and release of formaldehyde from the ether bridge forming methylene bridges. Weight loss from 350-390 °C may be attributed to the break of methylene bridges (Costa and Camino, 1988; Merline et al., 2013). The remaining weight at 300 °C, which is the generally-accepted char base temperature for wood, was less than 60%. Weight loss after 400 °C is an indication of further degradation. The residue at 800 °C is around 20%.

The TGA profile of PU is presented in Figure 4.15. The first small weight loss peak at around 75 °C was related to the loss of moisture and volatile contents. Then it has two distinctive weight loss peaks in the curve. The weight loss peak at 340 °C was mainly due to the breaking of urethane bonds (Cangemi et al., 2006; Trovati et al., 2010). The remaining weight at 300 °C was about 80%. The weight loss peak above 350 °C was mainly due to decomposition of ester groups (Cangemi et al., 2006; Trovati et al., 2010). The residue at 800 °C is around 25%.

PRF exhibited a much better thermal stability as than the other two shown in Figure . The weight loss before 300 °C is assumed to be due to the loss of free water, moisture and other volatile contents like free formaldehyde and phenol produced by the condensation reaction of hydroxyl functional groups (Lee et al., 2012). The second peak, which is between 300 °C to 400 °C may be attributed to water loss from condensation between phenolic hydroxyl group and methylene and between the two hydroxyl function groups (Lee et al., 2012), and the last peak which is above 450 °C involves pyrolytic reactions. At 800 °C, PRF still had more than 60% of its mass left.

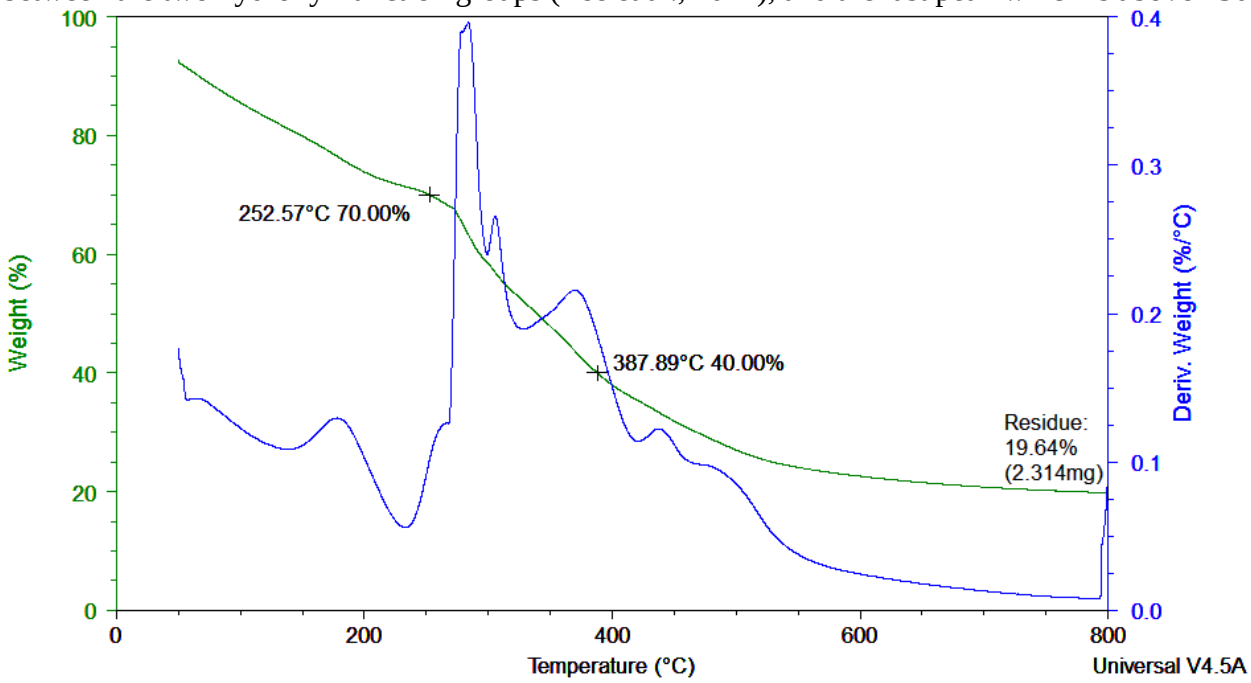

Figure 4.14. Representative thermogravimetric analysis profile for melamine formaldehyde.

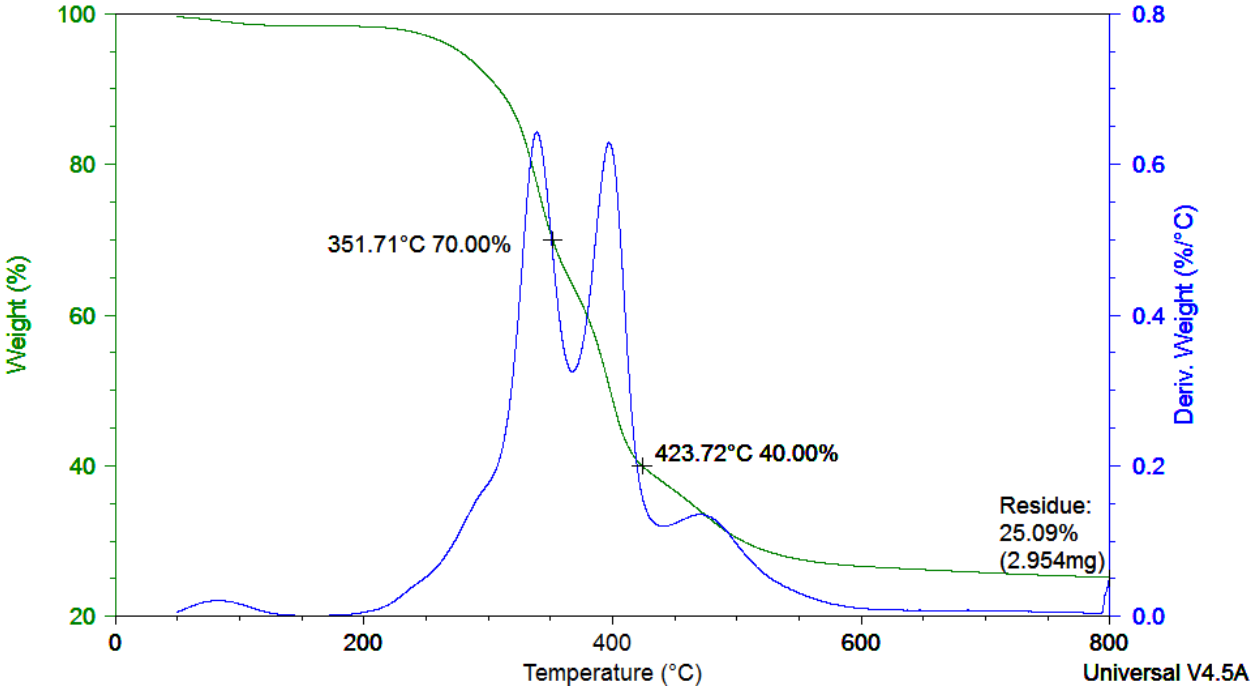

Figure 4.15. Representative thermogravimetric analysis profile for polyurethane.

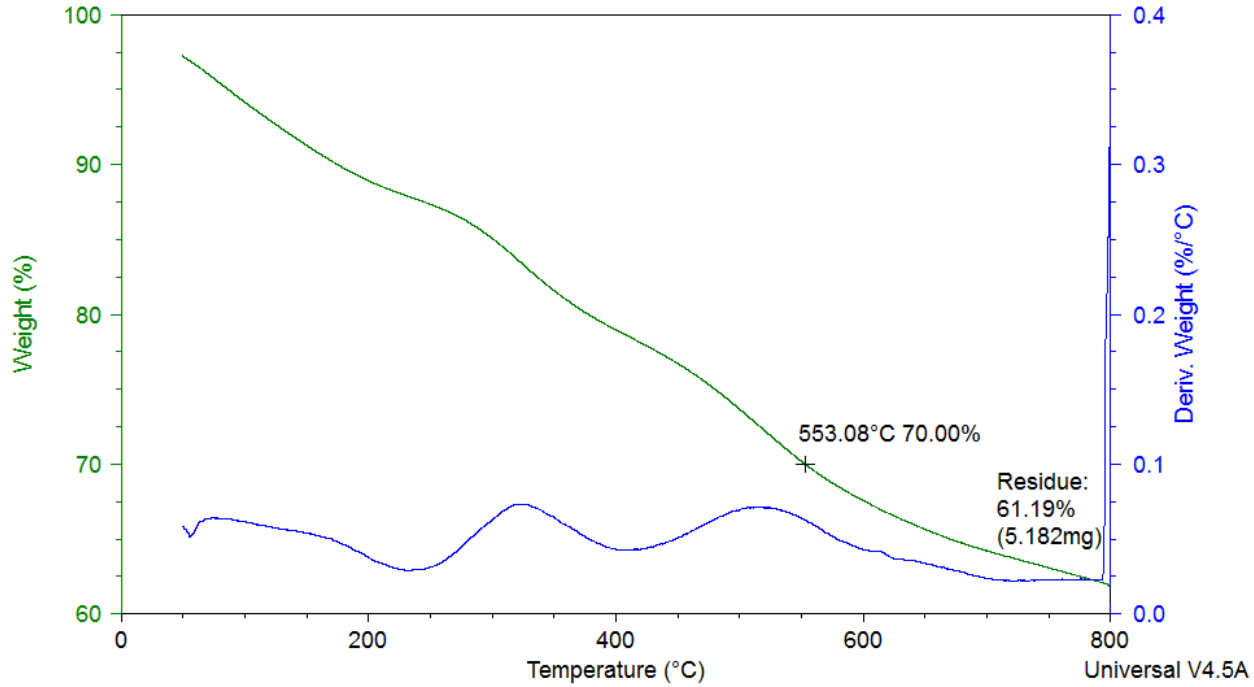

Figure 4.16. Representative thermogravimetric analysis profile for phenol-resorcinol formaldehyde.

DSC tests were conducted thereafter to further evaluate the thermal stabilities within the temperature range of 40 ~ 200 °C at a heating rate of 10 °C/min. Representative results are

presented in Figures 4.17-4.19. Although the shapes of these curves are similar, the mechanisms are different.

In Figure , the DSC profile of MF is presented. Although specimens had been cured at room temperature and conditioned in a climate chamber (20 °C, 65% RH) until equilibrium, there were still some remaining free chemicals (for instance, formaldehyde), and to some extent the curing was only partial. Therefore similar to the work done by Dyana (Dyana et al., 2013), the heating rate decreased before 140 °C due to the vaporization of moisture and volatile contents. After this, exothermal curing happened and the heating rate increased and peaked at around 180 °C. This also confirmed the peak weight loss of MF in Figure 4.14. Representative thermogravimetric analysis profile for melamine formaldehyde.

.

Similar to MF, the curing of PU specimens were conducted at room temperature following conditioning in the same climate chamber until equilibrium. The heat flow rate decreased before the peak at around 130 °C as shown in Figure 4.18. This is primarily due to the break of hydrogen bond (Seymour and Cooper, 1971) and the loss of moisture and volatile contents. Then as the temperature kept increasing, an exothermal peak occurred at around 150 °C. It was caused mainly by the incomplete cure due to room-temperature curing. (Daniel et al., 2008)

The curing and conditioning of PRF specimens were also the same as the others. As mentioned previously, the idea of adding resorcinol into phenol-formaldehyde is to cure it at room temperature. However at this condition, although the curing could reach to a high completion level, there were still partially uncured chemicals left especially from the phenol-formaldehyde portion (Chow, 1977). Therefore, besides moisture, free formaldehyde and other volatiles also existed in

the specimens. In Figure 4.19, before 135 °C, the decreasing heat flow was mainly due to the evaporation of the moisture and volatile contents. Then the heat flow increased primarily because of the curing of phenol-formaldehyde and peaked at around 150 °C. This curing-caused peak was confirmed by Charles's work (Vick and Christiansen, 2007).

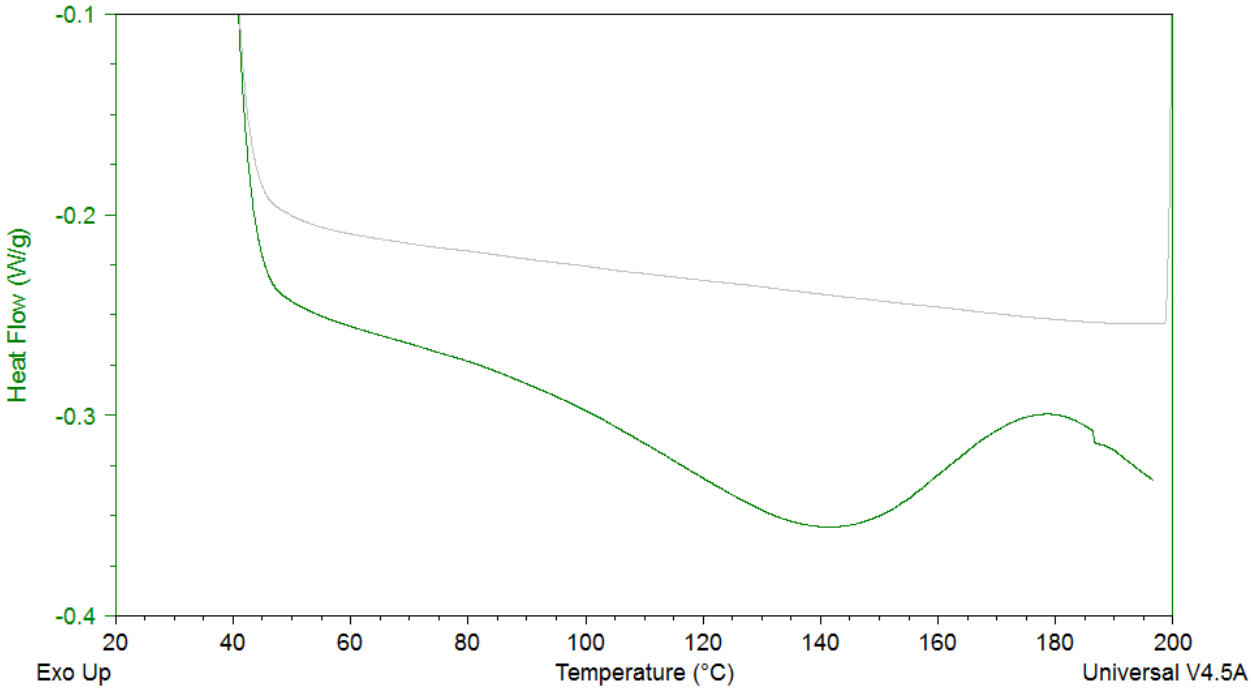

Figure 4.17. Representative differential scanning calorimetry profile for melamine formaldehyde (green line represents the first circle, gray line the second).

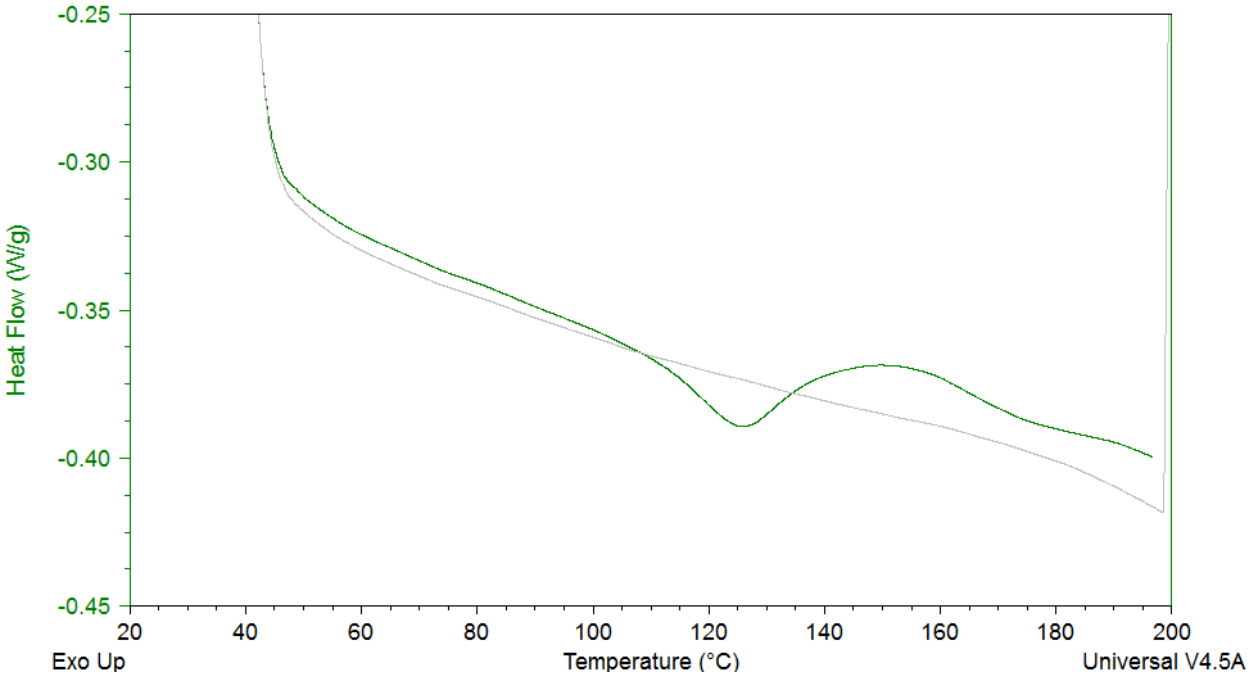

Figure 4.18. Representative differential scanning calorimetry profile for polyurethane (green line represents the first circle, gray line the second).

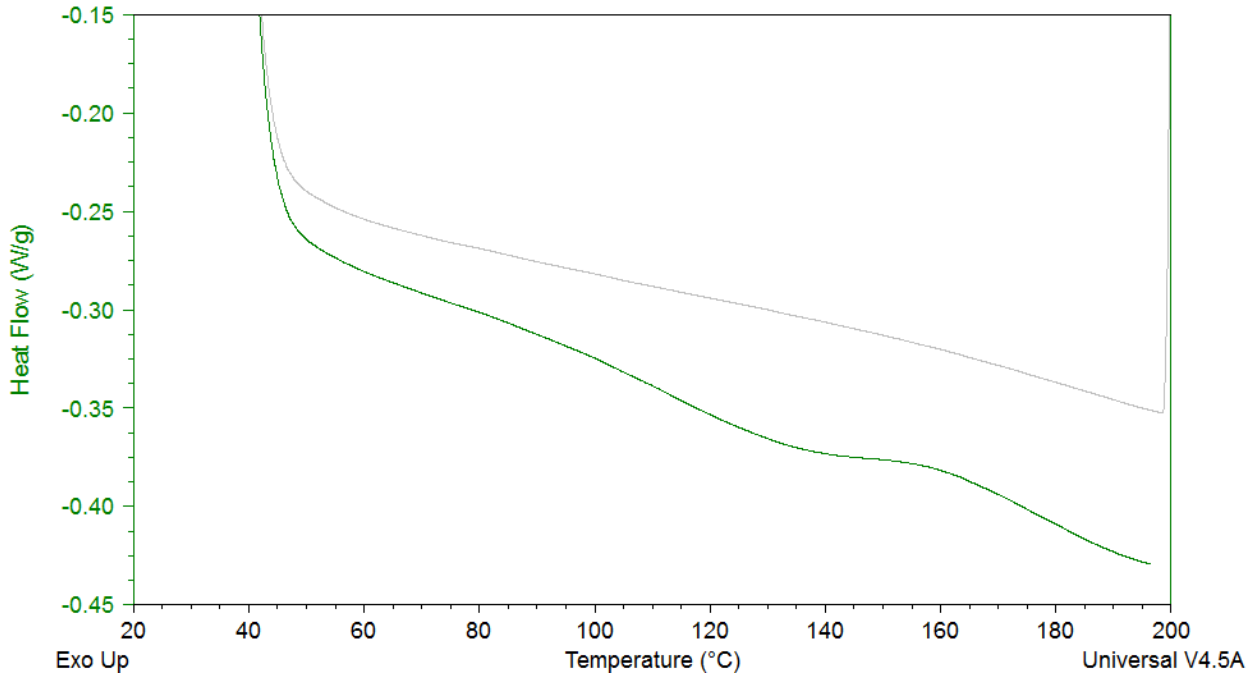

Figure 4.19. Representative differential scanning calorimetry profile for phenol resorcinol formaldehyde (green line represents the first circle, gray line the second).

4.3. Intermediate-scale CLT Fire Test

4.3.1. Furnace Operation and Conditions of Acceptance

ASTM E119 requires record of furnace temperatures at intervals of no more than 5 minutes. It also requires that deviations of average furnace temperature from the corresponding area for standard time-temperature curve be less than 10% for one hour or less, and less than 7.5% for one to two hours. The calculated deviations for all samples are listed in

Table 4.23. All deviations were within the standard requirements.

Table 4.23. Deviations of average furnace temperature from the corresponding area for standard time-temperature curve.

Specimen No.	Area under time-temperature curve above 20°C base (°C-min.) (percentage deviation from standard curve)					
	30 min.		1 hour		1.5 hours	
	area (°C-min)	% deviation	area (°C-min)	% deviation	area (°C-min)	% deviation
1	19446	-1.0	45593	-0.3	73689	-0.1
2	19526	-0.6	45697	-0.1	--	--
3	18954	-3.5	45140	-1.3	--	--
4	19461	-1.0	45598	-0.3	73645	-0.2
5	19278	-1.9	45459	-0.6	73540	-0.3
6	18925	-3.7	45062	-1.5	73118	-0.9
7	19665	0.1	45866	0.3	--	--
8	19400	-1.3	45575	-0.4	--	--
9	19442	-1.1	45507	-0.5	--	--
Standard area	19,650		45,740		73,760	

Since the test specimens were not loaded, it was decided to run the test until the first two laminae were completely charred (the point when the panel was predicted to have no remaining substantial strength). Thermocouples at the second glueline were used to determine the time of failure and the test was stopped when these thermocouples reached 300 °C. The modes of failure and time are presented in Table 4.24. The tests were continued beyond the failure points when deemed safe to obtain additional charring rate data. An example of the collected temperature data is shown in Figure 4.20.

Table 4.24. Failure mode and time of each specimen in the intermediate-scale fire test.

Specimen No.	Adhesive		Time to flame [min][1]	Time to 300°C [min][2]	Total Exposure Time [min][3]
	Edge	Face			
1	MF	MF	91	76	91
2	PRF	MF	89	--	89
3	PU	MF	--	76	81
4	MF	PRF	--	89	99
5	PRF	PRF	--	92	101
6	PU	PRF	--	93	99
7	MF	PU	85	--	86
8	PRF	PU	--	75	80
9	PU	PU	--	75	79

Notes:

1. *This is the time when flames were first observed on the unexposed side of the specimen.*
2. *This is the average time when all thermocouples at the second gluelined reached 300 °C.*
3. *This is the total time the specimen was exposed to fire.*

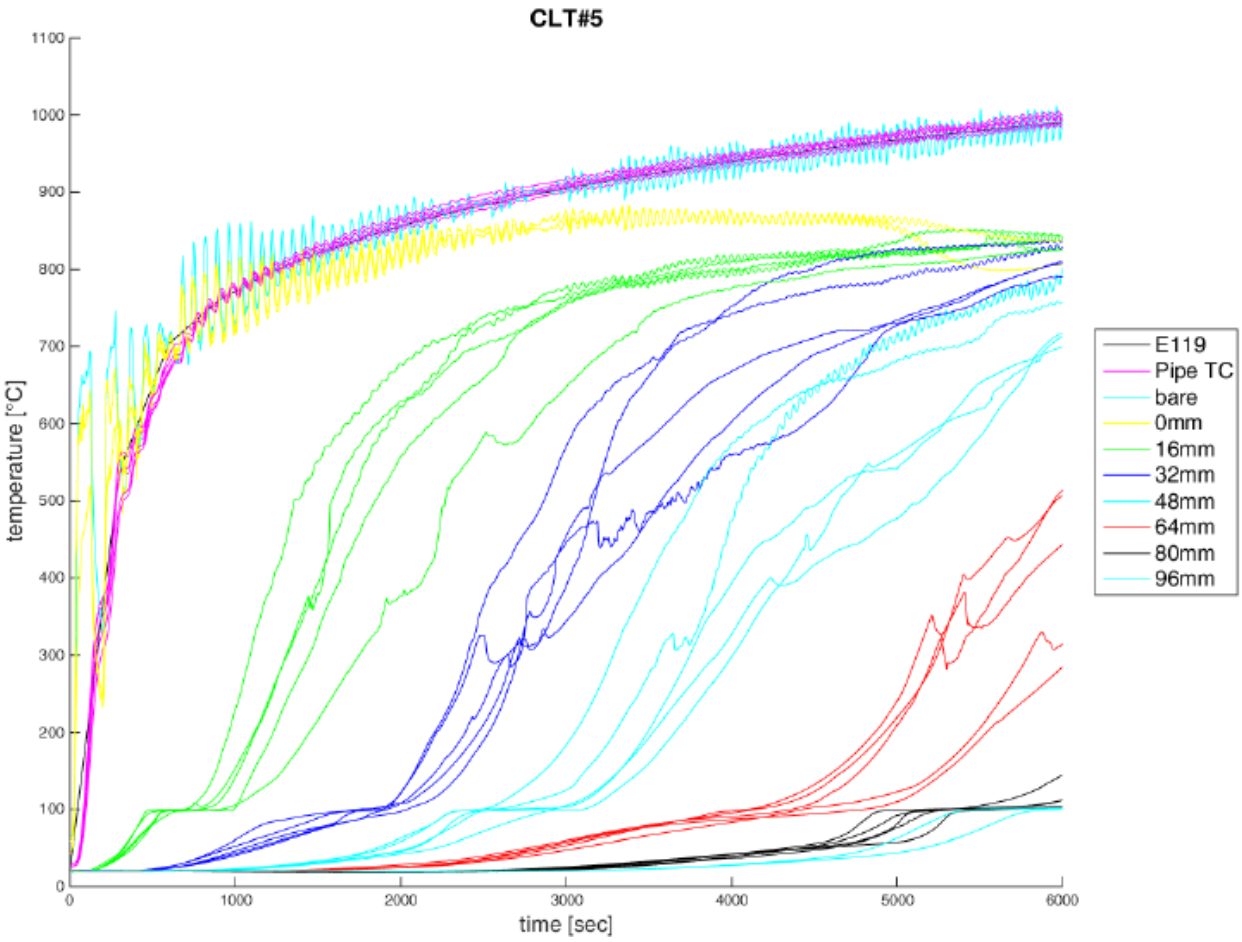

Figure 4.20. Thermocouple data for PRFE-PRFF (specimen 5).

4.3.2. Linear char rate model

Assuming a constant char rate, a linear model similar with Equation (1) can be applied to describe the charring rate of CLT panels:

$$d_{char} = \beta t + b \tag{9}$$

where d_{char} is the char depth; t is the time for each thermocouple to reach 300 °C (which is generally accepted as the base of char layer); the slope, β, is the char rate in millimeters per second or inches per hour.

By using a linear least squares algorithm, the data recorded during the fire test could be fitted to the linear model to estimate the char rate of each sample.

Table 4.25 and Figure present the fitted parameters. In this table, the charring rate of each lamina was listed. Statistical analysis results for face-gluing effect are summarized in Table 4.26-4.28. Though statistical analysis showed that first lamina charring rates of PU group were significantly different from the other two groups, the differences were not big (1.6 in/hr for PU group and 1.7 in/hr for the other two groups). This was expected since all specimens were manufactured with the same dimensions from the same batch of same grade southern yellow pine lumber. Therefore, they behaved similarly to solid soft wood under fire condition: average charring rate of first laminae is around 0.72mm/min and that of solid wood is 0.65mm/min.

However, the scenarios for the second laminae were quite different. It can be seen that for the MF and PU face-glued samples, the second lamina char rates were much higher as compared to the PRF face-glued samples, with the average char rate values of 2.07 in/hr, 2.35 in/hr and 1.51 in/hr for MF, PU and PRF respectively. This was mainly due to thermal stability differences. Based on the results from the small-scale fire test and thermal studies, PRF adhesive was most thermally stable. MF and PU had degradation temperature of around 250 °C, which is below the generally accepted 300 °C char base temperature. As a result, when the temperature of the first face glueline reached 300 °C, the previously formed char layer, which was acting as a protecting layer for the second laminate, fell off from the samples that were face-glued with MF and PU. Consequently, the char rates of the second lamina increased substantially for these two groups.

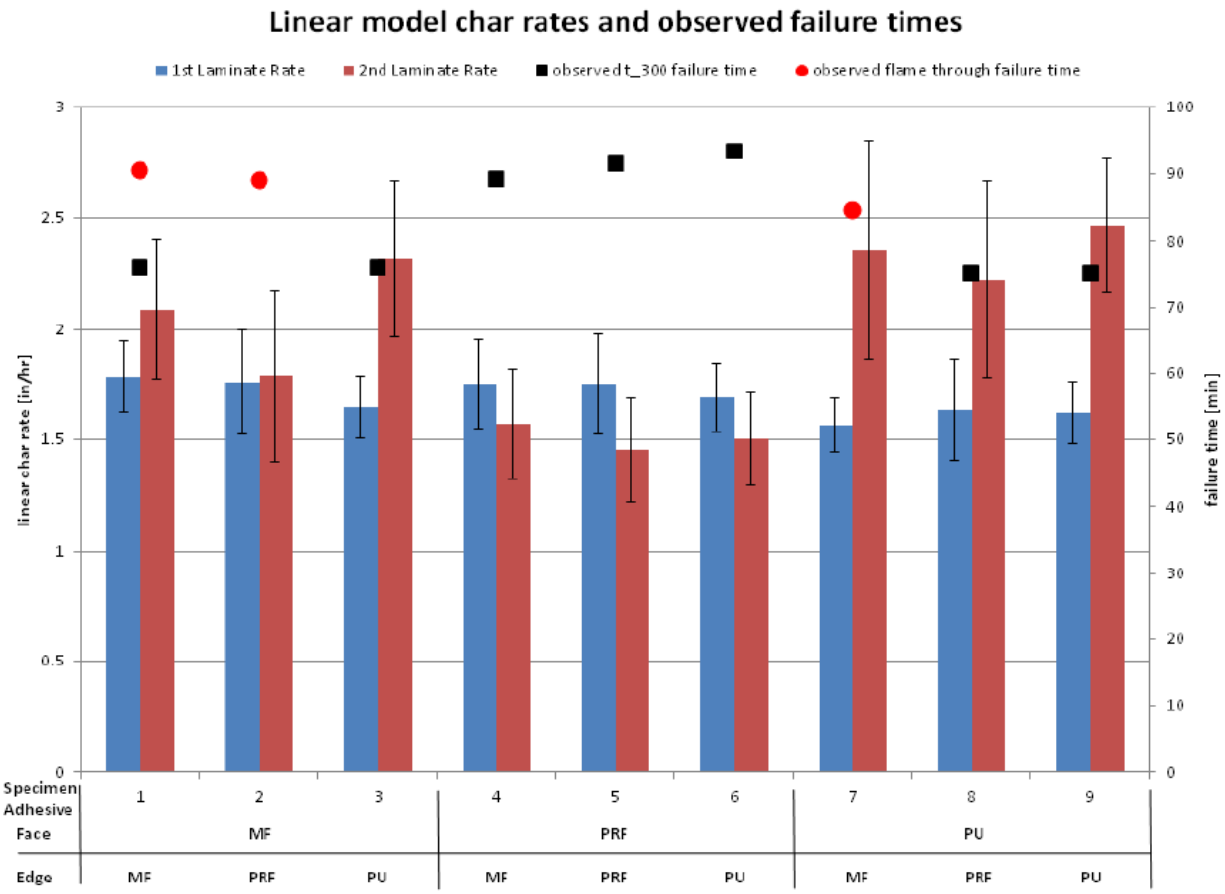

Figure 4.21. Comparison of linear charring rate (Table 4.14) and failure times (Table 4.13).

Table 4.25. Results of the regression analysis for the linear char rate model.

Specimen #	Adhesive		$d_{char} = \beta t + b$					
	Face	Edge	1st Lamina			2nd Lamina		
			β (in/hr)	95% ci	b (in)	β (in/hr)	95% ci	b (in)
1	MF	MF	1.79	0.16	0.01	2.09	0.32	-0.18
2	MF	PRF	1.76	0.24	0.00	1.79	0.39	0.07
3	MF	PU	1.65	0.14	0.01	2.32	0.35	-0.44
4	PRF	MF	1.75	0.20	-0.07	1.57	0.25	0.14
5	PRF	PRF	1.75	0.23	-0.02	1.45	0.23	0.30
6	PRF	PU	1.69	0.15	-0.03	1.50	0.21	0.17
7	PU	MF	1.57	0.12	0.03	2.35	0.50	-0.54
8	PU	PRF	1.63	0.23	0.04	2.23	0.44	-0.30
9	PU	PU	1.62	0.14	0.03	2.47	0.30	-0.57
Laminate average			1.69			1.97		

Table 4.26. Bartlett's test for homogeneity of variance for face-gluing effect.

1st Lamina Charring Rate			
Source	DF	Chi-Square	Pr > ChiSq
Adhesive	2	1.4844	0.4761
2nd Lamina Charring Rate			
Source	DF	Chi-Square	Pr > ChiSq
Adhesive	2	3.1810	0.2038

Table 4.27. ANOVA results for charring rate for face-gluing effect.

1st Lamina Charring Rate					
Source	DF	Sum of Squares	Mean Square	F Value	Pr > F
Adhesive	2	0.03126667	0.01563334	6.12	0.0356
Error	6	0.01533333	0.00255556		
Corrected Total	8	0.04660000			
2nd Lamina Charring Rate					
Source	DF	Sum of Squares	Mean Square	F Value	Pr > F
Adhesive	2	1.10508889	0.55254445	18.70	0.0026
Error	6	0.17733333	0.02955556		
Corrected Total	8	1.28242222			

Table 4.28. Duncan grouping for charring rate for face-gluing effect.

1st Lamina Charring Rate			
Duncan Grouping	Mean	N	Adhesive
A	1.733	3	MF
A	1.730	3	PRF
B	1.607	3	PU
2nd Lamina Charring Rate			
Duncan Grouping	Mean	N	Adhesive
A	2.350	3	PU
A	2.067	3	MF
B	1.507	3	PRF

The effect of face glue type on second layer charring rate was verified by visual observation of the samples. During the fire test, no char was observed on the floor inside the furnace when the PRF face-glued samples were tested. However, all of PU and MF face-glued samples

exhibited delamination during the test. The presence of unburnt area (white or light color area) on PU and MF face-glued samples, as shown in Figure , suggested that delamination occurred below the wood pyrolysis temperature. No unburnt areas were found on any of the PRF face-glued samples.

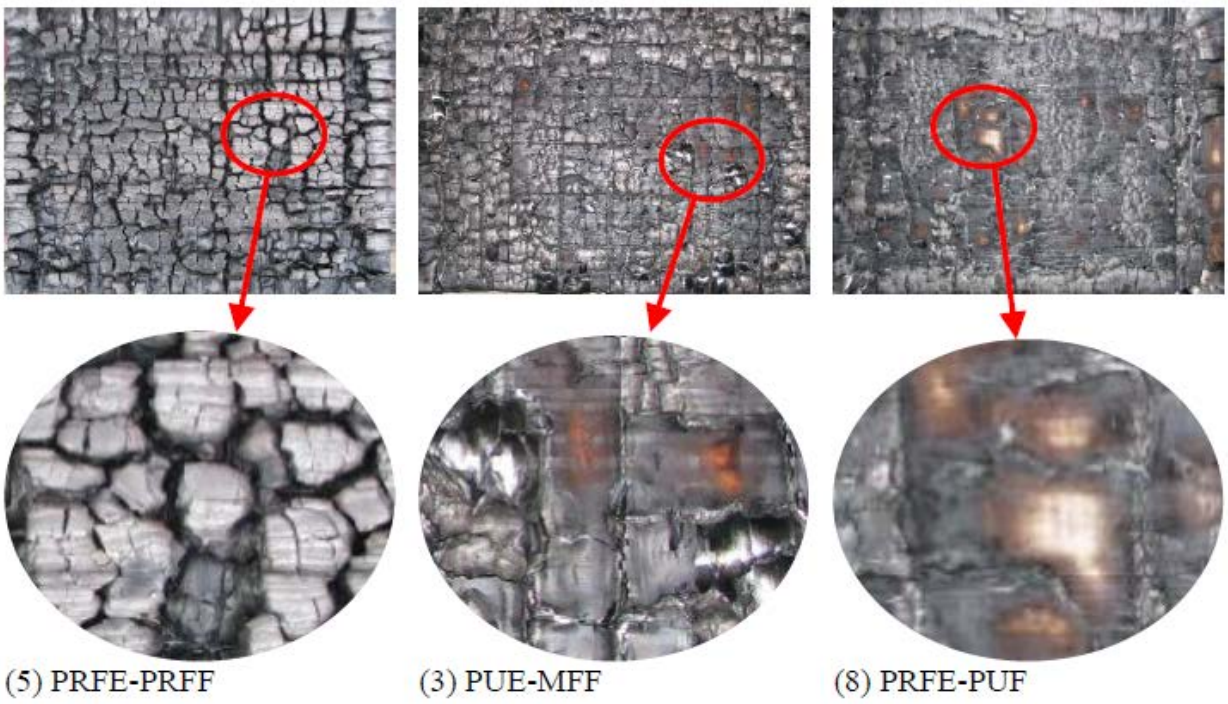

Figure 22. Comparison of the fire-exposed side of typical specimen from each face-glue group.

Although, edge-gluing did not seem to have a significant effect on the fire performance based on the data, as shown in Table 4.29 and 4.30, further analysis of the second lamina char rate data within each face gluing group revealed some influences of edge gluing. It can be found in Table 14 that within each face gluing group, the second lamina char rate of PRF edge-glued specimen was the lowest. For instance, in the MF face-glued group, the second lamina char rate of the PRF edge glued specimen was 1.79 in/hr, which is lower than those of the other two specimens. As shown previously, MF and PU degrade at around 250 °C. Therefore gaps along the edge gluelines in the first lamina of MF and PU edge-glued specimens would develop before the char layer fell off. These gaps opened paths for heat transfer into the second lamina. As a

result, the second lamina was exposed to fire and heated up much earlier. On the other hand no gaps developed along the edge gluelines in PRF edge-glued specimen, which behaved like solid wood, therefore the second laminate was protected. However, since the variance was large and there were no replications, we could not draw any strong statistical conclusions.

Table 4.29. Bartlett's test for homogeneity of variance for edge-gluing effect.

1st Lamina Charring Rate			
Source	DF	Chi-Square	Pr > ChiSq
Adhesive	2	2.0236	0.3636
2nd Lamina Charring Rate			
Source	DF	Chi-Square	Pr > ChiSq
Adhesive	2	0.1820	0.9130

Table 4.30. ANOVA analysis results for charring rate for edge-gluing effect.

1st Lamina Charring Rate					
Source	DF	Sum of Squares	Mean Square	F Value	Pr > F
Adhesive	2	0.00620000	0.00310000	0.46	0.6516
Error	6	0.04040000	0.00673333		
Corrected Total	8	0.04660000			
2nd Lamina Charring Rate					
Source	DF	Sum of Squares	Mean Square	F Value	Pr > F
Adhesive	2	0.11582222	0.05791111	0.30	0.7528
Error	6	1.16660000	0.19443333		
Corrected Total	8	1.28242222			

4.3.3. Non-linear char rate model

A nonlinear char rate model shown below was also adopted to analyze the fire test data.

$$t_{300°C} = \left(\frac{x}{\beta}\right)^{1.23} \quad (6)$$

Table 4.31 presents the summarized results for the non-linear model. The conclusions were similar except that the evidence of edge-gluing effect was even weaker. Statistical analysis results for face- and edge-gluing effects are summarized in subsequent tables.

Table 4.31. Summarized result of glue effect in non-linear model.

Specimen #	Adhesive		$t = (d_{char}/\beta)^{1.23}$	
	Face	Edge	1st Lamina	2nd Lamina
			β (in/hr)	β (in/hr)
1	MF	MF	1.65	1.97
2	MF	PRF	1.64	1.92
3	MF	PU	1.55	1.96
4	PRF	MF	1.54	1.77
5	PRF	PRF	1.52	1.77
6	PRF	PU	1.54	1.73
7	PU	MF	1.51	1.93
8	PU	PRF	1.58	1.99
9	PU	PU	1.55	1.97
Lamina average			1.56	1.89

Table 4.32. Bartlett's test for homogeneity of variance for face-gluing effect in non-linear charring rate model.

1st Lamina Charring Rate			
Source	DF	Chi-Square	Pr > ChiSq
Adhesive	2	3.0183	0.2211
2nd Lamina Charring Rate			
Source	DF	Chi-Square	Pr > ChiSq

Adhesive	2	0.1277	0.9382

Table 4.33. ANOVA analysis results for charring rate for face-gluing effect in non-linear charring rate model.

1st Lamina Charring Rate					
Source	DF	Sum of Squares	Mean Square	F Value	Pr > F
Adhesive	2	0.01102222	0.00551111	3.76	0.0875
Error	6	0.00880000	0.00146667		
Corrected Total	8	0.01982222			
2nd Lamina Charring Rate					
Source	DF	Sum of Squares	Mean Square	F Value	Pr > F
Adhesive	2	0.08026667	0.04013333	55.57	0.0001
Error	6	0.00433333	0.00072222		
Corrected Total	8	0.08460000			

Table 4.34. Duncan grouping for charring rate for face-gluing effect in non-linear charring rate model.

1st Lamina Charring Rate				
Duncan Grouping		Mean	N	Adhesive
	A	1.613	3	MF
B	A	1.547	3	PU
B		1.533	3	PRF
2nd Lamina Charring Rate				
Duncan Grouping		Mean	N	Adhesive
A		1.963	3	PU
A		1.950	3	MF
B		1.757	3	PRF

Table 4.35. Bartlett's test for homogeneity of variance for edge-gluing effect in non-linear charring rate model.

1st Lamina Charring Rate			
Source	DF	Chi-Square	Pr > ChiSq
Adhesive	2	6.1293	0.0467
2nd Lamina Charring Rate			
Source	DF	Chi-Square	Pr > ChiSq
Adhesive	2	0.1141	0.9445

Table 4.36. ANOVA analysis results for charring rate for edge-gluing effect in non-linear charring rate model.

1st Lamina Charring Rate					
Source	DF	Sum of Squares	Mean Square	F Value	Pr > F
Adhesive	2	0.00168889	0.00084444	0.28	0.7656
Error	6	0.01813333	0.00302222		
Corrected Total	8	0.01982222			
2nd Lamina Charring Rate					
Source	DF	Sum of Squares	Mean Square	F Value	Pr > F
Adhesive	2	0.00006667	0.00003333	0.00	0.9976
Error	6	0.08453333	0.01408889		
Corrected Total	8	0.08460000			

4.3.4. Comparison with previous tests involving samples with no edge glue

The purpose of the intermediate-scale horizontal fire test was to determine the edge-gluing effect on fire performance. It was hypothesized that edge-gluing could reduce the possibility of forming open paths hence enhance the fire performance of CLT. However, the opposite is also possible: edge-gluing adhesives can constrain the wood while it shrinks thus leading to cracks that provide path for the flame. To evaluate the edge-gluing effect, previous

non-edge-glued test results obtained by our research group were used as a control to compare with results in this study (Hasburgh et al., 2016). To differentiate, non-edge-glued samples will be referred to as Group A while edge-glued samples belong to Group B.

Figure 4.23. Comparison of exposed surfaces prior fire test of sample 3 from Group A (left, non-edge-glued) and sample (5) from Group B (edge-glued). (Courtesy of Forest Product Laboratory).

Although both groups of samples were made of southern yellow pine, they were not from the same batch. Group A samples had more/larger pith, knots and other defects than those of Group B as shown in Figure 4.23. This may affect the charring rate.

Group A samples were manufactured at Clemson University with 1.375 inches thick laminae, with the three-ply CLT samples having final dimensions of 4.125in × 47 in ×38 in (thickness×length×width). Group B samples were made of 1.25 inches thick laminae at North Carolina State University with the final dimensions of 3.75in × 40 in ×30 in

(thickness×length×width). According to both the Canadian and US CLT Handbooks, thickness of individual lamina could affect the charring rate. The Canadian CLT Handbook suggested that for thickness less than 35mm, a conservative linear charring rate estimate can be determined by:

$$\beta = 0.65^{\frac{d}{35}} \tag{8}$$

where d is the lamina thickness in mm and β is the linear charring rate in mm/min. According to this equation, there would be an approximately 4% increase in linear charring rate for Group B sample when compared to Group A. This predicted 4% difference was used to normalize and compare results from two groups, as presented in

Table 4.37.

In Group A, both PRF and MF face-glued samples showed no or only little delamination; while in Group B, although PRF face-glued samples still had no delamination, those of MF exhibited significant delamination during the test. This could be due to different pre-condition setups of wood or manufacturing processes. PU face-glued samples presented similar delamination behaviors in both tests.

Table 4.37. Comparison of charring rate (inches per hour) between Clemson data (Group A, only 3-layer CLT included) and NCSU data (Group B).

	Linear Charring rate model		Non-Linear Charring rate model	
	Group A	Group B	Group A	Group B
1st Lamina MF	1.54	1.73 (0.07)	1.41	1.61 (0.06)
1st Lamina PRF	1.85	1.73 (0.03)	1.72	1.56 (0.03)
1st Lamina PU	1.81	1.61 (0.03)	1.60	1.55 (0.04)
2nd Lamina MF	1.73	2.07 (0.27)	1.77	1.95 (0.03)
2nd Lamina PRF	1.64	1.51 (0.06)	1.94	1.76 (0.03)
2nd Lamina PU	1.99	2.35 (0.12)	1.97	1.96 (0.04)

Notes: Numbers in the brackets are standard deviations.

Linear and non-linear charring rate data comparisons of Group A and B are also presented in Figure -Figure . No clear trends were found for first lamina linear charring rate. This was expected as the first lamina in both groups behaved similarly to solid timber. For the second lamina, PRF face glued samples showed similar performance in both groups. This was because PRF was the most thermally stable adhesive and the only one that didn't show any delamination in either group. The difference of linear charring rates of MF faced glued samples may be partially due to the different thermal properties between two groups. Delamination of MF face glued samples were observed in Group B while Group A counterparts exhibited no or little delamination. The second-lamina linear charring rates of PU face-glued sample in Group B were larger than those in Group A. However, since there were no replications, the cause was hard to find.

The trends in the non-linear model as shown in Figure 4.25 were similar to but not as pronounced as in the linear model.

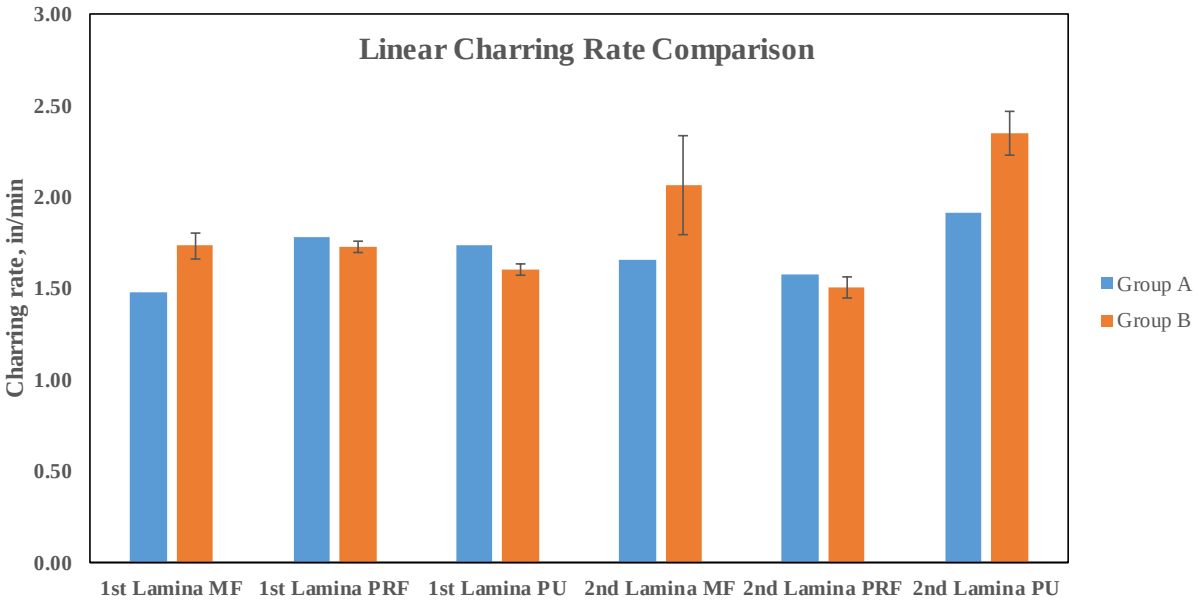

Figure 4.24. Comparison of linear charring rate data from Group A and Group B.

Figure 4.25. Comparison of non-linear charring rate data from Group A and Group B.

5. Conclusions

With the aim to study the effect of edge-gluing on the fire performance of cross-laminated timber (CLT) panels, small-scale fire tests, thermogravimetric and differential scanning analyses, and intermediate-scale horizontal fire tests were carried out. From the results of the study, it could be concluded that:

- Polurethane (PU) adhesive is less thermally stable than phenol-resorcinol formaldehyde (PRF) and melamine formaldehyde (MF) adhesives. PRF is a better adhesive than MF under high temperature and fire conditions.
- The type of face-gluing adhesive has a significant effect on the charring rate of the second layer of a CLT. Panels face-glued with PRF has the lowest second layer charring rate.
- This study could not conclusively show that edge gluing can significantly affect the charring rate. Further studies with more replications are recommended to confirm this conclusion.

CHAPTER 5. SUMMARY

Cross-laminated timber (CLT) has several advantages and has the great potential to substitute for concrete and steel in building envelopes. However, being a hygroscopic and combustible material, the lack of database (such as southern pine CLT) raises concerns of water accumulation and mold growth, dimensional stability and fire safety of building envelops.

To address the concerns, three commonly available adhesives, polyurethane (PU), phenol resorcinol formaldehyde (PRF) and melamine formaldehyde (MF) were applied to prepare southern pine CLTs. The diffusion process of southern pine CLT was studied first by means of diffusion cup method, then modeled and simulated by COMSOL MULTIPHYSICS in Chapter 2. Results showed that glueline moisture diffusion coefficient was independent of adhesive type. The hygrothermal performance of CLT building envelopes were analyzed thereafter and found that a properly designed CLT wall assembly did not provide favorable conditions for mold growth.

Then in Chapter 3, warping studies were conducted with the aim of analyzing the dimensional stability of southern pine CLTs. The warping measurement was perform on ARAMIS Adjustable system. Hygrothermal warping model was applied. Warping results validated the hygrothermal warping model and revealed that cross lamination method did improve the dimensional stability as compared to solid wood and adhesive types had no or little effect on warping.

Lastly, first tests and thermal analyses were conducted to analyze the fire performance of southern pine CLT in Chapter 4. Findings from the fire tests and thermal analyses showed that PU performed poorly under high temperature or fire conditions while PRF was very thermally

stable. It also found that adhesive type had a significant effect on the charring rate of the second layer of CLT. The effect of edge gluing however remained uncertain, and further research with more replications is needed.

References

Standard for Performance-Rated Cross-Laminated Timber, StandardU.S.C. (2012).

Amini, M. O., van de Lindt, J. W., Pei, S., Rammer, D., Line, P., & Popovski, M. (2014). Overview of a project to quantify seismic performance factors for cross laminated timber structures in the united states. *Materials and Joints in Timber Structures: Recent Developments of Technology, 9*, 531-541. doi:10.1007/978-94-007-7811-5_49

ASTM, E. (2011). 119. *Standard Test Methods for Fire Tests of Building Construction and Materials, ASTM International, West Conshohocken, PA,*

Baettig, R., Rémond, R., & Perré, P. (2006). Measuring moisture content profiles in a board during drying: A polychromatic X-ray system interfaced with a vacuum/pressure laboratory kiln. *Wood Science and Technology, 40*(4), 261-274.

Bogensperger, T., Fitz, M., Hamm, P., & Schickhofer, G. (2010). Investigation of vibration behaviour of floors made of cross laminated timber (CLT). *Bauingenieur, 85,* 45-52.

Branco, J. M., Kekeliak, M., & Lourenco, P. B. (2014). In-plane stiffness of traditional timber floors strengthened with CLT. *Materials and Joints in Timber Structures: Recent Developments of Technology, 9*, 725-737. doi:10.1007/978-94-007-7811-5_65

Brandner, R., Bogensperger, T., & Schickhofer, G. (2013). In plane shear strength of cross laminated timber (CLT): Test configuration, quantification and influencing parameters. *Proceedings of the Cib - W18: Working Commission W18 - Timber Structures, ,* 229-241.

Brief, A. (1990). The role of adhesives in the economy. *Handbook of adhesives* (pp. 21-38) Springer.

Burgert, I., & Eckstein, D. (2001). The tensile strength of isolated wood rays of beech (fagus sylvatica L.) and its significance for the biomechanics of living trees. *Trees, 15*(3), 168-170.

Cachim, P. B., & Franssen, J. (2009). Assessment of eurocode 5 charring rate calculation methods. *Fire Technology, 46*(1), 169. doi:10.1007/s10694-009-0092-x

Cangemi, J. M., Claro Neto, S., Chierice, G. O., & Santos, A. M. d. (2006). Study of the biodegradation of a polymer derived from castor oil by scanning electron microscopy, thermogravimetry and infrared spectroscopy. *Polímeros, 16*(2), 129-135.

Ceccotti, A., Sandhaas, C., Okabe, M., Yasumura, M., Minowa, C., & Kawai, N. (2013). SOFIE project-3D shaking table test on a seven-storey full-scale cross-laminated timber building. *Earthquake Engineering & Structural Dynamics, 42*(13), 2003-2021. doi:10.1002/eqe.2309

Chen, Y., & Lam, F. (2013). Bending performance of box-based cross-laminated timber systems. *Journal of Structural Engineering, 139*(12) doi:10.1061/(ASCE)ST.1943-541X.0000786

Chow, S. (1977). A curing study of phenol-resorcinol-formaldehyde resins using infrared spectrometer and thermal analysis. *Holzforschung-International Journal of the Biology, Chemistry, Physics and Technology of Wood, 31*(6), 200-205.

Coats, A., & Redfern, J. (1963). Thermogravimetric analysis. A review. *Analyst, 88*(1053), 906-924.

Costa, L., & Camino, G. (1988). Thermal behaviour of melamine. *Journal of Thermal Analysis, 34*(2), 423-429.

Daniel-da-Silva, A. L., Bordado, J. C. M., & Martín-Martínez, J. M. (2008). Moisture curing kinetics of isocyanate ended urethane quasi-prepolymers monitored by IR spectroscopy and DSC. *Journal of Applied Polymer Science, 107*(2), 700-709.

Daniel, I. M., Ishai, O., Daniel, I. M., & Daniel, I. (1994). *Engineering mechanics of composite materials* Oxford university press New York.

DANTEC DYNAMICS. Measurement Principles of (DIC): https://www.dantecdynamics.com/measurement-principles-of-dic

Devallencourt, C., Saiter, J., Fafet, A., & Ubrich, E. (1995). Thermogravimetry/fourier transform infrared coupling investigations to study the thermal stability of melamine formaldehyde resin. *Thermochimica Acta, 259*(1), 143-151.

EN, B. (1995). 1-2 eurocode 5. design of timber structures. general structural fire design. *British Standards Institution,*

CLT Handbook US Edition, ANI StandardU.S.C. (2013).

F. A. Long, David Richman. (1960). Concentration gradients for diffusion of vapors in glassy polymers and their relation to time dependent diffusion phenomena. *Journal of the American Chemical Society, 3,* 513-519.

Fragiacomo, M., Menis, A., Clemente, I., Bochicchio, G., & Ceccotti, A. (2013). Fire resistance of cross-laminated timber panels loaded out of plane. *Journal of Structural Engineering, 139*(12) doi:10.1061/(ASCE)ST.1943-541X.0000787

Frangi A., Fontana M., Knobloch M., Bochicchio G.,9th International Symposium on Fire Safety Science,. (2008). Fire behaviour of cross-laminated solid timber panels. *Fire Saf.Sci.Fire Safety Science, ,* 1279-1290. Retrieved from /z-wcorg/ database.

Frangi, A., Fontana, M., Hugi, E., & Jübstl, R. (2009a). Experimental analysis of cross-laminated timber panels in fire. *Fire Safety Journal, 44*(8), 1078-1087.

Frangi, A., Fontana, M., Hugi, E., & Jübstl, R. (2009b). Experimental analysis of cross-laminated timber panels in fire. *Fire Safety Journal, 44*(8), 1078-1087. doi:http://dx.doi.org.prox.lib.ncsu.edu/10.1016/j.firesaf.2009.07.007

Frihart, C. R. (2004). Adhesive interactions with wood.

Frihart, C. R. (2005). 9 wood adhesion and adhesives. *Handbook of Wood Chemistry and Wood Composites, ,* 215.

Frihart, C. R. (2015). Introduction to special issue: Wood adhesives: Past, present, and future. *Forest Products Journal, 65*(1), 4-8.

Friquin, K. L. (2011). Material properties and external factors influencing the charring rate of solid wood and glue-laminated timber. *Fire and Materials, 35*(5), 303-327.

Friquin, K. L., Grimsbu, M., & Hovde, P. J. (2010). Charring rates for cross-laminated timber panels exposed to standard and parametric fires. Paper presented at the *Proceedings of the 11th World Conference on Timber Engineering*,

Gereke, T. (2009). Moisture-induced stresses in cross-laminated wood panels. (Doctoral thesis, Dipl.-Ing., University of Leipzig).

Gereke, T., Gustafsson, P. J., Persson, K., & Niemz, P. (2009). Experimental and numerical determination of the hygroscopic warping of cross-laminated solid wood panels. *Holzforschung, 63*(3), 340-347.

Gereke, T., & Niemz, P. (2010a). A numerical study on the influence of the bond-line diffusivity on moisture-related stresses and deformations of three-layered spruce cross-laminates. *Wood Material Science and Engineering, 5*(2), 62-66.

Gereke, T., Hass, P., & Niemz, P. (2010). Moisture-induced stresses and distortions in spruce cross-laminates and composite laminates. *Holzforschung*, *64*(1), 127-133. Retrieved from http://proxying.lib.ncsu.edu/index.php?url=http://search.ebscohost.com/login.aspx?direct=true&db=lah&AN=20103028529&site=ehost-live&scope=site; http://dx.doi.org/10.1515/HF

Gereke, T., Gustafsson, P. J., Persson, K., & Niemz, P. (2011). The hygroscopic warping of cross-laminated timber. In V. Bucur (Ed.), *Delamination in wood, wood products and wood-based composites* (pp. 269-285). Dordrecht: Springer Netherlands. doi:10.1007/978-90-481-9550-3_14

Gereke, T., & Niemz, P. (2010b). Moisture-induced stresses in spruce cross-laminates. *Engineering Structures, 32*(2), 600-606. doi:10.1016/j.engstruct.2009.11.006

Giana Almeida, Stéphane Gagné, & Roger Hernández. (2007). A NMR study of water distribution in hardwoods at several equilibrium moisture contents. *Wood Science & Technology, 41*(4), 293-307. Retrieved from http://search.ebscohost.com/login.aspx?direct=true&db=a9h&AN=25367813&site=ehost-live&scope=site

Hailwood, A., & Horrobin, S. (1946a). Absorption of water by polymers: Analysis in terms of a simple model. *Transactions of the Faraday Society, 42*, B084-B092.

Hailwood, A., & Horrobin, S. (1946b). Absorption of water by polymers: Analysis in terms of a simple model. *Transactions of the Faraday Society, 42*, B084-B092.

Hanhijärvi, A. (1995). Modelling of creep deformation mechanisms in wood, helsinki university of technology. technical research centre of finland. *VTT Publications.Espoo (SF), Dissertation,*

Hasburgh, L., Bourne, K., Peralta, P., Mitchell, P., Schiff, S., & Pang, W. (2016). Effect of adhesives and ply configuration on the fire performance of southern pine cross-laminated timber. Paper presented at the *World Conference on Timber Engineering. Vienna, Austria,*

Hass, P., Wittel, F. K., Mendoza, M., Herrmann, H. J., & Niemz, P. (2012). Adhesive penetration in beech wood: Experiments. *Wood Science and Technology, 46*(1-3), 243-256.

Hochreiner, G., Füssl, J., & Eberhardsteiner, J. (2014). Cross-laminated timber plates subjected to concentrated loading. *Strain, 50*(1), 68-81.

Ido, H., Nagao, H., Miura, S., & Miyatake, A. (2014). Compressive strength properties perpendicular to the grain of cross-laminated timber (CLT) composed of sugi laminations. *Mokuzai Gakkaishi, 60*(1), 16-22.

International Organization for Standardization. (2000). *Fire-resistance tests: Elements of building construction. specific requirements for loadbearing vertical separating elements* ISO.

Joebstl, R. A. (2010). In Cruz P. (Ed.), *Verification processes for cross laminated timber in the frame of EN 1995*

KÃ¶nig, J. (2005). Structural fire design according to eurocode 5â€”design rules and their background. *Fire and Materials, 29*(3), 147-163. doi:10.1002/fam.873

Karacebeyli, E., & Douglas, B. (2013). CLT handbook-US edition. *Library and Archives Canada Cataloguing in Publication, Quebec, Canada,*

Kettunen, P. O. (2006). *Wood structure and properties* Trans Tech Publications.

Kollmann, F., & Höckele, G. (1962). Comparison of procedure for the determination of moisture content in wood. *Holz Als Roh-Und Werkstoff, 20*(12), 461-473.

Kretschmann, D. E., & Green, D. W. (2007). Modeling moisture content-mechanical property relationships for clear southern pine. *Wood and Fiber Science, 28*(3), 320-337.

Labonnote, N., & Malo, K. A. (2010). In Cruz P. (Ed.), *Vibration properties of cross laminated timber floors*

Lawson, D., Webster, C., & Ashton, L. (1951). *Fire endurance of timber beams and floors* HM Stationery Office.

Lee, W., Chang, K., & Tseng, I. (2012). Properties of phenol-formaldehyde resins prepared from phenol-liquefied lignin. *Journal of Applied Polymer Science, 124*(6), 4782-4788.

Liu, J., Chen, R., Xu, Y., Wang, C., & Chu, F. (2017). Resorcinol in high solid phenol−formaldehyde resins for foams production. *Journal of Applied Polymer Science, 134*(22)

Marcinko, J. J., Devathala, S., Rinaldi, P. L., & Bao, S. (1998). Investigating the molecular and bulk dynamics of PMDI/wood and UF/wood composites. *Forest Products Journal, 48*(6), 81.

Marra, A. A. (1992). *Technology of wood bonding : Principles in practice*. New York: Van Nostrand Reinhold. Retrieved from http://www2.lib.ncsu.edu/catalog/record/NCSU792116

Menczel, J. D., Judovits, L., Prime, R. B., Bair, H. E., Reading, M., & Swier, S. (2009). Differential scanning calorimetry (DSC). *Thermal Analysis of Polymers: Fundamentals and Applications*, , 7-239.

Menis, A., Fragiacomo, M., & Clemente, I. (2012). Numerical investigation of the fire resistance of protected cross-laminated timber floor panels. *Structural Engineering International, 22*(4), 523-532. doi:10.2749/101686612X13363929517659

Merline, D. J., Vukusic, S., & Abdala, A. A. (2013). Melamine formaldehyde: Curing studies and reaction mechanism. *Polymer Journal, 45*(4), 413-419.

Neimsuwan, T., Wang, S., Taylor, A. M., & Rials, T. G. (2008). Statics and kinetics of water vapor sorption of small loblolly pine samples. *Wood Science and Technology, 42*(6), 493.

Niemz, P., & Sonderegger, W. (2013). Cross laminated timber - properties and use for building purposes: A review from the experience of swiss researchers. *Pro Ligno, 9*(1), 3-21. Retrieved from http://search.ebscohost.com/login.aspx?direct=true&db=lah&AN=20133188150&site=ehost-live&scope=site; http://www.cabi.org/cabdirect/showpdf.aspx?PAN=20133188150; http://www.proligno.ro/en/articles/2013/1/niemz_full.pdf

Okabe, M., Yasumura, M., Kobayashi, K., & Fujita, K. (2014). Prediction of bending stiffness and moment carrying capacity of sugi cross-laminated timber. *Journal of Wood Science, 60*(1), 49-58. doi:10.1007/s10086-013-1377-8

Ormarsson, S., Dahlblom, O., & Petersson, H. (1998). A numerical study of the shape stability of sawn timber subjected to moisture variation. *Wood Science and Technology, 32*(5), 325-334. Retrieved from http://proxying.lib.ncsu.edu/index.php?url=http://search.ebscohost.com/login.aspx?direct=true&db=lah&AN=19980617034&site=ehost-live&scope=site

Park, G. S., & Crank, J. (1968). Diffusion in polymers.

Petrie, E. M. (2007). *Handbook of adhesives and sealants*. New York: McGraw-Hill. Retrieved from http://www2.lib.ncsu.edu/catalog/record/UNCb5333415; Table of contents only (http://www.loc.gov/catdir/enhancements/fy0664/2006024251-t.html)

Pielichowski, K., & Njuguna, J. (2005). Thermal degradation of polymeric materials. (pp. 3-14) iSmithers Rapra Publishing.

Pizzi, A. (1994). *Advanced wood adhesives technology* CRC Press.

Pizzi, A., & Mittal, K. L. (2003). *Handbook of adhesive technology, revised and expanded* CRC press.

Popper, R., Niemz, P., & Eberle, G. (2004). Diffusion processes in multilayer solid wood panels. *Holz Als Roh-Und Werkstoff, 62*(4), 253-260.

Riggin, M. T., Sharp, A. R., Kaiser, R., & Schneider, M. H. (1979). Transverse NMR relaxation of water in wood. *Journal of Applied Polymer Science, 23*(11), 3147-3154. doi:10.1002/app.1979.070231101

Risbrudt, C. D., Ibach, R. E., Cruz-Barba, L., Williams, R. S., Winandy, J. E., Han, J. S., et al. (2005). *Handbook of wood chemistry and wood composites* CRC Press. doi:doi:10.1201/9780203492437

Sami Ullah, M. A. Bustam,M. Nadeem, M. Y. Naz, W. L. Tan, and A. M. Shariff. (2014). Synthesis and thermal degradation studies of melamine formaldehyde resins. *The Scientific World Journal, 2014*

Schaffer, E. L. (1968). *A simplified test for adhesive behavior in wood sections exposed to fire* Forest Products Laboratory.

Schmid, J., Menis, A., Fragiacomo, M., Clemente, I., & Bochicchio, G. (2015). Behaviour of loaded cross-laminated timber wall elements in fire conditions. *Fire Technology, 51*(6), 1341-1370.

Schmid, J., Konig, J., & Kohler, J. (2010). In Kodur V. F.,JM (Ed.), *Design model for fire exposed cross-laminated timber*

Seymour, R. W., & Cooper, S. L. (1971). DSC studies of polyurethane block polymers. *Journal of Polymer Science Part B: Polymer Letters, 9*(9), 689-694. doi:10.1002/pol.1971.110090911

Siau, J. F. (1984). *Transport processes in wood*. Berlin ; New York: Springer-Verlag. Retrieved from http://www2.lib.ncsu.edu/catalog/record/NCSU606900

Siau, J. F. (1995). In Virginia Polytechnic Institute and State University. Department of Wood Science & Forest Products (Ed.), *Wood : Influence of moisture on physical properties*. Blacksburg, VA]: Dept. of Wood Science and Forest Products, Virginia Polytechnic Institute and State University. Retrieved from http://www2.lib.ncsu.edu/catalog/record/NCSU908313

SKAAR, C. (1984). Wood water relationships. *Advances in Chemistry Series,* (207), 127-172.

Sonderegger, W., Hering, S., Mannes, D., Vontobel, P., Lehmann, E., & Niemz, P. (2010). Quantitative determination of bound water diffusion in multilayer boards by means of

neutron imaging. *European Journal of Wood and Wood Products, 68*(3), 341-350. Retrieved from http://search.ebscohost.com/login.aspx?direct=true&db=lah&AN=20103268170&site=ehost-live&scope=site; http://www.springerlink.com/content/u5l7tt0584p47407/

Stamm, A. J., & Nelson, R. (1961). Comparison between measured and theoretical drying diffusion coefficients for southern pine. *Forest Prod.J, 11*(11), 536-543.

Stamm, A. J. (1935). SHRINKING and SWELLING of WOOD. *Industrial & Engineering Chemistry, 27*(4), 401-406. doi:10.1021/ie50304a011

Stürzenbecher, R., Hofstetter, K., & Eberhardsteiner, J. (2010). Cross laminated timber: A multi-layer, shear compliant plate and its mechanical behavior. Paper presented at the *Proceedings of the World Conference on Timber Engineering,*

Tabatabaian, M. (2015). *COMSOL5 for engineers* Stylus Publishing, LLC.

Toratti, T. (1994). Creep of timber beams in a variable environment.

Trick, K. A., & Saliba, T. E. (1995). Mechanisms of the pyrolysis of phenolic resin in a carbon/phenolic composite. *Carbon, 33*(11), 1509-1515.

Trovati, G., Sanches, E. A., Neto, S. C., Mascarenhas, Y. P., & Chierice, G. O. (2010). Characterization of polyurethane resins by FTIR, TGA, and XRD. *Journal of Applied Polymer Science, 115*(1), 263-268. doi:10.1002/app.31096

van Meel, P., Erich, S., Huinink, H. P., Kopinga, K., de Jong, J., & Adan, O. (2011). Moisture transport in coated wood. *Progress in Organic Coatings, 72*(4), 686-694. doi:http://dx.doi.org/10.1016/j.porgcoat.2011.07.011

Vick, C. B., & Christiansen, A. W. (2007). Cure of phenol-formaldehyde adhesive in the presence of CCA-treated wood by differential scanning calorimetry. *Wood and Fiber Science, 25*(1), 77-86.

Wadsö, L. (1992). *A test of different methods to evaluate the diffusivity from a sorption measurement* na.

Wadsö, L. (1993a). *Studies of Water Vapor Transport and Sorption in Wood,*

Wadsö, L. (1993b). Measurements of water vapour sorption in wood. *Wood Science and Technology, 28*(1), 59-65.

White, R. H., & Nordheim, E. V. (1992). Charring rate of wood for ASTM E 119 exposure. *Fire Technology, 28*(1), 5-30.

White, R. H. (2016). Analytical methods for determining fire resistance of timber members. In M. J. Hurley, et al. (Ed.), *SFPE handbook of fire protection engineering* (pp. 1979-2011). New York, NY: Springer New York. doi:10.1007/978-1-4939-2565-0_55

Wimmer, R., Kläusler, O., & Niemz, P. (2013). Water sorption mechanisms of commercial wood adhesive films. *Wood Science and Technology, 47*(4), 763-775. Retrieved from http://search.ebscohost.com/login.aspx?direct=true&db=lah&AN=20133229930&site=ehost-live&scope=site; http://rd.springer.com/article/10.1007/s00226-013-0538-7

Wood handbook electronic resource] : Wood as an engineering material. (2010).